Evaluation of a new trigger function for cumulus convection

M.J. de Haij

Utrecht University MSc thesis

Supervisors:

dr. A.P. Siebesma
Royal Dutch Meteorological Institute, De Bilt (KNMI)
dr. A.J. van Delden
Institute for Marine and Atmospheric research Utrecht (IMAU)

De Bilt, The Netherlands, January 2005

Abstract

Cumulus convection plays a major role in the vertical transport of heat, moisture, momentum and chemical tracers in the atmosphere. Because of the small horizontal size, cumulus clouds can not be explicitly resolved in climate and numerical weather prediction models. Hence, a parameterization is needed.

The convection scheme of the ECMWF model was equipped with a new trigger function, proposed by Siebesma and Jakob (2003). This new formulation originates from the idea that the equations that describe the updraft properties in the cloud layer can be extended to the subcloud layer. This gives opportunities to aim for a unified formulation for the cumulus-topped boundary layer as a whole. The updraft equations consist of assumptions about lateral mixing of thermodynamical properties and the vertical velocity. Furthermore, the roots of the clouds (thermals) are assumed to have a certain excess in heat and moisture with respect to their environment, at their prescribed release height.

First, this formulation is tested in an offline model and sensitivity tests for various parameters are performed. The model input is obtained from data gathered at the BBC2 cloud campaign at Cabauw (May 2003) and consists mainly of mast, radiosonde, aircraft and remote sensing measurements. The evaluation of model outcome is as well carried out with data from certain shallow cumulus days in this period. For the studied cases, we find that the offline model simulates the observed cloud convective properties considerably well, as well as the presence of clouds during the day. Cloud tops are overestimated in multiple layer situations of boundary layer clouds. For the sensitivity, we notice that the new formulation is less sensitive for changes in parcel release parameters than the formulation that can be associated with the old trigger function. This is mainly caused by the assumption of lateral exchange of the updraft with its environment in the subcloud layer.

In the second part of the study, coherent structures along the Cabauw mast are identified with help of high-frequent sonic anemometer measurements. Wavelet analysis is used to determine prevailing time scales, whereafter the characteristics of thermals during typical convective conditions are studied. For the 5 m level in Cabauw, we find dominant time scales that agree well with values found in Krusche and de Oliveira (2004), i.e. 19 – 39 s. This derived dominant time scale grows with height, as well as the uncertainty in it. The feedback of this part of the project on the offline model lies in the excess factors for temperature and humidity that can be obtained from mean thermal properties. We find excess factors $b_T = 2.68 \pm 0.08$ and $b_q = 3.32 \pm 0.10$ for sampling on simultaneous positive temperature and humidity anomalies, while sampling on positive anomalies in vertical velocity delivers $b_T = 1.51 \pm 0.23$ and $b_q = 1.59 \pm 0.21$.

Contents

1 General Introduction

1.1 Introduction

Shallow cumulus convection has long been recognized as an important redistribution mechanism of heat, moisture and momentum in the cloudy atmospheric boundary layer (ABL). The representation of this non-precipitative form of convection in large-scale models is a main topic in boundary layer research and has been approached in numerous ways. In this paper, we try to gain a better insight in a significant part of the description of shallow cumulus clouds in weather and climate prediction models, the so-called trigger function.

Convection is inextricably bound up with turbulent – i.e. random – motions caused by eddies with different length scales. Because of inhomogeneity of the earth's surface, solar radiation tends to form rising thermal structures there, which organize in large eddies and cause updraft motions that rise throughout the ABL. If these updrafts get saturated due to cooling, liquid water is formed and the latent heat that is released by the condensation process, causes the generation of buoyancy for a further rise. A cumulus cloud is born.

1.2 On cumulus clouds and their importance

1.2.1 Introduction

In 1801, the Frenchman Jean Lamarck made a first classification of clouds. Subsequently, in 1803, the English scientist Luke Howard made a separation between three cloud forms: *cumuliform*, *stratiform* and *cirriform*, that was more or less adopted by the International Meteorological Commission in 1929. Nowadays, some modifications have been introduced. After World War II, the World Meteorological Organization published the International Cloud Atlas, which contains 10 families subdivided in 14 cloud species. A distinction can be made between the cloud divisions:

- Low-level clouds (cloud base 0 – 2 km)
- Mid-level clouds (cloud base 2 – 6 km)
- High-level clouds (cloud base > 6 km)
- Vertically developed clouds (convective clouds with cloud base 500 m – 6 km)

In appendix B, an overview of the most common cloud types for each form is presented by several photographs.

1.2.2 Cumuliform cloud types

Because of the main concern on boundary layer convective cloud formation, we will hereafter focus on cumuliform cloud types. These are in general characterized by grey, flat cloud bases and bright cloud tops. Furthermore, they all show in some kind cauliflower-shaped structures, which are caused by the turbulent motions due to instability inside the cloud layer. Considering cumuliform clouds, we discriminate between three types:

- **Deep cumulus (Cu)**

This type of cumulus cloud is deep enough to become precipitative. Deep cumulus (Cu) generally has its cloud base between 500 m and 6 km while its cloud top can reach a height up to 10 km, if one considers deep convective monsoon towers. Inside the cloud strong turbulence is present, characterized by vertical velocities that can have values up to $10 ms^{-1}$. Cloud droplets are mostly in ice form. Deep cumulus clouds in an unstable atmosphere are very often followed by a growth to cumulonimbus cloud with an anvil on top, which is a thunderstorm cloud that can be accompanied by heavy hail fall and lightning.

- **Stratocumulus (Sc)**

This cumuliform type is characterized by its layered pattern and occurs usually at heights of 500 m - 1 km. Stratocumulus (Sc) clouds cause the atmosphere to look quite grey. Except for some small openings, the horizontally extended stratocumulus cloud decks cover the sky completely. Precipitation may fall out of this cloud type, in general in the form of drizzle. In our area, Sc fields occur very often above the North Sea.

- **Shallow cumulus (ShCu)**

The nice looking, puffy clouds called shallow cumulus (ShCu) or *cumulus humilis* are the main subject of this paper. Because of their occurrence in combination with cloudless blue sky, they are also called fair-weather cumulus. Typically, their cloud base is flat and located between 500 and 2000 metres and they are hundreds of metres thick. The height of the cloud base strongly depends on the location, i.e. above land it will be higher than above sea. The horizontal size of shallow cumulus can reach up to 1 km, while cloud cover is typically 20 – 40%. They are not deep enough to form precipitation. In chapter 2, a developing shallow cumulus cloud will be diagnosed from its origin at the surface to its cloud top, which is reached in the inversion layer.

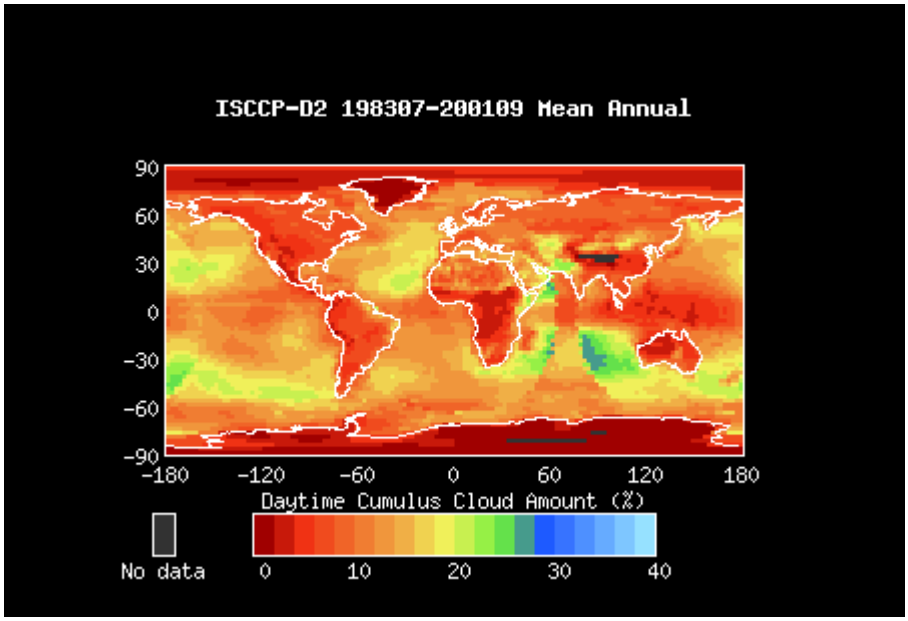

FIGURE 1.1 Mean annual daytime cumulus cloud amount (July 1983 - September 2001), according to the database of the International Satellite Cloud Climatology Project (ISCCP). Note the dominating occurrence of cumulus in the trade-wind areas (around 30° N and 30° S).

1.2.3 Climatic impact of shallow cumulus clouds

In general, clouds are one of the most important contributors to uncertainties in revealing the climate system. They act as transport mechanism for heat, moisture, momentum and chemical tracers on scales differing from boundary layer height to thousands of kilometers, depending on their height and environmental conditions. Furthermore, clouds have a major influence on the radiation budget in the earth's atmosphere, which entails all kinds of possible feedbacks on their physics and dynamics.

Shallow cumulus convection is a major venting mechanism for boundary layers all over the world, but especially in the subtropical belts or so-called trade-wind areas. In these areas, which are located around $30^{\circ}N$ and $30^{\circ}S$, shallow cumulus has the upper hand in occurrence on other cloud types (see Figure 1.1). The importance of ShCu in the trade-wind areas can be illustrated by considering a figure of the Hadley circulation, which is presented in Figure 1.2. In this circulation, shallow cumulus enhances the amount of moisture and heat that is transported to the intertropical convergence zone (ITCZ), where deep convective towers provide a substantial amount of precipitation during the wet monsoon. Furthermore, shallow cumulus counteracts warming and drying of the lower atmosphere, that is entailed by the subsidence, which is also caused by the Hadley circulation (Siebesma, 1998).

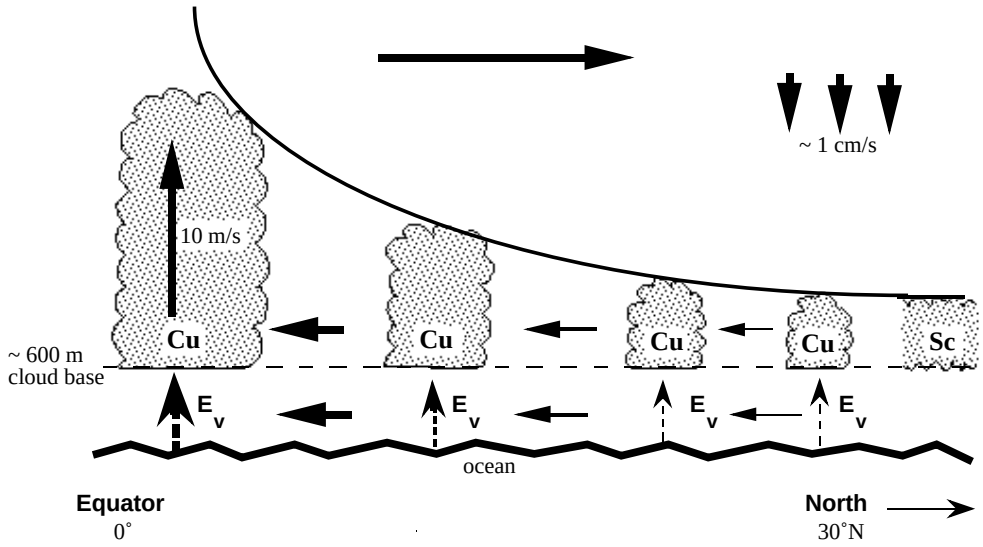

FIGURE 1.2 Schematic cross-section of the Hadley circulation on the Northern Hemisphere, illustrating the importance of trade-wind cumuli in it. Due to enhanced vertical transport of heat and moisture, which on their turn are transported to the ITCZ by the trade-winds, shallow cumulus clouds act as a major driving mechanism of the Hadley circulation (after Tiedtke, 1987). The black solid curve depicts the height of the capping inversion.

Concerning radiation, the influence of clouds is dependent on their vertical extent and the height of occurrence, but mainly on cloud cover. In general, incoming (solar) shortwave radiation is reflected by cumulus clouds, thereby they reduce warming of the surface. Because of the low cloud cover of shallow cumulus, its effect is considerably small. If we consider deep cumulus, this effect can reach a decrease in shortwave radiation up to $75 Wm^{-2}$. Because the transport caused by shallow cumulus enhances the amount of heat, moisture and momentum available for the development of deep cumuli, the indirect effect on this cooling is fairly present.

In contrary, it is especially high clouds – such as cirrus – that have a major effect on decreasing the outgoing longwave radiation of the earth, an effect that warms the earth's atmosphere. Cumuli also reflect longwave radiation both from higher and lower altitudes, though less effectively. Hence, their net effect is that they cool the earth's surface and the sub-cloud layer.

1.3 On cumulus parameterization

Current General Circulation Models (GCMs) – which can be categorized in of global climate models and Numerical Weather Prediction (NWP) models – are operational on a horizontal grid size of at least 100 and 10 kilometres, respectively. Because cumulus clouds – and especially shallow ones – occur on horizontal scales of typically 1 km, they can not be explicitly resolved. This is schematically presented in Figure 1.3. In the case of such a process, the large-scale model needs a so-called *parameterization*. A parameterization is an approximation or system of approximations for a sub-grid process, in terms of the large-scale variables. In the case of cumulus clouds, this means that the impact of an ensemble of cumulus clouds within a grid box is parameterized in terms of variables that are explicitly solved on the model grid. Generally, the contribution of sub-grid phenomena to grid box mean values is significant.

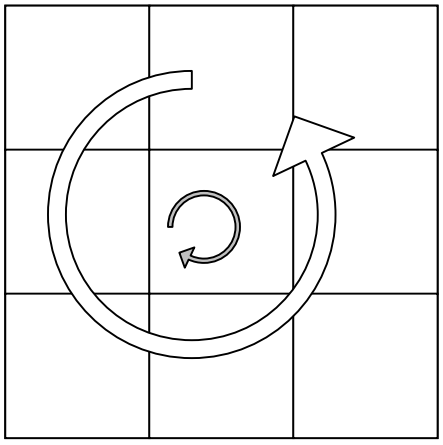

FIGURE 1.3 Illustration of the need for parameterization of variables. Unresolved sub-grid scale process (grey) versus resolved grid scale process (white).

Cumulus convection has been approached in numerous schemes, where the eddy diffusivity scheme (e.g. Bougeault, 1981) and the moist adjustment scheme (e.g. Betts, 1986) are two very important ones. A third, frequently used scheme in cumulus convection representation is a scheme that uses the (bulk) mass-flux approach (e.g. Tiedtke, 1989), which is described in more detail in section 4.2. This scheme is currently a widely accepted method.

Most General Circulation Models use a so-called K-diffusion scheme in the dry convective boundary layer, after which a mass-flux based convection scheme is employed in the case of moist convection. This is schematically depicted in Figure 1.4. Almost every convection scheme starts with the integration of a plume model at cloud base. Only recently, the importance of the sub-cloud layer in the parameterization of moist convection has been recognized. Its effects on weather and climate models outcome seem to be significant (e.g. Jakob and Siebesma, 2003).

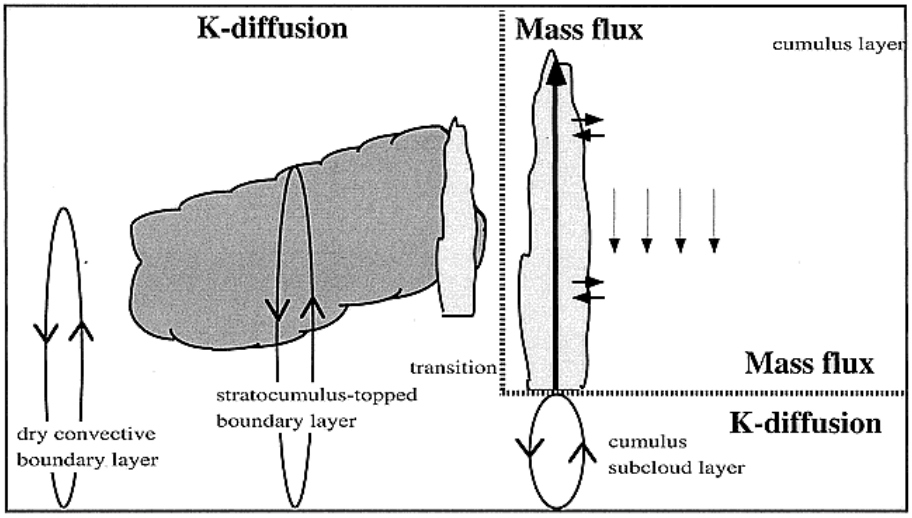

FIGURE 1.4 Coupling of boundary layer and cloud layer parameterizations. For cumulus, K-diffusion and mass-flux are connected to each other at cloud base by means of a so-called trigger function (after De Roode et al., 2000).

The so-called trigger function takes care of the switch between the boundary layer scheme and the convection scheme. It is a decision tree that decides whether convection takes place or not and determines the cloud convective properties at cloud base, as well as the type of convection (i.e. shallow or deep). With the proposal of a unified approach for the sub-cloud and in-cloud layer in case of cumulus convection (Jakob and Siebesma, 2003), one might be able to describe the cumulus layer on top of the boundary layer as a whole instead of as in two separate parts. The latter is schematically presented in the right part of Figure 1.4.

1.4 Research objectives

This paper is mainly concerned with the parameterization of cloud convective properties in shallow cumulus cases, in terms of sub-cloud profiles and surface fluxes. The main topic in achieving satisfactory results on this problem is a validation of the new ECMWF trigger function (Jakob and Siebesma, 2003).

In short, the three stages that were planned for succeeding this study are:

1) **Implement the new formulation (Jakob and Siebesma, 2003) in an offline parcel model.**
   - The model has to make an estimate of cloud convective properties on basis of observations in the sub-cloud layer.
2) **Perform a sensitivity study for updraft properties.**
   - What is the influence of different lateral mixing assumptions on sub-cloud and in-cloud updraft properties?
   - Are diluted ascents – contrary to undiluted ascents – not sensitive for release height and excess values of the rising parcel? And what role does the entrainment formulation play in this sensitivity?
3) **Characterize coherent 'thermal' structures in the surface layer.**
   - Derivation of thermal structure length scale as function of height.
   - Making an estimate of the excess proportionality factor that is part of the new formulation.
   - Derivation of mean thermal anomalies as a function of height.
   - Making an estimate of the contribution of thermals to total turbulent fluxes.

The measurements that are used for validation are particularly selected from the 2nd Baltex Bridge Campaign (BBC2), which was organized from May 3rd till May 24th 2003, near the Cabauw Experimental Site for Atmospheric Research (CESAR) in The Netherlands.

1.5 Outline

In chapter 2 the reader will be made more familiar with some theoretical concepts on which the research is based, differing from a description of the diurnal cycle of the atmospheric boundary layer to the theory of wavelet transforms.

In chapter 3 all of the used observations are presented, as well as the instruments that made these observations possible. The main features of the 2nd Baltex Bridge Campaign will be depicted. Furthermore, the main aspects of the Integrated Profiling Technique (IPT), which was used as the main model input deliverer, are presented.

The most important new aspects of the proposed trigger function and its implementation in the used offline 1D Single Parcel Ascent Model (1D SPAM) is presented in chapter 4. Subsequently, this chapter provides information about a profound method for identifying thermal structures using various criteria.

Subsequently, in chapter 5 the results of the experimental setup from chapter 4 are shown, in figures and text. Comparison will be made between the 1D SPAM outcome and aircraft observations. Finally, the results of the study on coherent thermal structures are also given.

Finally, chapter 6 concludes the previous chapters and gives the recommendations made for possible future research.

2 Theoretical Background

2.1 Introduction

In order to study shallow cumulus, one will need to use some general aspects of meteorology, in which thermodynamics play an important role. Therefore, in this chapter some basic principles and definitions that can be useful in the analysis and interpretation of the process of shallow cumulus convection, will be presented. For a more detailed overview of used thermodynamic quantities and the derivation of them we refer to appendix A, or e.g. Iribarne and Godson (1973). Furthermore, in section 2.6, a brief look into wavelet analysis will be taken.

2.2 The atmospheric boundary layer

2.2.1 Introduction

The atmospheric boundary layer (ABL) is defined as the layer where dynamics and physics of air are influenced by the earth's surface. Characteristics of the surface, like roughness, land use, albedo or orography, are important in driving the processes in the boundary layer. A typical value for the boundary layer height is 500 – 1500 metres. That is about 10% of the height of the troposphere.

2.2.2 Development of a mixed layer

In the morning, when the sun starts warming the earth, upward pointed fluxes of heat and moisture develop at the surface. Turbulent eddies with length scales of a few millimetres to a few hundred metres, mix conserved quantities, like potential temperature and specific humidity, throughout the boundary layer. Furthermore, eddies that rise out of the boundary layer into the free troposphere, will take warm and dry air with them when they drop back into the boundary layer. This process is called *entrainment*. If we assume the supply of air by the mesoscale circulation to be very small, a so-called *mixed layer* will develop.

The mixed layer will grow during the day, due to the continuous upward fluxes at the earth's surface in combination with the entrainment of warm and dry air at the top of the boundary layer. This thin layer at the top of the boundary layer is called *entrainment zone* or *inversion layer*.

2.2.3 Thermals

Due to the continuous incoming radiation of the sun, in the lowest 50 – 100 metres of the ABL a superadiabatic *surface layer* can develop. This is caused by heating of the soil by solar shortwave radiation. In this surface layer the air will be potential warmer and contain more moisture than the air above, i.e. it is less dense. The atmosphere will tend to smooth down this unstable situation by taking away the *buoyancy* of the air in the surface layer. This can only be achieved if this air rises from the surface and mixes with air at higher levels.

In case of heterogeneous warming, there may be places that have so much buoyancy with respect to their environment, such that an air parcel at that place will spontaneously rise from the surface. Because of continuity, these so-called *thermals* will induce downward motions on other locations. Rising thermals are very local and small phenomena, this explains why vertical speeds in these

thermals can reach values of $5ms^{-1}$, depending on the strength of the upward fluxes and the ABL height.

A rising thermal is generally characterized by a positive anomaly in temperature, humidity and vertical speed. For selecting thermals, a lot of different criteria are used. For example, in Lenschow and Stephens (1980), a thermal is selected if on a length scale of at least 25 metres the specific humidity deviates a half time the standard deviation from the average value.

2.3 Thermodynamic quantities

Virtual temperature is defined as the temperature that dry air must have to obtain the same density as the moist air considered:

$$T_v = T(1 + 0.61q_v - q_l) \tag{2.1}$$

with q_v the specific humidity of water vapor and q_l the amount of liquid water. If we now correct this temperature for adiabatic pressure changes – that causes cooling in case of expansion or warming in case of compression – the virtual potential temperature θ_v is introduced, which is defined as

$$\theta_v = T_v \Pi^{-1} \tag{2.2}$$

where Π is the Exner function

$$\Pi = \left(\frac{\overline{p}}{p_0} \right)^{R_d / c_p} \tag{2.3}$$

It is assumed that the pressure in the parcel, p_u, is equal to the environmental pressure $\overline{p}$. The reference state pressure of 1000 hPa is denoted by p_0, g is the gravitational constant with a value of $9.81ms^{-2}$, whereas $R_d = 287.05Jkg^{-1}K^{-1}$ is the gas constant for dry air and $c_p = 1004Jkg^{-1}K^{-1}$ is the specific heat capacity at constant pressure for dry air.

Because of the inverse proportionality of θ_v to density, we can write the buoyancy force that acts on an air parcel per unit of mass as

$$F_B = -\rho_u g \frac{\rho_u - \overline{\rho}}{\overline{\rho}} \simeq \rho_u g \frac{\theta_{vu} - \overline{\theta}_v}{\overline{\theta}_v} \tag{2.4}$$

In this equation, ρ_u and $\overline{\rho}$ are the densities of the air parcel and the environment, respectively. Furthermore, θ_{vu} and $\overline{\theta}_v$ are the corresponding virtual potential temperatures. The difference $\theta_{vu} - \overline{\theta}_v$ is the virtual potential temperature excess that is commonly denoted by $\Delta\theta_v$. If we now displace an air parcel dry-adiabatic (i.e. without condensation effects) at a certain height over an infinitesimal distance δz, we obtain the following equation by using the conservation of θ_{vu}:

$$\rho \frac{\partial w}{\partial t} = \rho \frac{d^2(\delta z)}{dt^2} = F_B(z + \delta z) - F_B(z) \approx \frac{dF_B}{dz} \delta z \tag{2.5}$$

During the ascent, the air parcel will cool due to expansion. As a result, the saturation value of specific humidity in the parcel decreases. The level at which the virtual temperatures of the air parcel and the environment become equal, is called *level of neutral buoyancy* (LNB). Subsequently, if the air parcel becomes saturated, it has reached its *lifting condensation level* (LCL). At this level the water vapor specific humidity q_v is exactly the same as the value of the saturation specific humidity q_s (see section 2.4). In general, it holds for the total specific humidity that

$$q_t \equiv q_v + q_l \tag{2.6}$$

Above the LCL, conversion of water vapor into liquid water takes place and cloud growth starts. The sub-cloud thermal becomes a cumulus cloud (Cu) by definition. The LCL is the most common estimate of cloud base height, therefore. In Figure 2.1, a schematic overview of the structure of the cumulus-topped boundary layer is presented. The total specific humidity q_t is the first conserved quantity we recognize under adiabatic displacements, i.e. the total amount of liquid water an air parcel contains does not change, provided that there is no exchange with its environment.

The air parcel can have a negative buoyancy at the LCL, due to the low virtual potential temperature with respect to the environment. This entails that the air parcel must have sufficient kinetic energy, if it wants to rise above the LCL. Condensation behaves as an engine for a further rise in this area, since it heats the air parcels. Above cloud base, two kinds of further ascents are possible. If the lapse rate (section 2.4) of the environment is larger than the wet-adiabatic lapse rate the updraft is following because of the latent heat release, the parcel will keep its negative buoyancy with respect to the environment and the vertical motion will stop. The cloud that develops in this case is called a *forced cloud*.

On the other hand, it is also possible that the environment has a lapse rate that is less than the wet-adiabatic lapse rate. In that case, the parcel might reach its *level of free convection* (LFC). This is the level at which the virtual potential temperatures of the parcel and the environment are exactly equal. If this level is reached, there are no thresholds for the parcel anymore to become a full-grown cumulus cloud, due to the fact that the buoyancy obtains a positive value again. The cloud that develops in this case is called an *active cloud*.

Passive clouds are the remnants of active clouds that have lost connection with heat, moisture and momentum input from the sub-cloud layer. This can be possibly caused by warm, dry downdrafts that descend along the cloud. Finally, a passive cloud will evaporate and disappear, in addition to which the speed of evaporation is dependent on the environmental humidity.

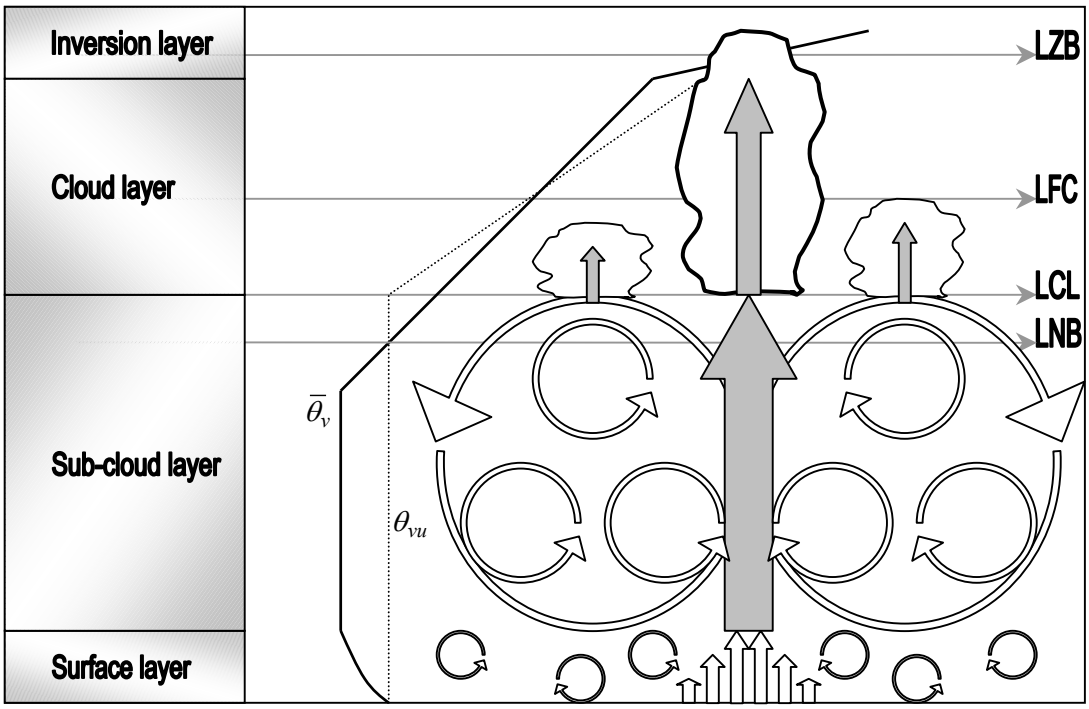

FIGURE 2.1 Schematic overview of the cumulus-topped boundary layer (CTBL). In the figure, typical profiles for mean (solid) and parcel (dashed) virtual potential temperatures are presented. The inhomogeneity of the surface (white arrows at the surface) produces turbulent eddies with various length scales, as depicted. The resulting updraft that starts to rise, is denoted by the grey arrow. The clouds on the left and the right of the active cumulus cloud we consider, are forced clouds, i.e. negatively buoyant and still rising towards the LFC.

Because of the low cloud cover of shallow cumulus (typically 20% - 40%), most of the time the sun prevails in heating the earth's surface. Hence new thermals can rise and might develop new cumuli. As a result, the low cloud cover more or less guarantees the maintenance of a cumulus-topped boundary layer.

2.4 Local stability

2.4.1 On lapse rates and stability

The local stability of the atmosphere for condensing thermals can be considered by using the *lapse rate* of the virtual potential temperature in the environmental air:

$$\Gamma = \frac{\partial \overline{\theta_v}}{\partial z} \tag{2.7}$$

This lapse rate can be compared with standard situations that hold for dry-adiabatic and wet-adiabatic situations, for unsaturated and saturated air parcels respectively. The lapse rate for dry-adiabatic displacements, Γ_d, is zero by definition, while the lapse rate for wet-adiabatic displacements, Γ_m, is positive due to the latent heat release of the condensation process. It has a typical value of about $4K/km$, for ambient circumstances $T = 288K$, $p = 1000hPa$ and $q_v = 11g/kg$.

Now, we discriminate between three typical situations:

- $\Gamma < \Gamma_d \Leftrightarrow$ *absolutely unstable*

In the absolutely unstable regime the vertical displacement of an air parcel will lead to a positive buoyancy of this air parcel, which will be followed by a further rise. This situation only occurs in the surface layer, irrespective of the saturation of the air parcel.

- $\Gamma_d < \Gamma < \Gamma_m \Leftrightarrow$ *conditionally unstable*

In a conditionally unstable situation the stability is dependent on the fact whether the air parcel is saturated or not. For dry-adiabatic displacements the atmosphere is stable, while for wet-adiabatic displacements it is unstable. This situation typically occurs in the cloud layer.

- $\Gamma > \Gamma_m \Leftrightarrow$ *absolutely stable*

In the absolutely stable regime the vertical displacement of an air parcel will lead to a negative buoyancy, which will be followed by a subdued vertical motion. This situation typically occurs in a stable boundary layer or in the inversion layer.

2.4.2 CAPE

The vertical path between the LNB and LFC can, as mentioned above, only be passed if enough kinetic energy is available in the air parcel. This is completely dependent on the extent of stability in the sub-cloud layer. To gain a better insight in this concept, you can make use of *convective available potential energy* (CAPE). This is an integrated stability function that is defined as:

$$CAPE(z, z_r) \equiv \int_{z_r}^{z} F_B dz = R_d \int_{p(z)}^{p(z_r)} (T_{vu} - \overline{T_v}) d \ln p \tag{2.8}$$

In (2.8), z_r and z are the release height and the height of an air parcel, respectively. Between the second and third step in this equation, the validity of hydrostatic equilibrium is assumed.

The level at which the buoyancy of an air parcel becomes negative again, is the level at which the virtual potential temperatures of the air parcel and the environment become equal. This is called the 'level of zero buoyancy' (LZB). It is possible that the parcel still rises somewhat, into the inversion layer. If a parcel indeed does so, one talks about an *overshoot*. In this case convection can still occur, despite of the stable situation in the inversion layer, which is characterized by a strong increase in temperature and a decrease in humidity with height. Nevertheless, the LZB is a well-known estimate for the cloud top height. Above the inversion layer, a relatively warm and dry *free atmosphere* is present.

2.5 Condensation effects

Condensation takes place if the saturation value for specific humidity is exceeded. Calculating this saturation value out of the known variables, we use a condensation scheme presented in Sommeria and Deardorff (1977). First of all, the liquid water temperature T_l is calculated:

$$T_l = T \exp(-\frac{Lq_l}{c_p T}) \tag{2.9}$$

which can be written as $T_l = T - (L/c_p)q_l$ after a Taylor expansion, because the term in the exponent is in general much smaller than 1. The latent heat of vaporization is denoted by L and has a value of $2.5 \times 10^6 J/kg$.

The liquid water temperature can be interpreted as the temperature an air parcel will have if you remove all the liquid water from it, the term $-(L/c_p)q_l$ exactly corrects for the amount of latent heat that is released in the case of condensation at which a certain amount of liquid water q_l is formed. For convenience reasons, the liquid water potential temperature $\theta_l = \theta \exp(-Lq_l/c_p T)$ is often used. This temperature is conserved under moist adiabatic processes, including phase changes. It therefore is very useful, because diabatic processes such as lateral mixing of an updraft are easier to recognize if it is evaluated during its rise from the surface.

Subsequently, the saturation vapor pressure for this liquid water temperature is calculated with the Tetens formula (Murray, 1967):

$$e_s(T_l) = e_0 \exp[a\frac{(T_l - T_0)}{(T_l - b)}] \tag{2.10}$$

with $e_0 = 610.78Pa$, $T_0 = 273.16K$ as the temperature at the triple point, $a = 17.27$ and $b = 35.86$.

With the derived saturation vapor pressure, one can calculate the saturation specific humidity with Dalton's law:

$$q_{sl} \equiv q_s(T_l, \overline{p}) = \frac{\varepsilon_0 e_s(T_l, \overline{p})}{\overline{p} + (\varepsilon_0 - 1)e_s(T_l, \overline{p})} \tag{2.11}$$

with $\varepsilon_0 = R_d / R_v = 0.622$ and $\overline{p}$ the atmospheric pressure.

However, the saturation value of specific humidity is now computed at the liquid water temperature T_l, whereas we want to know this value at the 'normal' air temperature T. We do not yet know how much liquid water is present, therefore we have to make use of

$$T - T_l = \frac{L}{c_p} q_l \tag{2.12}$$

in combination with a Taylor expansion of $q_s(T)$ around the point $q_s(T_l)$:

$$q_s(T, \overline{p}) \simeq q_s(T_l, \overline{p}) + (T - T_l)\frac{\partial q_s}{\partial T}_{T=T_l} \tag{2.13}$$

Concerning the Clausius-Clapeyron equation, the derivative in the second term on the r.h.s. of (2.13) can be obtained:

$$\frac{\partial q_s}{\partial T}_{T=T_l} = \frac{\varepsilon_0 L q_{sl}}{R_d T_l^2} \tag{2.14}$$

Finally, the saturation specific humidity at a certain temperature T and pressure $\overline{p}$ can be found by combining (2.13) and (2.14):

$$q_s(T,\overline{p}) = q_{sl}\frac{1+\beta_1 q_t}{1+\beta_1 q_{sl}} \tag{2.15}$$

where

$$\beta_1 = \varepsilon_0\left(\frac{L}{R_d T_l}\right)\left(\frac{L}{c_p T_l}\right) \tag{2.16}$$

For saturated air, the amount of liquid water q_l can now be determined as the difference between the total specific humidity q_t and the calculated saturation specific humidity q_s, provided that this difference is positive. It should be stressed that equation (2.15) only holds for air that already contains liquid water, i.e. $q_l > 0$. In case of an unsaturated air parcel ($q_l = 0$), it reduces to $q_s(T,\overline{p}) = q_{sl}$ because of $T_l = T$.

2.6 Wavelet analysis

2.6.1 Introduction

Wavelet analysis is a very useful mathematical tool in analyzing series of data in e.g. time or space. It is a strongly developing technique that has recently been used in various studies concerning geophysical topics, like e.g. studies on the El Niño-Southern Oscillation (Gu and Philander, 1995; Wang and Wang, 1996), atmospheric cold fronts (Gamage and Blumen, 1993), the dispersion of ocean waves (Meyers et al., 1993) and coherent structures in turbulent flows (Farge, 1992; Krusche and de Oliveira, 2004). In spite of what a Fourier transform can do with a time series, wavelet analysis offers a complete decomposition of the signal, so one will be able to determine the dominant modes of variability as well as how those modes vary in time. In the study of the evolution of rising thermals in the lower ABL, this seems to be convenient. For a complete and clearly written paper about wavelet analysis, we refer to Torrence and Compo (1998).

2.6.2 Theory

We consider a time series, x_i, with $i = 0,1,...,N-1$, where $t_{i+1} - t_i = \delta t$ is the time spacing, then a function $\psi_0(\eta)$, with η a non-dimensional time parameter, can be a so-called mother wavelet function if it obeys two conditions (Farge, 1992):

- it must have a zero mean
- it must be localized in time and frequency space

An example is the Morlet wavelet function, which has the form:

$$\psi_0(\eta) = \pi^{-1/4} e^{i\omega_0 \eta} e^{-\eta^2/2} \tag{2.17}$$

with the wave component $e^{i\omega_0\eta}$ and the Gaussian component $e^{-\eta^2/2}$. Furthermore, ω_0 is the non-dimensional frequency.

Another example of a wavelet function is the DOG (Derivative Of a Gaussian) wavelet, which is defined as:

$$\psi_0^{(m)}(\eta) = \frac{(-1)^{m+1}}{\sqrt{\Gamma(m+\frac{1}{2})}} \frac{d^m}{d\eta^m}(e^{-\eta^2/2}) \tag{2.18}$$

where Γ represents the Gamma function. The function $\psi_0^{(2)}$ is the so-called Marr or Mexican Hat wavelet function. An illustration of this mother wavelet function is presented in Figure 2.2. Note that its shape reminds to some extent of the shape of a thermal structure in the surface layer, with periods with lower values for e.g. T, q next to the structure. In several studies (e.g. Weijers et al., 1995; Chen et al., 2003), the shape of thermals has been described as so-called ramp structures, i.e. gradually rising values with sudden drops towards negative anomalies.

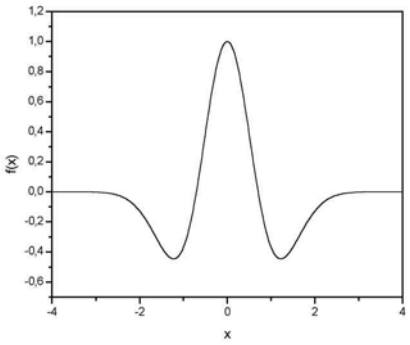

FIGURE 2.2 A representation of the Mexican Hat or DOG2 wavelet function.

The wavelet transform is defined as the convolution of x_i with the normalized and complex conjugated version of the mother wavelet function $\psi_0(\eta)$, i.e. $\psi*$:

$$W_i(s) = \sum_{i'=0}^{N-1} x_{i'} \psi * \left[\frac{(i' - i)\delta t}{s} \right] \tag{2.19}$$

where i denotes the localized time index. By varying the wavelet scale s and calculating $W_i(s)$ for all the points in the time series, a picture can be constructed that contains information about the amplitude of a periodic feature versus its scale, as well as how this feature evolves in time. Because most of the mother wavelet functions – and their transformations – are complex, we define the wavelet power spectrum as $|W_i(s)|^2$.

Numerous different wavelets exist, in order to analyze data sets with different characteristics. The choice of wavelet function is dependent on the expected (or known) behaviour of the time series, concerning oscillation period, character of peaks and discontinuities and the smoothness of the time series. Furthermore, it is important that you realize that time and frequency resolutions cannot both be very good at the same time. A narrow (in time) function will have good time resolution but poor frequency resolution, while it is the other way around with a broad (in time) function (Torrence and Compo, 1998).

The choice of wavelet scales is also very important if you want to perform a good wavelet analysis. First of all, it is convenient to write the scales as fractional powers of two:

$$s_j = s_0 2^{j\delta j} \tag{2.20}$$

with $j = 0,1,...,J$. The smallest resolvable scale in the analysis is denoted by s_0, while the largest scale is equal to $J = dj^{-1}\log_2(N\delta t / s_0)$. The value of s_0 should be chosen such that the equivalent period in the Fourier domain is about $2\delta t$. Furthermore, a typical value for the wavelet scale interval δj is 0.5 for the Morlet wavelet functions, while other wavelet functions are able to handle a greater value for δj.

Finally, we introduce the global wavelet spectrum as the time-averaged value over all the local wavelet power spectra:

$$\overline{W}^2(s) = \frac{1}{N}\sum_{i=0}^{N-1}|W_i(s)|^2 \tag{2.21}$$

This can be interpreted as the horizontal slice you can make through a wavelet power spectrum plot, in time direction. By making use of the global wavelet spectrum, one can qualitatively analyze the signal power distribution on the scale domain at a glance.

3 Used data

3.1 Introduction

The data described in this chapter are twofold. First of all, we use data – mean vertical profiles of thermodynamic quantities and surface conditions – to diagnose the offline model that is presented in chapter 4. This mainly concerns measurements done at or near the meteorological mast in Cabauw and measurements derived by the so-called Integrated Profiling Technique (IPT). On the other hand, evaluation of model outcome is carried out with data collected by lidar instruments and aircraft. As mentioned before, the BBC2 campaign that took place in May 2003 near Cabauw offers a great opportunity to gather all of these desired measurements more or less simultaneously. This campaign is discussed in the next section. For photographs of instruments that are presented in this chapter, we refer to appendix B.

3.2 Baltex Bridge Campaign

The 2nd Baltex Bridge Campaign (BBC2) was jointly organized by the Royal Dutch Meteorological Institute (KNMI) and the University of Bonn, in the period 3 May-24 May 2003. It was a sequel of the successfully held 1st Baltex Bridge Campaign (August - September 2001). Around 25 institutes from 6 countries (The Netherlands, Germany, France, United Kingdom, Poland and Sweden) participated and brought a substantial amount of their instruments and scientific and technical staff to The Netherlands. Measurements during both campaigns were carried out around the central meteorological measurement facility of KNMI at Cabauw.

The Baltex Bridge Campaigns have been conducted in the BALTEX (Baltic Sea Experiment) framework, which is the European continental-scale experiment within GEWEX (Global Energy and Water Cycle Experiment). In general, this is a sub-programme of the World Climate Research Programme (WCRP) (Simmer et al., 2004). The focus in both BBC campaigns was on continental clouds, primarily on boundary layer clouds. Spatial variability, vertical structure and diurnal cycle of these clouds were the main topics. Besides clouds itself, aerosols and radiative transfer, as well as development and testing of measurement techniques, belonged to the BBC topics. For the BBC2 campaign, an additional focus on precipitation and its small-scale variability was made.

All measurements that were collected during the BBC2 campaign are subjected to a quality control and afterwards stored in a central database at KNMI. Also some end products that have been produced by the analysis of raw data, are available. In the next sections, measurements that are a part of this database and have been used for this particular study, are described.

3.3 Cabauw mast[1]

3.3.1 Introduction

The Cabauw meteorological mast ($N51^{\circ}58.223'$ $E4^{\circ}55.575'$; WMO ID 06243) is located near the village of Lopik, in the western part of The Netherlands. The 213 m high tower was built in 1972 by KNMI, especially for research of possible relations between the state of the ABL, the land surface

[1] For more information about the meteorological mast at Cabauw, visit www.cesar-observatory.nl . For more information about instruments and data, visit www.knmi.nl/~bosveld .

conditions and the synoptic situation. Since May 2002 three universities and five research institutes collaborate in CESAR (Cabauw Experimental Site for Atmospheric Research), a project to develop Cabauw into a leading scientific international site on the terrain of remote sensing, climate monitoring and boundary layer research.

The Cabauw site was chosen, first of all because of the representative Dutch polder landscape and because of the mostly agricultural land use in the nearby region. Furthermore, the elevation in the region is minimal and in a range of 40 kilometres, four major weather stations – e.g. De Bilt (06260) – are present. These stations can support and check measurements done at Cabauw and may give reason to spatially correlate measurements.

The mast mainly consists of a 2 m wide tube, with a small elevator inside. It is held by four steel cables and has booms in three directions every 20 metres. On the ends of these 9.4 m long booms, the instruments are mounted. In the pasture around the mast, a lot of instruments of various research groups are (permanently or temporarily) erected. At the base of the mast a building is located, for data collection and maintenance of the instruments.

3.3.2 Measured variables

Temperature and dewpoint temperature
In the mast, air temperature and dewpoint temperature are measured at seven levels; 10, 20, 40, 80, 140 and 200 m. For the levels at 40, 80, 140 and 200 m, the measurements occur on the main mast itself, while for the levels at 2, 10 and 20 m, the measurements take place at a separate profiling mast, south of the Cabauw building. Especially after periods of rain, dew and fog, there is an overestimation of dewpoint temperature and subsequently of specific humidity, due to wet shielding of the Vaisala sensor (Bosveld, 2002).

Air temperature is measured with the KNMI Pt500-element (accuracy $0.1^{\circ}C$; resolution $0.1^{\circ}C$) in an unventilated KNMI temperature hut. Dewpoint temperature is measured with a Vaisala HMP243 heated relative humidity sensor (accuracy 3.5%; resolution $0.1^{\circ}C$) with a metal filter in a separate Vaisala unventilated hut.

Wind speed and wind direction
In the mast, wind speed and wind direction are measured at six levels, 10, 20, 40, 80, 140 and 200 m. For the levels at 40, 80, 140 and 200 m, wind direction is measured at three booms and wind speed is measured at two booms. Concerning the levels at 10 and 20 m, wind speed and wind direction are measured at two separate masts, located north and south of the Cabauw building. Depending on wind direction, the instruments that are expected to measure the undisturbed wind with the highest quality, are selected every 10 minutes.

Wind speed is measured with the KNMI cup-anemometer (accuracy $0.5ms^{-1}$; resolution $0.1ms^{-1}$), while wind direction is measured with the KNMI wind vane (accuracy 3°; resolution 1°).

Surface pressure

Surface pressure is measured with a Paroscientific 1016B-01 (accuracy $0.1hPa$; resolution $0.1hPa$), at the AWS located 200 m southwest of the mast.

Turbulent fluxes

Turbulent fluxes of heat and moisture are measured at five levels, at 1, 5, 60, 100 and 180 m, by the instruments as presented in Table 3.1. During BBC2, only the levels located at 5 and 180 m were operational.

Height	Location	Sonic anemometer	H_2O/CO_2 probe	Operational
1 m	200 m S of mast	Kaijo-Denki TR90AH	Ly-Alpha hygrometer	2002-2003
5 m	200 m S of mast	Kaijo-Denki TR61	KNMI IR fluctuation	Permanent
60 m	Mast	Kaijo-Denki TR61	Licor open path IR	200308-200512
100 m	Mast	Gill Solent	Licor open path IR	200305-200512
180 m	Mast	Kaijo-Denki TR61	IR fluctuation	200208-200512

TABLE 3.1 Overview of instrument deployment for deriving turbulent fluxes.

The 60 and 180 m levels are operated in cooperation with USA-NSF, while the 100 m level is operated in cooperation with Alterra Wageningen.

The sonic anemometers are able to measure the three components of the 3D wind vector $\vec{V} = (u, v, w)$. Along each of the three axis of the anemometer, two ultrasonic signals are transmitted in opposite directions. Hence the special geometry, with the six antennas as depicted in appendix B. The thermometer and the hygrometer, which are located next to the sonic anemometer, measure air temperature and specific humidity, for the determination of the heat and moisture fluxes. These two measured variables can also be used for calculation of the speed of propagation of sound waves, that is equal to $c^2 = \gamma_h R_d T(1 + 0.51q)$ with the specific heat ratio $\gamma_h = 1.4$ (Schotanus et al., 1983). A typical value for c in air is $340ms^{-1}$. If we denote the path length by d and the wind speed along one of the anemometer axes by U_{a_i} ($i = 1,2,3$), the transit time of the first signal is equal to $t_i^A = d/(c - U_{a_i})$, while the signal in the opposite direction has a transit time $t_i^B = d/(c + U_{a_i})$. Typical values of d are $0.20m$ for the Kaijo-Denki AR61 and Gill Solent anemometers, while the Kaijo-Denki AR90AH at the 1 m level has a path length $d = 0.05m$.

The respective wind component can now be retrieved as:

$$U_{a_i} = \frac{d}{2}\left(\frac{1}{t_i^A} - \frac{1}{t_i^B}\right) \tag{3.1}$$

Subsequently, we obtain the orthogonal wind vector by calculating

$$\begin{pmatrix} u \\ v \\ w \end{pmatrix} = M \begin{pmatrix} U_{a_1} \\ U_{a_2} \\ U_{a_3} \end{pmatrix} \tag{3.2}$$

where M is a 3×3 transformation matrix with coefficients containing information about e.g. anemometer geometry and orientation.

Generally, the instruments mentioned in Table 3.1 are mounted on a 1 m long thin cylinder to avoid flow obstruction. Between the instruments and the boom, an inclinometer is mounted. For the 1 and 5 m levels, a rotator is fixed to the cylinder. This rotator turns the cylinder with its instruments in the wind direction every two hours, induced by an automatic wind direction tracking system.

Data logging and processing
Data from the temperature, wind and pressure instruments are logged with a so-called SIAM (Sensor Intelligent Adaptation Module). Every 10 minutes, the values for mean, minimum, maximum and standard deviation are stored. Turbulence instruments are logged with a frequency of $10 Hz$. Both the raw data as the processed 10 minute values for mean, minimum, maximum, standard deviation and covariances are stored.

The stored data are transmitted to De Bilt where they become a part of the MOBIBASE database. Here, quality control is performed on the incoming data.

3.3.3 Model initialization
An overview of the Cabauw mast data, used for profiles that are presented to 1D SPAM every 10 minutes (section 4.4), is presented in Table 3.2.

Input name	Symbol	Description	Availability
TP***	θ	Potential temperature ($^\circ C$)	2, 10, 20, 40, 80, 140, 200 m
TA***	T	Temperature ($^\circ C$)	2, 10, 20, 40, 80, 140, 200 m
TD***	T_d	Dewpoint temperature ($^\circ C$)	2, 10, 20, 40, 80, 140, 200 m
F***	ff	Absolute wind speed (ms^{-1})	10, 20, 40, 80, 140, 200 m
D***	dd	Wind direction ($^\circ$)	10, 20, 40, 80, 140, 200 m
CP0	p_{srf}	Surface pressure (hPa)	-
WT***	$\overline{w'T'}$	Vertical heat flux ($^\circ C m s^{-1}$)	1, 5, 60, 100, 180 m
WQ***	$\overline{w'q'}$	Vertical moisture flux ($gmkg^{-1}s^{-1}$)	1, 5, 60, 100, 180 m

TABLE 3.2 Overview of available Cabauw tower data, useful to initialize the 1D SPAM

Variables are interpolated to the desired vertical grid levels. If only mast observations are used for initialization, the profile of θ (and for technical reasons for ff and dd) is prescribed constant for model levels above the tower top of 200 metres, as if it is a profile in a well-mixed layer. The specific humidity is computed with Dalton's law:

$$q_v = \frac{\varepsilon_0 e}{p + e(\varepsilon_0 - 1)} \tag{3.3}$$

after the calculation of the vapor pressure e at each measuring level from the values of the dewpoint temperature T_d:

$$e = e_0 \exp\left[-\frac{L}{R_v}\left(\frac{1}{T_d} - \frac{1}{T_0}\right) \right] \tag{3.4}$$

with $R_v = 461.50 Jkg^{-1}K^{-1}$, the gas constant for water vapor.

3.4 Radiosondes

During BBC2, KNMI launched (in cooperation with the Dutch Army) at least three RS90 radiosondes a day, with time intervals of about 3 hours. For this study, the radiosonde data are very useful in the quality checking procedure of mast and IPT initialization data. Furthermore, the data plays a role in debugging the initialization routine. In Table 3.3, the measurements of the RS90 sondes are listed.

Symbol	Variable
p	Pressure (hPa)
z	Geopotential height (m)
T	Temperature ($^\circ C$)
T_d	Dewpoint temperature ($^\circ C$)
RH	Relative humidity (%)
ff	Absolute wind speed (ms^{-1})
dd	Wind direction ($^\circ$)

TABLE 3.3 Overview of available RS90 radiosonde data.

3.5 Aircraft measurements

During BBC2, in-situ measurements were carried out with various instruments mounted on three research aircraft. The German institute IfT Leipzig participated with its Partenavia, NERC (United Kingdom) with its Dornier and CNRM (France) flew its Merlin-IV research aircraft to The Netherlands. A total of 31 flights was carried out on 14 days, all departing from Rotterdam Airport (Zestienhoven).

An extensive flight plan was made for the three aircraft, in order to gather desired measurements as efficiently as possible. Flight time is very expensive and should therefore be used carefully. A special BBC2 forecast that was made by KNMI every morning helped in achieving satisfactory results.

The Merlin aircraft is the most interesting for our purposes, because this aircraft was planned on flying vertical profiles through boundary layer clouds, if possible. The other ones (Dornier, Partenavia) were supposed to fly above the clouds and were more focussed on measuring radiative properties of clouds. Above all, the Merlin was equipped with a lot of very useful instrumentation, under which fast probes for measurements of pressure, temperature, humidity and vertical velocity and two devices for measurements of in-cloud liquid water content. Furthermore, radiation instruments were mounted, e.g. an Eppley for longwave up- and downward radiation and a new

radiation instrument of the IMAU (DIRAM). An overview of the used instruments on board of the Merlin during the BBC2 campaign is shown in Table 3.4.

Instrument	Parameter	Frequency	Accuracy
GPS receiver	Position	10 Hz	-
Various fast temperature, humidity, pressure and vertical velocity probes	T, q, p, w	10 Hz	-
Rosemount PT50/100 probes	Temperature	10 Hz	0.5 K
Lyman-Alpha hygrometer	Humidity	10 Hz	4%
Gerber PVM-100	Liquid water	200 Hz	5%
King probe	Liquid water	200 Hz	15%

TABLE 3.4 Overview of used Merlin IV instruments during this study.

3.6 Remote sensing

Remote sensing observations have gained an enormous amount of popularity during the last decades. Nowadays, it is unimaginable that an atmospheric research group or commercial service in the field of meteorology works without radar, lidar or satellite-based measurements.

For additional information about the state of the atmosphere and the presence of clouds, we used observations of two KNMI remote sensing instruments, which are permanently located at the Cabauw experimental site.

A lidar (LIght Detection And Ranging) works with the same principle as a radar, but uses optical signals to do its measurements; a short pulse of laser light is emitted and the reflections of the light on air molecules and particles are observed. The height resolution is obtained by measuring the time lapse between emission of the laser pulse and the reception of the echo. Signal averaging is often applied, due to very weak optical echoes. Thereby it is assumed that the atmosphere is frozen during the measurement time.

In Cabauw, a Vaisala CT75K lidar ceilometer is located. This lidar can measure up to 3 cloud bases and works with a wavelength of 905 nm. The measurement range is up to 11250 metres, with a vertical resolution of 30 m. The integration time of the instrument is 30 s.

Since May 2001, the RIVM is also present in Cabauw with its 1064 nm lidar. This lidar can measure up to 10 cloud bases and has a measurement range of 150 – 15000 metres with a resolution of 3.75 m. The measurement integration time of 1 s is adjustable. Furthermore, to avoid unwanted effects due to averaging of rapidly changing cloud properties, the RIVM lidar has been equipped with a non-averaging measurement scheme.

The CT75K lidar shows a cloud base bias of one to two gates compared to the RIVM lidar, which corresponds with a difference in cloud base estimate of 30-60 m. This is caused by the treshold method that is used to make the estimate, considering the backscatter profile.

3.7 Integrated Profiling Technique (IPT)

The Integrated Profiling Technique (IPT) of the University of Bonn, that was operational with BBC data (August/September 2001) for the first time, combines simultaneous measurements of various remote sensing and profiling instruments in order to obtain physically consistent profiles of temperature, humidity and liquid water content in the column above Cabauw (Löhnert et al., 2004).

The measurements that are used in this method are presented in Table 3.5. We should remark here that the output of the single column microphysical cloud model DCM is interpreted as a measurement.

Instrument	Derived variables
GKSS 95 GHz cloud radar MIRACLE	Z, Doppler velocity, Doppler spectral width
MICCY/HATPRO microwave radiometer	T, q, q_l vertical profiles
Vaisala CT75K lidar ceilometer	Cloud base height
RS90 radiosonde (De Bilt 06260)	T, q, p vertical profiles
Temperature/humidity sensor	T and q at ground level
DCM microphysical cloud model	Liquid drop size spectra

TABLE 3.5 Overview of instruments and input needed for operation of the Integrated Profiling Technique (IPT) during the BBC1 and BBC2 campaign.

After application of so-called optimal estimation theory, the IPT method gives its output with a vertical resolution of 250 metres in the lowest 5 kilometres of the atmosphere. Between 5 and 10 kilometres, IPT has a vertical resolution of 500 metres, while between 10 and 30 kilometres the output is given every 5 kilometres. For the derived profiles of temperature, specific humidity and liquid water content, an additional file is automatically generated in which the uncertainties in the corresponding variables are presented.

For (one dimensional) model evaluation, it is very convenient to use IPT data for initialization. It gives a sort of best guess observation of vertical profiles of temperature, specific humidity and LWC in the column above the experimental site. Above that, the data set is temporal very dense, except for days with a significant amount of daytime precipitation or non-operational input instruments. In ideal circumstances (i.e. no precipitation, all instruments working), about two IPT output records are made every minute.

In the generation of initialization profiles for the 1D SPAM model (section 4.4), the Integrated Profiling Technique plays a major role. First of all, profiles of T and q are interpolated to the chosen vertical model grid, after which a temporal interpolation puts the profiles in the correct model time grid.

4 Models and methods

4.1 Introduction

Because of computational limitations, the horizontal resolution of most Numerical Weather Prediction (NWP) models is at least about 10 kilometres. Convection, and especially shallow cumulus convection, acts on horizontal length scales of at most 1 kilometre and thus can not be explicitly solved. Therefore, a sub-grid process like convection should be parameterized in terms of the large-scale flow, as we have observed in chapter 1. In this chapter, the new trigger function (Jakob and Siebesma, 2003) will be discussed, as well as an offline parcel model (1D SPAM) that was used to test this function. In the last section a method for the identification of coherent thermal structures in the boundary layer is presented.

4.2 On the triggering of cumulus convection

4.2.1 Introduction

There has been a lot of research during the past decades on the accurate description of cumulus convection in NWP models and GCMs. The trigger function – that is part of every convection scheme – can be seen as a decision process prior to the occurrence of convection. With the publication of Jakob and Siebesma (2003), a new step forward is made in solving the cumulus triggering problem. Previous schemes based on the mass-flux approach were starting their calculations at cloud base, while now this approach is being used for a description for the boundary layer and the cloud layer as a whole (section 1.3). After all, why would updrafts that lead to the forming of clouds behave in another way than the convective clouds themselves, considering the lateral mixing of properties with their environment?

4.2.2 Mass-flux approach

The mass-flux approach is often made in cumulus transport studies. In the construction of the tendency of a mean thermodynamic property $\overline{\phi}$, the vertical gradient of the flux $\overline{w'\phi'}$ is an important source term. Therefore, one would like to parameterize this flux as accurately as possible. The mass-flux approach is based on the idea that the vertical motion pattern in the boundary layer can be split in two parts: one with strong, narrow updrafts with a property ϕ_u in a very small fractional area a_u ($= A_u / A$ with A the absolute total area for averaging) and one with weak downward motion in the surroundings, denoted by the fractional area $(1 - a_u)$. The average value of a field ϕ can hence be written as:

$$\overline{\phi} = a_u \phi_u + (1 - a_u)\phi_e \tag{4.1}$$

The subscripts u and e refer to the updraft and environmental value, respectively.

Subsequently, the turbulent flux of a field ϕ can be split into three parts (Siebesma and Cuijpers, 1995):

$$\rho\overline{w'\phi'} = \rho a_u \overline{w'\phi'}_u + \rho(1 - a_u)\overline{w'\phi'}_e + \rho a_u (w_u - \overline{w})(\phi_u - \phi_e) \tag{4.2}$$

The r.h.s. contains the following terms: (1) updraft turbulence, correlated fluctuations with respect to the updraft average; (2) environmental turbulence, correlated fluctuations with respect to the environmental average; (3) contribution due to the organized updrafts with respect to the environment. Next, we introduce an entrainment rate E and a detrainment rate D. These rates describe lateral mass exchange between the updraft and its environment and vice versa, respectively. For example, a higher value of E leads to more inflow of environmental air into the updraft. A schematic picture of the mass-flux approach is given in Figure 4.1.

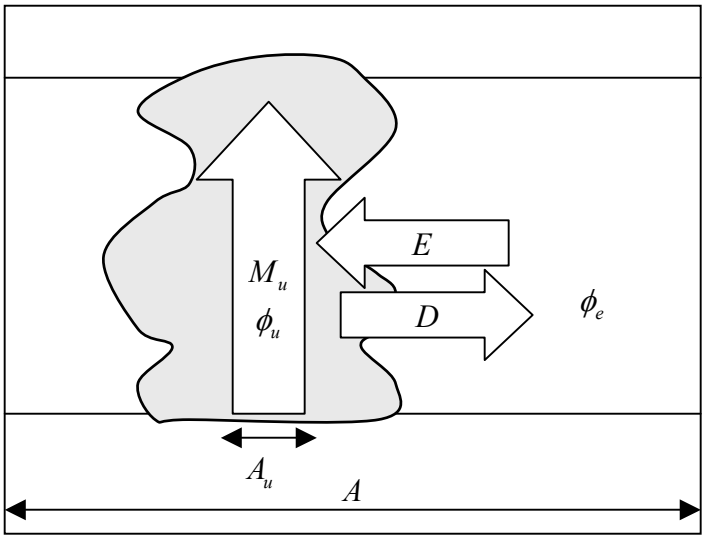

FIGURE 4.1 Schematic representation of the mass-flux approach. A narrow strong updraft in an area A_u is assumed to represent the ensemble of cumulus clouds in the total area A. The vertical transport inside the updraft is described by the mass-flux M_u and modified by lateral exchange with the environment by means of detrainment D and entrainment E.

We can now write the equations for updraft and environmental averages of ϕ as (Siebesma and Cuijpers, 1995):

$$\rho\frac{\partial a_u\phi_u}{\partial t} = -\frac{\partial M_u\phi_u}{\partial z} + E\phi_e - D\phi_c - a_u S_u \tag{4.3}$$

$$\rho\frac{\partial (1-a_u)\phi_e}{\partial t} = +\frac{\partial M_u\phi_e}{\partial z} - E\phi_e + D\phi_c - (1-a_u) S_e \tag{4.4}$$

in which the mass-flux $M_u = \rho a_u (w_u - \overline{w})$ is introduced. The sources and sinks of ϕ are denoted by S.

Analogous to this, the mass continuity equation follows as:

$$\rho\frac{\partial a_u}{\partial t} = -\frac{\partial M_u}{\partial z} + E - D \tag{4.5}$$

In order to obtain convenient equations that describe the properties of updrafts that are subject to lateral mixing, three further approximations are made:

- Turbulent transport is driven by major updrafts and weak environmental subsidence, this leads to a reduction of equation (4.2): $\rho\overline{w'\phi'} \approx \rho a_u(w_u - \overline{w})(\phi_u - \phi_e)$.
- The fractional cloud cover $a_u \ll 1$ (hence $(1-a_u) \approx 1$), which leads to $\phi_e \approx \overline{\phi}$.
- The updraft is in a steady state, i.e. $\partial X_u / \partial t = 0$.

Using these assumptions in combination with equations (4.3) and (4.4), we obtain:

$$\frac{\partial M_u \phi_u}{\partial z} = E\overline{\phi} - D\phi_u + a_u S_u \tag{4.6}$$

$$\rho\frac{\partial \overline{\phi}}{\partial t} = \frac{\partial M_u \overline{\phi}}{\partial z} - E\overline{\phi} + D\phi_u + S_e \tag{4.7}$$

$$\frac{\partial M_u}{\partial z} = E - D \tag{4.8}$$

The entrainment and detrainment rates can subsequently be parameterized as $E = \varepsilon M_u$ and $D = \delta M_u$ (Siebesma and Holtslag, 1996). In the expressions for these rates, the fractional entrainment rate ε and the fractional detrainment rate δ have been introduced. A typical in-cloud value for deep cumulus is $\varepsilon = \delta = 3\times10^{-4} m^{-1}$ (Tiedtke, 1989).

4.3 The trigger function

4.3.1 Introduction

This section presents the main aspects of the previous ECMWF trigger function, as well as the modifications made in the new trigger function as proposed by Jakob and Siebesma (2003). Neggers (2002) and Cheinet (2003) proposed a new formulation for lateral entrainment of updraft properties, which is considered in subsection 4.3.2. Only recently, Siebesma et al. (2004) have again modified some parts of the function, they are also taken into account in this section.

The original triggering of cumulus convection in the ECMWF model consists of the undiluted ascent of an air parcel from the lowest model level at 10 m. The thermodynamic properties of the air parcel are equal to the environmental properties at the corresponding level. If saturation takes place, an LCL is detected if on each level between the release level and the saturation level, it holds that $\Delta T_v = T_{vu} - \overline{T}_v > -0.5K$. This criterion can be seen as a buoyancy sorting mechanism, parcels that become more than 0.5 K negatively buoyant during their ascent in the sub-cloud layer will not make it as a cumulus cloud, and hence will be detrained. In fact, the phenomenon that parcels that are colder than their environment in some cases can penetrate to the cloud layer, is caused by the build-up of CAPE in regions that are subjected to a positively buoyant situation (see equation 2.8).

After the detection of a cloud base, the parcel rises further on the latent heat that is released due to the condensation process. This occurs under the same undiluted circumstances, and is carried out for making a first estimate of cloud top. This estimate is used for the choice between shallow (depth < 200 hPa) or deep (depth > 200 hPa) convection.

The cloud base values of temperature and specific humidity are determined from the undiluted ascent, as well as the mass-flux at cloud base M_u (section 4.2). For the latter, in the case of shallow

convection the calculations make use of the conservation of moist-adiabatic energy $h = c_p T + gz - Lq_l$ in the layer between the release height and cloud base. This energy is assumed to be conserved under adiabatic height displacements. Finally, the cloud base value for updraft vertical velocity is arbitrarily set to 1 m/s.

In the remains of this section, we will introduce the four changes that are proposed for the new ECMWF trigger function, with respect to the previous formulation.

4.3.2 Lateral mixing

In the parcel model that is associated with the new trigger function, a lateral mixing of updraft properties with the environment is assumed during the ascent. If we substitute equation (4.8) and the parameterizations for entrainment en detrainment $E = \varepsilon M_u$ and $D = \delta M_u$ (section 4.2) in (4.6), we obtain that an under adiabatic conditions conserved property $\phi = \{\theta_l, q_t\}$ of the updraft mixes with the environmental air as (Betts, 1973):

$$\frac{\partial \phi_u}{\partial z} = -\varepsilon(\phi_u - \overline{\phi}) \tag{4.9}$$

where we made use of a source term S_u that is equal to zero. The updraft property and environmental property are denoted by ϕ_u and $\overline{\phi}$ respectively.

Near the surface, mixing occurs with a fractional entrainment rate ε that is height-dependent:

$$\varepsilon = c_\varepsilon \frac{1}{z} \tag{4.10}$$

A typical value for c_ε is 0.4. In the lower ABL equation (4.10) is confirmed by LES studies of De Roode et al. (2000) and Jakob and Siebesma (2003). Higher up, ε approaches the values found also by LES results and by observations, in the order of $10^{-3} m^{-1}$ for shallow convection and $10^{-4} m^{-1}$ for deep convection.

The $1/z$ dependency is based on the idea that a lot of individual, narrow clouds can mix more effectively with the environment than a few horizontally extended clouds in the same area. It is in some kind reasonable to suggest the effectiveness of the mixing inversely proportional to the dominating turbulent length scale (Siebesma, 1998). Combining this with LES results that favour the idea of a constant aspect ratio of shallow cumulus clouds with height, an entrainment rate that is inversely proportional to z is found. This is illustrated in Figure 4.2.

Neggers (2002) and Cheinet (2003) suggested a twofold formulation for the fractional entrainment rate, that is also dependent on the ratio of the variance dissipation time (τ) and the updraft vertical velocity:

$$\varepsilon = \max\left[c_\varepsilon \frac{1}{z}, \frac{1}{\tau w_u} \right] \tag{4.11}$$

Both terms inside the max-operator represent the inverse of a certain length scale λ which is considered as the length scale on which lateral mixing in the updraft takes place and hence determines the rate of entrainment of environmental air into the air in the updraft. In addition to (4.10), this formulation assumes less entrainment in faster updrafts.

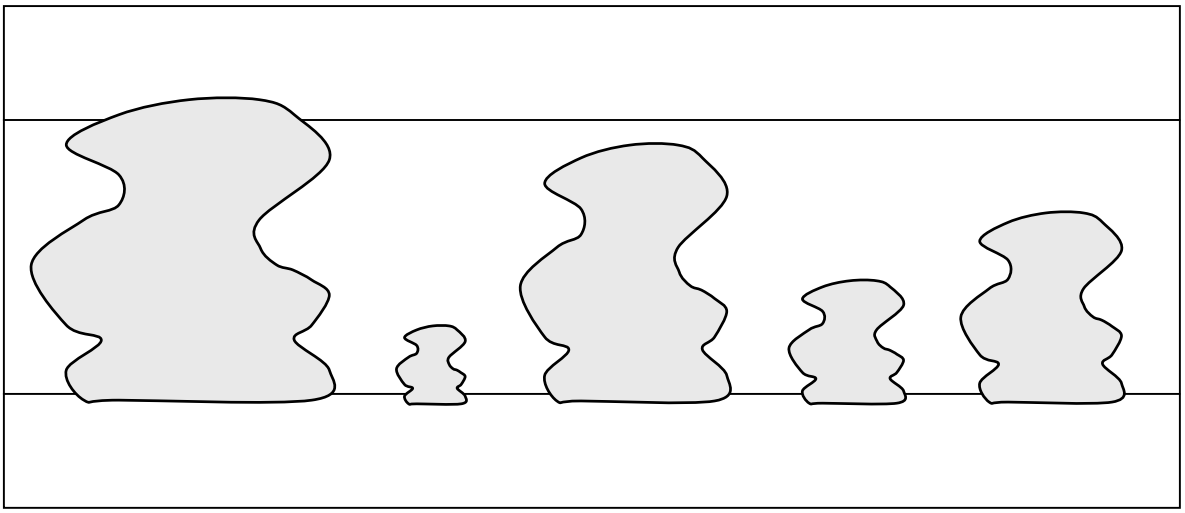

FIGURE 4.2 A cumulus field with its lower and upper cloud boundaries (horizontal lines). Typically, cloud cover decreases with height, which causes a less effective lateral mixing for the ensemble at higher levels.

The formulation presented in equation (4.11) solves the problem of a too low fractional entrainment rate in the moist boundary layer, near the cloud base and the inversion. This problem caused an overestimation of cloud thermodynamic properties and cloud top in the original formulation. On the other hand, one might expect a great sensitivity to some model parameters like parcel release height and excesses in this case, caused by the dependency on updraft vertical velocity.

4.3.3 Vertical velocity equation

By analogy with (4.9), an equation for the conservation of vertical velocity in the updraft (Simpson and Wiggert, 1969) can be obtained. Assuming that the sources S_u of w_u can be described in a turbulent pressure perturbation and a buoyancy term

$$S_u = -\frac{1}{\rho}\frac{\partial \overline{p}}{\partial z} + g\frac{(\theta_{vu} - \overline{\theta}_v)}{\overline{\theta}_v} \tag{4.12}$$

we obtain:

$$\frac{1}{2}\frac{\partial w_u{}^2}{\partial z} = -\varepsilon_w w_u{}^2 + F_p + F_B \tag{4.13}$$

with ε_w the fractional entrainment rate that holds for updraft vertical velocity. We should remark here that $\overline{p}$ represents the mean deviation from hydrostatic pressure.

Now, we can make use of the fact that the pressure perturbation term can be parameterized in terms of the vertical velocity variance, which itself can be related to the updraft vertical velocity variance with a proportionality factor γ, taken as 0.15 here. Furthermore, we assume $\varepsilon_w = b_w \varepsilon$ with $b_w = 0.5$ according to LES results from Siebesma et al. (2004). This leaves us with:

$$\frac{1}{2}(1-2\gamma)\frac{\partial {w_u}^2}{\partial z} = -b_w \varepsilon {w_u}^2 + F_B \tag{4.14}$$

which can be rewritten in the form:

$$w_u \frac{\partial w_u}{\partial z} = -c_1 \varepsilon {w_u}^2 + c_2 F_B \tag{4.15}$$

in which the constants c_1 and c_2 have values of $b_\varepsilon /(1-2\gamma) \simeq 0.71$ and $1/(1-2\gamma) \simeq 1.43$, respectively. In fact, they take into account the contribution of the pressure perturbation and buoyancy source terms that are introduced in equation (4.13).

The vertical velocity equation in (4.15) has the form that was already described by e.g. Simpson and Wiggert (1969) and Jakob and Siebesma (2003), except for the values of c_1 and c_2. The last two mentioned authors used $c_1 = 2$ and $c_2 = 1/3$, which means that there has been an enormous turn in the ranking of amount of importance that is given to the two source terms.

The decision process for triggering convection is entirely determined by (4.15). If a LCL is found and the vertical velocity of the parcel is still positive at the corresponding level, the condensation scheme is deployed and a cumulus cloud develops. Additionally, the cloud top height is defined as the level above the LCL, at which the vertical velocity becomes negative.

4.3.4 Excesses at release height

In the initialization process, offsets (i.e. positive anomalies) in potential liquid water temperature and total specific humidity are given to the parcel, before it actually starts its dry-adiabatic ascent. These anomalies in $\phi_u = \{\theta_{lu}, q_{tu}\}$ are generated as follows at a certain model level z_r:

$$\phi_u(z_r) = \overline{\phi}(z_r) + b_\phi \frac{\overline{w'\phi'}_{srf}}{\sigma_w(z_r)} \tag{4.16}$$

with an excess proportionality factor $b_\phi \simeq 1.5$ (from LES results) and $\overline{w'\phi'}_{srf}$ the surface flux of property ϕ. We try to make an estimate of the value for b_ϕ in the second part of this study (see section 5.6). Note that the value of 1.5 is much lower than the value $b_\phi = 8$, proposed originally by Troen and Mahrt (1986) and used in the ECMWF operational model (Siebesma et al., 2004).

4.3.5 Exact calculation of cloud base height

In the original trigger function, the height of the first model level where supersaturation of the parcel took place was taken as cloud base height. In the new parameterization, the pressure of this

cloud base height is exactly computed and the height of the nearest model level that corresponds with this pressure is taken as cloud base height. This method has as a great advantage that it prevents a systematic overestimation of cloud base height, which is especially very useful in models with a coarse vertical resolution.

4.4 1D Single Parcel Ascent Model

4.4.1 Introduction

The 1D Single Parcel Ascent Model (1D SPAM) that was developed during this research based on existing codes, is able to study the proposed trigger function for shallow cumulus convection in an idealized way. The used model is a so-called parcel ascent model, in which in a situation with known ABL environmental profiles and surface fluxes, an air parcel is lifted from a certain release height at prescribed times. With the prescribed assumptions for initialization excesses, lateral mixing, cloud base detection and vertical speed, one can study the evolution of the cumulus-topped boundary layer during the day and have a close look at the corresponding updraft profiles.

In this section, the experimental setup of this 1D SPAM, based on the new formulation of the trigger function in the previous section, is presented.

4.4.2 Model grid

The column in 1D SPAM originally has 400 full and 401 half levels, with an equidistant vertical grid distance of 10 metres. The choice for these full and half levels is very common, e.g. a variable that is derived from another variable at two full levels, can now be computed at the half level in between, without localization problems. Here, $z_f(1) = 5m$, $z_h(1) = 10m$, $z_f(400) = 3995m$ and $z_h(401) = 4000m$, where the subscripts f and h denote the full and half levels, respectively. The number of vertical grid levels and the grid distance can be changed very easily.

The time grid consists of intervals of 10 minutes, chosen mainly because of the data that is available on this time interval. Most of the time, input consists of only one day of data (144 time steps), so it will not take a lot computer time to run the 1D SPAM for one day, given the chosen time grid.

4.4.3 Initialization profiles

1D SPAM is fed with environmental profiles that are derived from Cabauw mast and IPT or RS90 data (see chapter 3). Heat and moisture fluxes are also in the input file, because of the dependency on surface fluxes in the offsets that are given to the parcel at the release height. Furthermore, the surface pressure is given in order to start the calculation of the profile for potential temperature. The initialization routine combines observations of atmospheric variables at different heights and interpolates them to the chosen vertical model grid.

During this procedure, the correction of the mast/IPT combined profile that was discussed in section 4.1, is also carried out.

4.4.4 Scaling parameters

In 1D SPAM, an empirical relation by Holtslag and Moeng (1991) is used to calculate the standard deviation σ_w at a height z:

$$\sigma_w(z) = 1.3 w_* \left[\left(\frac{u_*}{w_*} \right)^3 + 0.6 \left(\frac{z}{z_i} \right) \right]^{1/3} \left[1 - \frac{z}{z_i} \right]^{1/2} \tag{4.17}$$

Here, u_* and w_* are the horizontal and vertical friction velocities respectively, and z_i is the inversion height, as computed in the previous time step.

In this formulation u_* is set on a typical value of 0.1, while w_* is defined as (Stull, 1988):

$$w_* = \left(g z_i \frac{\overline{w'\theta_v'}_{srf}}{\overline{\theta_v}} \right)^{1/3} \tag{4.18}$$

The surface flux $\overline{w'\theta'}_{srf}$ is therefore calculated at the lowest model level as the eddy correlation

$$\overline{w'\theta'} = \frac{1}{N} \sum_{i=1}^{N} (w_i - \overline{w})(\theta_i - \overline{\theta}) \tag{4.19}$$

in which N is the number of data points in an averaging period. Now, the desired surface flux $\overline{w'\theta_v'}_{srf}$ – with virtual potential temperature instead of 'normal' potential temperature – is approximated by (Schotanus et al., 1983):

$$\overline{w'\theta_v'}_{srf} = \overline{w'\theta'}_{srf} + 0.61 \overline{\theta}\, \overline{w'q_t'}_{srf} \tag{4.20}$$

4.4.5 Parcel ascent

When the parcel starts its ascent, the updraft properties $\phi_u = \{\theta_{lu}, q_{tu}\}$ obtain an anomaly following equation (4.16), which can be discretized as:

$$\theta_{luh}(k_r) = \overline{\theta}_{lh}(k_r) + b_\theta \frac{\overline{w'\theta_l'}_h(1)}{\sigma_{wh}(k_r)} \tag{4.21}$$

$$q_{tuh}(k_r) = \overline{q}_{th}(k_r) + b_q \frac{\overline{w'q_t'}_h(1)}{\sigma_{wh}(k_r)} \tag{4.22}$$

with k_r the index of the release height z_r, i.e. $z_r = z_h(k_r)$.

During the ascent, the conserved property ϕ_{uh} is subject to lateral mixing with the environment as presented in (4.9). This equation reads in a discretized form as:

$$\theta_{luh}(k+1) = (1 - c_{mixh}(k))\theta_{luh}(k) + c_{mixh}(k)\overline{\theta}_{lh}(k) \tag{4.23}$$

$$q_{tuh}(k+1) = (1 - c_{mixh}(k))q_{tuh}(k) + c_{mixh}(k)\overline{q}_{th}(k) \tag{4.24}$$

with a linear mixing factor c_{mixh} formulated as

$$c_{mixh}(k) = \varepsilon_h(k) dz_f \tag{4.25}$$

in which the fractional entrainment rate $\varepsilon_h(k)$ is prescribed, in the form corresponding to the proposed parameterization (Neggers, 2002; Cheinet, 2003), see equation (4.11). This delivers:

$$\varepsilon_h(k) = \max\left[c_\varepsilon / z_h(k), 1/\tau(j) w_{uh}(k) \right] \tag{4.26}$$

The vertical grid distance between two half levels is denoted by dz_f. Furthermore, the variance dissipation time τ is computed for each time index j as $0.62\tau_*$ with the eddy turnover time $\tau_* = z_i / w_*$ (Cheinet, 2003).

The updraft vertical velocity equation, presented in (4.15), is discretized as:

$$w_{uh}^2(k+1) = w_{uh}^2(k)(1 - 2c_1 \varepsilon_h(k) dz_f) + F_{Bh}(k)(2c_2 dz_f) \tag{4.27}$$

with

$$F_{Bh}(k) = \frac{\theta_{vuh}(k) - \overline{\theta}_{vh}(k)}{\overline{\theta}_{vh}(k)} \tag{4.28}$$

the buoyancy force per unit of mass, analogous to (2.4). Besides, it is assumed that $w_{uh}^2(k_r) = \sigma_w^2(k_r)$. In 1D SPAM, the cloud top is chosen as the inversion height, that is approximated as the height at which the vertical velocity vanishes, i.e. $w_{uh}^2 = 0$. The corresponding height is computed with:

$$z_i = z_h(k_i - 1) + \frac{w_{uh}^2(k_i - 1)}{w_{uh}^2(k_i - 1) - w_{uh}^2(k_i)} \tag{4.29}$$

where k_i denotes the level where w_{uh}^2 is negative for the first time. Analogous, the LZB is determined in the same way, except that it is assumed to be the first level above the LCL where buoyancy becomes zero. An exact level calculation like that in equation (4.29) can also be performed for z_{LNB}, z_{LCL}, z_{LFC} and z_{LZB}. Nevertheless, this operation is not necessary in the model described here, because of the small vertical grid distance of 10 metres.

We use the condensation scheme of Sommeria and Deardorff (1977), presented in section 2.5, for deriving the properties of the in-cloud phase change of water vapor to liquid water. First, with equations 2.10-2.16, the saturation specific humidity q_s is computed, after which this value is compared with the in situ updraft total specific humidity q_{tu}, to determine the amount of liquid water that is formed on the corresponding level:

$$q_{luh}(k) = \max\left[q_{tuh}(k) - q_{sh}(k), 0 \right] \tag{4.30}$$

which means that $q_{luh}(k)$ obtains the value of the difference $q_{tuh}(k) - q_{sh}(k)$, provided that this difference is positive.

The lowest level at which liquid water is present is defined as the LCL. For an exact calculation, one could use an expression like that of the inversion height, formulated in (4.29). As mentioned before, there is no need for the exact calculation of cloud base height (subsection 4.3.5).

By means of the diagnostic relation

$$\theta_{vuh}(k) = \left(\theta_{luh}(k) + \frac{L}{c_p} q_{luh}(k) \Pi_h(k) \right) (1 + 0.61 q_{tuh}(k) - 1.61 q_{luh}(k)) \tag{4.31}$$

the updraft virtual potential temperature is computed on each level and used as input for the vertical velocity equation that is presented in (4.27). For model levels below the LCL, this relation reduces to $\theta_{vuh}(k) = \theta_{luh}(k)(1 + 0.61 q_{tuh}(k))$, that is valid for unsaturated air.

In Figure 4.3, a schematic overview of the functioning of 1D SPAM is presented.

4.5 Thermal structure identification

4.5.1 Introduction

An important new aspect in the proposed trigger function is the formulation of excesses that are given to the parcel at the release height, as described in subsection 4.3.4. Equation (4.16) tells us that the anomaly $\phi_u - \overline{\phi}$ is assumed to be linear proportional to the ratio of the surface flux of property ϕ and the standard deviation of the vertical velocity, σ_w, at the prescribed release height.

Next, we are interested in the question how well the excesses for θ_l and q_t, which are obtained by means of this assumption, are corresponding to the observational values observed for typical shallow convective situations. Therefore, an identification method was set up that is able to pick thermals out of time series in the case of given thermal selection criteria.

4.5.2 What is a thermal?

Using the thermal identification method that is discussed in this section, we will try to make an estimate of the excess proportionality factor b_ϕ. The sensitivity to different parameters in the criterion for sampling is investigated. Next to this, we would like to gain insight in the mean thermal anomalies as a function of height, as well as the contribution of thermals in the total turbulent fluxes of heat and moisture on the respective mast level.

As mentioned in subsection 2.2.3, various criteria exist in selecting thermal structures. In general, one should agree that a thermal should be warmer and contain more moist with respect to its environment and as well have an upward vertical velocity. Possible definitions include treshold values for anomalies of temperature, vertical velocity, humidity or turbulence intensity (Lenschow and Stephens, 1980). All of these thresholds have their own advantages and disadvantages. We here discriminate between three elements of the criterion used in this study:

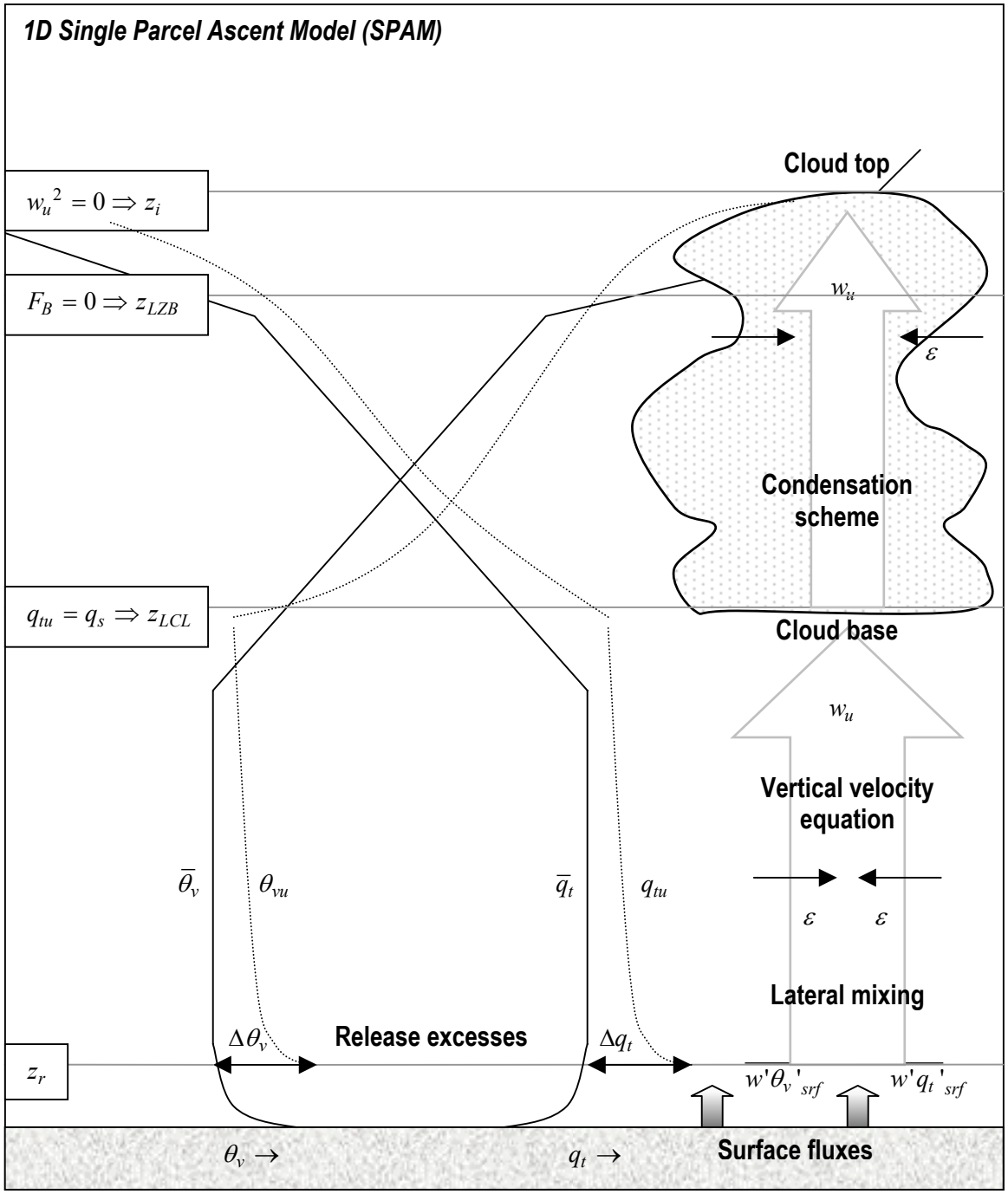

FIGURE 4.3 Schematic picture of the 1D Single Parcel Ascent Model, in a cumulus-topped ABL. A developing cumulus cloud is evaluated from its origin at the surface to its cloud top. Note that the original release excess in θ_l is here converted to an excess in θ_v.

- **Averaging period**, τ_c. This is the interval on which the average value and standard deviation of the thermal variables in the time series are calculated.

Choosing τ_c too short, the mean that is calculated is strongly dependent on accidental extreme events in the respective period. Furthermore, good statistics might not be possible because only few (or incomplete) thermal structures are selected. In the case that τ_c is chosen too long, thermals that occur in periods of e.g. lower temperatures because of the diurnal cycle are not selected because the mean is too high to obtain positive anomalies. A typical value of τ_c in our study is 30 minutes.

- **Thermal structure time scale**, T_c. This is the minimum time scale on which the prescribed thermal criteria have to persist.

This is the criterion element we want to determine from wavelet analysis (section 2.6). In fact, we are interested in thermals that exist as spatial coherent structures on a typical length scale L_c. By making use of the Taylor hypothesis (e.g. Stull, 1988) this is related to the time scale T_c through the relation $L_c = U \cdot T_c$, where U denotes the ambient mean horizontal wind speed during the averaging period. A classical picture lets us assume that L_c is dependent on height, because thermal structures get more and more extended horizontally during the ascent due to the merging of eddies with height. This should imply that L_c is small near the surface and grows to approximately cumulus horizontal size at cloud base. Expected values for T_c at the lowest level of the Cabauw mast (5 m) are in the range 5 – 50 s.

- **Treshold quantity.** Sampling can occur with respect to different measured quantities (T, q and w) or combinations of them.

Furthermore, a treshold fraction α_{wc} is introduced. This factor determines the fraction of the standard deviation of the sampling quantity that has to be exceeded to be identified as thermal data point. For example, if we set $\alpha_{wc} = 0$, all the points with positive anomalies with respect to their average value $\overline{w}$ in the corresponding averaging period, are selected.

Thermals will be selected if on an averaging period τ_c the anomaly X' of a given quantity X exceeds the treshold factor α_{Xc} times the standard deviation σ_X during a period of at least T_c.

4.5.3 Wavelet transforms

The theory of wavelet transforms is discussed in section 2.6. In order to find time scales of coherent thermal structures for the input for the identification method as described in the previous subsection, the wavelet technique is applied here.

As mother wavelet function, we have chosen the DOG2 or Mexican Hat wavelet. The characteristics of this wavelet are quite useful in identifying coherent thermal structures. This type of continuous wavelet functions is able to unfold the signal continuously in both time and frequency space, in spite of discrete functions like e.g. the Haar wavelet function (Chen and Hu, 2002). Furthermore, the shape of the Mexican Hat resembles the shape of an eddy very well, which is also

important to optimize the analysis results. Another example of a wavelet that has this typical shape is the Morlet wavelet. Nevertheless, it is shown that the Mexican Hat wavelet is the most convenient type of wavelet function for performing turbulence spectral dynamics studies, because it is more localized in frequency. This feature makes this type – better than e.g. the Haar, Ramp or DOG1 wavelet function – suitable for studying characteristics of time scale or frequency (Collineau and Brunet, 1993).

We analyzed the convective period on several (BBC2 and non-BBC2) days, by splitting up the convective period in intervals with $\tau_c = 30\,\text{min}$ and downsampling the time series of T, q and w from 10 Hz to 1 Hz. Subsequently, we calculated anomalies in these time series with respect to a 100 s running average, which leaves us with structures that can have a dominant period between 1 and 100 s. This implies values between a few metres and a few hundred metres for the corresponding detected length scales, assuming a typical value for the mean horizontal windspeed ff of 3 m/s.

The smallest resolvable scale s_0 is chosen 1.0 s. The downsampled signal has a frequency of 1 Hz, so the smallest resolvable scale contains only 1 data point in the time series. Subsequently, the greatest resolvable scale is $2^J s_0$ with $J = 8$, which corresponds to a maximum period of 256 s. The thermal structure length scale T_c, which is discussed in subsection 4.5.2, is identified as the time scale that shows the first maximum in energy variance, considering the global wavelet spectrum. Results of the method discussed here are presented in section 5.6.

5 Results

5.1 Introduction

In this chapter, the results of the discussed models and methods from the previous chapter are presented and evaluated with observations gathered during the BBC2 campaign. These give a good indication of the atmospheric conditions under which the specific case studies are performed and the general results are derived.

After a discussion about the so-called 'Golden Days' of the BBC2 campaign, the setup of a reference run is presented and tested on two of the selected days. Next, a validation of the results takes place with help of observations done by instruments mounted on the Merlin aircraft. Furthermore, this chapter discusses sensitivity studies that are carried out in order to investigate the offline model sensitivity to some essential parameters. The second part of this study, concerning surface layer thermal characteristics, is presented in the last section of this chapter.

5.2 BBC2 Golden Days

In every measurement campaign there are days that are deemed to be 'Golden Days', because of the favourable circumstances under which the processes you are interested in, develop. Considering this study, we should look at days that are characterized by small advective tendencies of temperature and humidity in the boundary layer and the occurrence of single layer boundary layer clouds, i.e. shallow cumulus. The occurrence of rain during the day should be omitted and the measurements used for initialization of the offline model and for validation of the results, should have a high temporal resolution. Above all, the biases in these measurements should not be too large.

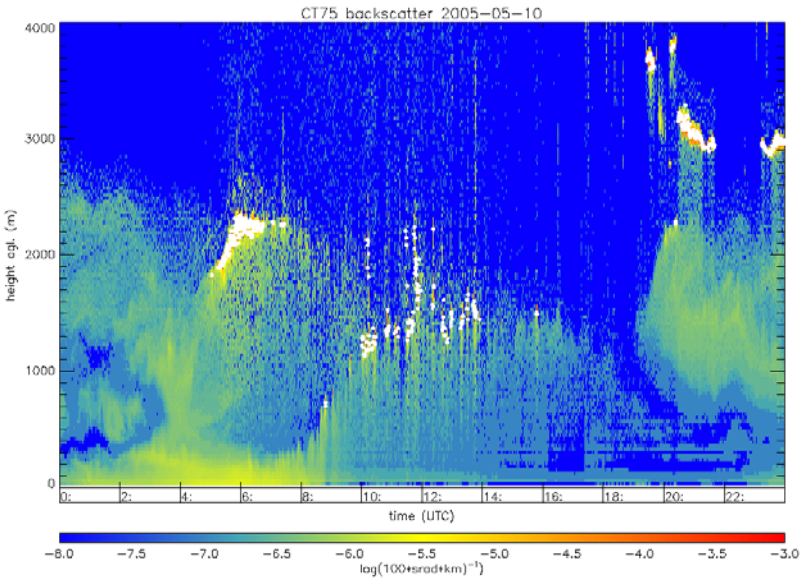

a)

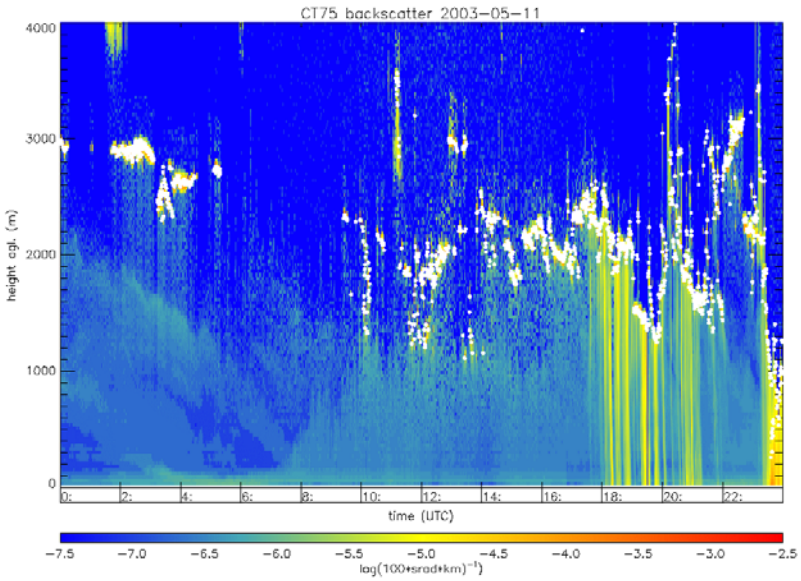

b)

FIGURE 5.1 CT75K lidar backscatter ($\log(100 \cdot srad \cdot km)^{-1}$) for the BBC2 Golden Days a) 10 May and b) 11 May. White dots represent detected cloud bases. Higher values depict stronger echoes, which illustrate the presence of cloudy air. The backscatter observed between the surface and the low clouds is induced by aerosols. Note the build-up of a dry convective boundary layer starting at sunset and the period with rain on the 11th between 18 and 22 UTC.

For the BBC2 campaign, the modeling community of the participating institutes and universities has selected four days that somehow obey one or more of these favourable circumstances: 10, 11, 15 and 21 May 2003. Considering the CT75K lidar images of these days (Figures 5.1 and 5.2), we can immediately distinguish between two types of boundary layer cloud structures. During daytime, 10 and 15 May show the development of one layer of (shallow cumulus) clouds, while 11 and 21 May also have a overlying stratocumulus deck with a cloud base at a height of approximately 2 kilometres. Furthermore we notice the build-up of the dry convective boundary layer that starts at sunset (approximately 06:30) and causes a parabolic-like shape in height of the echo signal, which is associated with the diurnal cycle. This is especially well seen for 10 May.

Date	IPT temporal density (T,q)
10 May	H1 62% M1 39% **H2 79%** M2 45%
11 May	H1 37% M1 34% **H2 59%** M2 57%
15 May	H1 52% M1 49% **H2 62%** M2 63%
21 May	H1 27% M1 37% **H2 53%** M2 55%

TABLE 5.1 Data density of the Integrated Profiling Technique (IPT), for H1 (v1 with HATPRO radiometer), M1 (v1 with MICCY radiometer), H2 (v2.0 with HATPRO radiometer) and M2 (v2.0 with MICCY radiometer).

In Table 5.1 the temporal data density for the different versions of derived IPT profiles of temperature and humidity is listed. It contains the first and second version of the IPT based on the HATPRO (Humidity And Temperature Profiler) and MICCY (Microwave Radiometer for Cloud Cartography) radiometers. It should be stressed that this table does not give any information about the temporal distribution of profiles. One can imagine that big data gaps during the convective

period are fatal for a study like this one, because the linear interpolation that is performed in time and height, generates great biases in the initialization profiles of temperature and humidity. These cause on their turn unrealistic cloud boundaries and updraft profiles of e.g. buoyancy (and hence vertical velocity) and liquid water content. For best density reasons, we hereafter use IPT v2.0 with HATPRO radiometer.

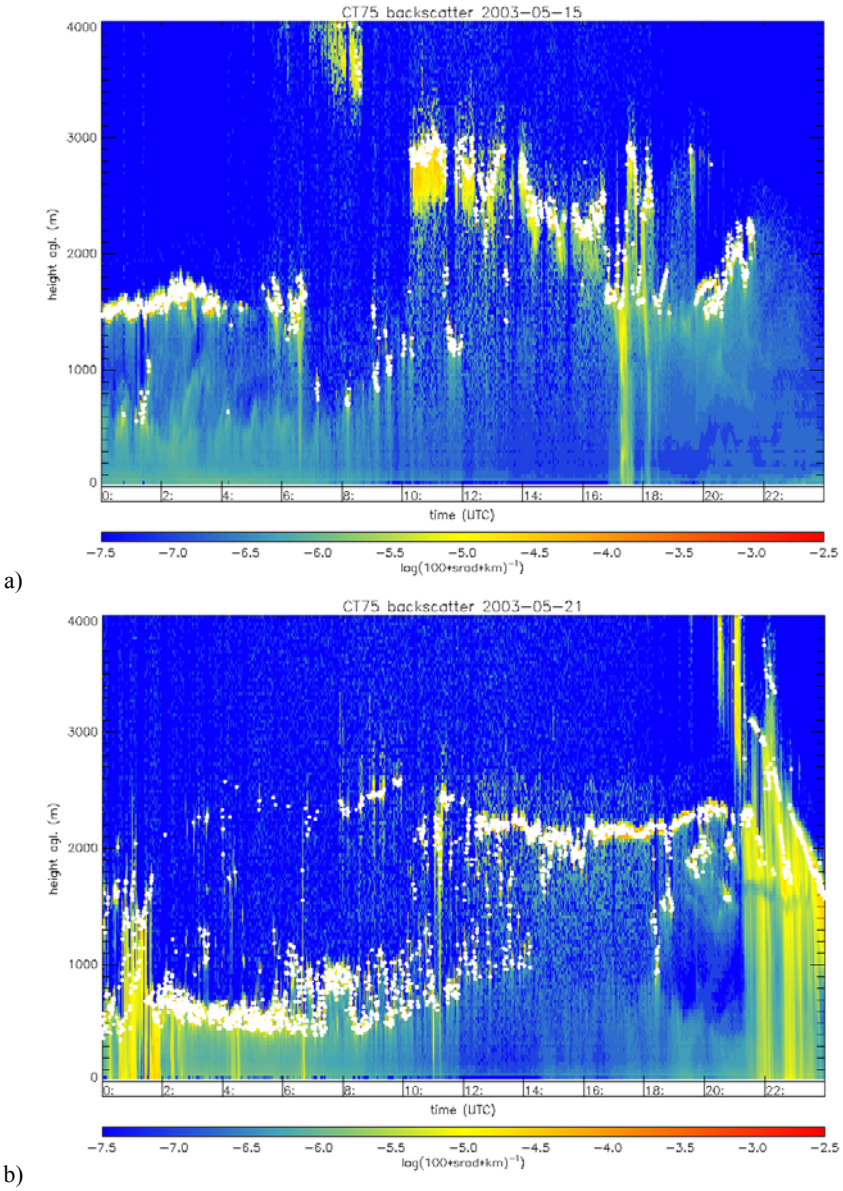

FIGURE 5.2 Same as Figure 5.1, but for a) 15 May and b) 21 May.

Unfortunately, the differences in temperature and humidity between the IPT and mast profiles at the fitting height of 200 metres are considerably large for the morning and early afternoon of 15 May. These discrepancies can be seen in Figure 5.3. In spite of the very nice shallow cumulus fields, probably the best during BBC2, we decided for this reason to skip this day in the 1D SPAM analysis. Nevertheless, the high-frequent time series of temperature, humidity and vertical velocity

as measured by the sonic anemometers in the mast, are used in the study on thermal characteristics that is discussed in section 5.6.

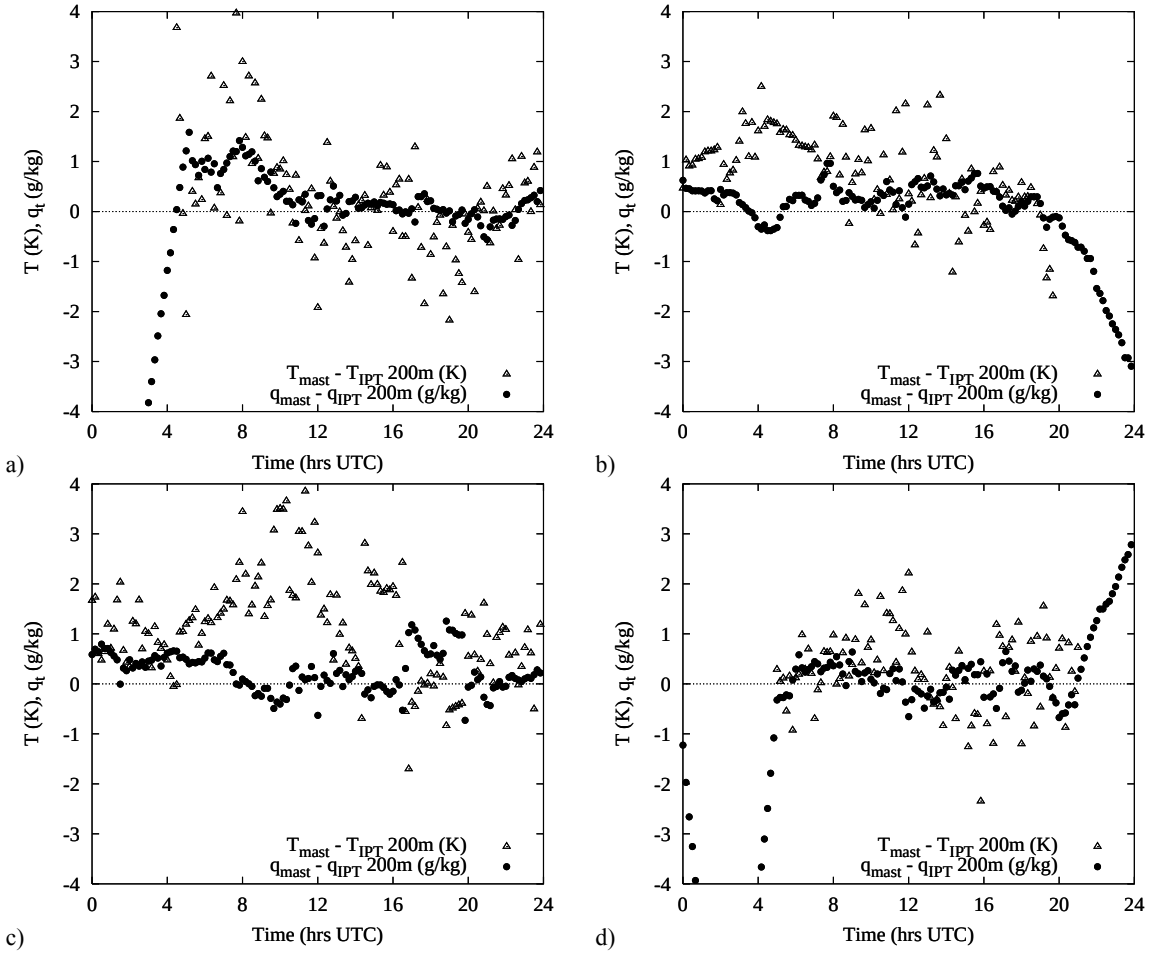

FIGURE 5.3 Differences between Cabauw mast and IPT at 200 m for temperature (triangles) and humidity (dots), for a) 10 May, b) 11 May, c) 15 May and d) 21 May.

Logically, a small part of the difference at 200 m can be explained by the fact that the IPT has a rather coarse resolution of 250 m. Hence, its first level is positioned at a height of 250 m. The upper level of the mast is located at 200 m, which causes the difference to be non-zero. However, to avoid possible sudden drops and discontinuities in the initialization profiles, we translated the IPT profiles of T and q towards the value of the upper level of the Cabauw mast to obtain the combined mast/IPT profile that is given to the 1D SPAM model. This correction procedure is demonstrated in Figure 5.4. We linearly smoothed away the difference found at this fitting level to a height of 2000 m, which means that the correction term is getting smaller and smaller between 200 m and 2000 m. Above this height, the combined mast/IPT profile obtains its IPT value again, according to aircraft measurements that show that the IPT generates fairly good profiles for higher levels (see e.g. Merlin measurements in Figure 5.4).

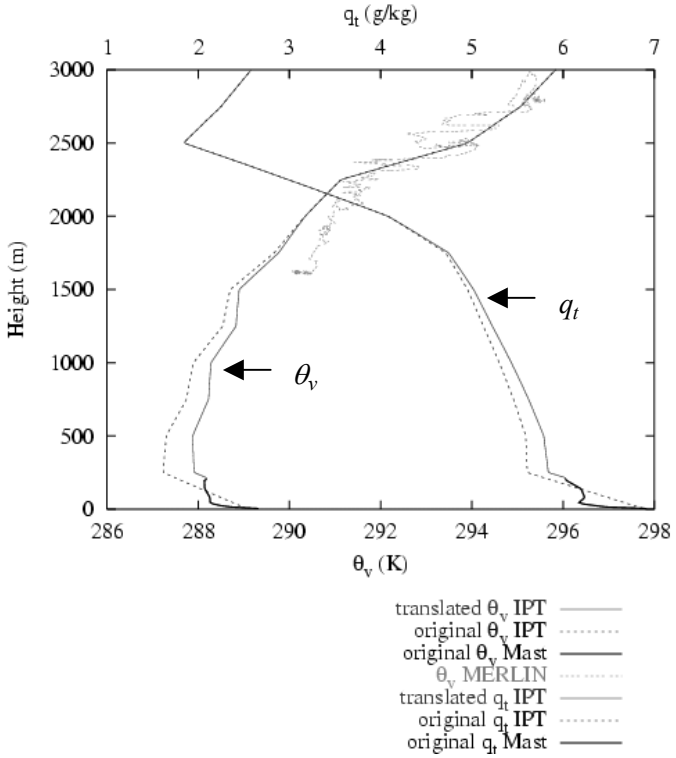

FIGURE 5.4 Example of the correction procedure for the combined mast/IPT initialization profiles, for 11 May 11:00 UTC. Profiles shown for virtual potential temperature (surface value 289.2 K) and total specific humidity (surface value 6.9 g/kg). The original IPT profiles (dotted) are translated with the difference between the IPT and the mast (solid black) at 200 m, whereafter this correction term linearly decreases to zero between 200 and 2000 m. The results are the translated IPT profiles (solid grey), which are combined with the fixed mast profiles in order to obtain the desired initialization profiles. Between 1600 and 3000 m the Merlin measurements (four dots) are depicted. Note the good resemblance of these measurements with the IPT profile in the inversion layer and for higher levels.

5.3 Case studies

5.3.1 Introduction

For the analysis of mutually comparable model results, a 1D SPAM reference run with the following specifications was set up:

- lateral entrainment: $\varepsilon = \max[c_\varepsilon(1/z), 1/(\tau w_u)]$
- entrainment factor: $c_\varepsilon = 0.4$
- parcel release height: $z_r = 10m$, i.e. $k_r = 2$
- release excesses: $\phi_u(z_r) = \overline{\phi}(z_r) + b_\phi\left(\overline{w'\phi'}_{srf} / \sigma_w(z_r)\right)$; $b_\phi = 1.0$
- vertical velocity: $w_u\left(\partial w_u / \partial z\right) = -c_1 \varepsilon {w_u}^2 + c_2 F_B$
  with $c_1 = 0.71$, $c_2 = 1.43$ (sub-cloud)
  with $c_1 = 2$, $c_2 = 1/3$ (in-cloud)

This reference run is hereafter called REF. The parameters were chosen such that cumulus clouds were simulated as good as possible at a glance, with respect to the observed cumulus cloud bases and tops on the Golden Days 10, 11 and 21 May 2003. In this tuning especially the choice for c_ε is

very important. The factors c_1 and c_2 in the vertical velocity equation were chosen according to recent LES results for the dry and moist convective boundary layer (Cheinet, 2003).

Total simulation time is one day, i.e. 86400 s, with an interval of 600 s between two successive ascents. Hence, every 10 minutes initialization profiles and values for surface fluxes and surface pressure are given to the routine, which calculates the direct response of interesting updraft thermodynamic quantities to these constraints. The vertical resolution is set on 10 m, applied to a total vertical domain of 4000 m. Furthermore, an undiluted simulation, that is equivalent to REF with the modifications $c_\varepsilon = 0$ and $b_\phi = 0$, will be denoted by UND.

5.3.2 Case study: 10 May 2003

The first BBC2 day on which we focus is Saturday 10 May 2003. The HIRLAM analysis for 00, 06, 12, 18 UTC on this day can be found in Figure 5.5. We can see that the Benelux is subjected to a dominating westerly to southwesterly flow that is fed by an almost stationary low pressure area south of Iceland. Relatively cold air has taken possession of The Netherlands, brought in by a cold front on 9 May. A combination of the analyses of 00 and 06 UTC shows the passing of a weak trough, behind which a modest ridge with high pressure is building up. Furthermore, a developing low pressure system can be found southwest of the United Kingdom, which may cause the passing over of a weak front on the 11th with a chance of multi-layer clouds and precipitation in the evening.

Saturday 10 May 2003 - De Bilt, The Netherlands (06260)

Temperature		**Precipitation**	
Average	11.4 °C	Amount	0.0 mm
Maximum / Minimum	17.6 °C / 4.2 °C	Duration	0.0 hrs
Sunshine and cloudiness		**Winds**	
Sunshine duration	11.5 hrs (75 %)	Average wind speed	2.1 m/s
Average cloud cover	3/8	Max. hourly wind speed	4.0 m/s
	(Partly cloudy)	Max. wind gust	7.0 m/s
Min. visibility	3.8 km	Average wind direction	272° (W)
Relative humidity		**Pressure**	
Average	73 %	Average	1020.1 hPa

TABLE 5.2 Weather overview for De Bilt on 10 May 2003. Source: Climatological Service, KNMI, De Bilt, The Netherlands.

The cloud forecast, taken from the special KNMI meteo briefing that was made for every campaign day, reads as follows:

```
(Written by Rob van Dorland, date: 2003-05-10 07:56 UTC)
The day started with some high clouds at 6000 to 7000 ft, associated with the
passing trough. Today, convection is expected when the temperature rises above
the 14 to 15 degrees. This will be the case between 9 and 10 UTC. The CCL is
situated at about 2000 ft at the coast to 3000 ft inland. The cloud tops in the
early afternoon are at 6000 to 7000 ft. Above this level we have a critical
unstable profile, implying the possibility of showers later in the afternoon and
```

if they occur mainly in the east of The Netherlands. Cloud cover will be around 4 to 5 octa, perhaps somewhat more in the east.

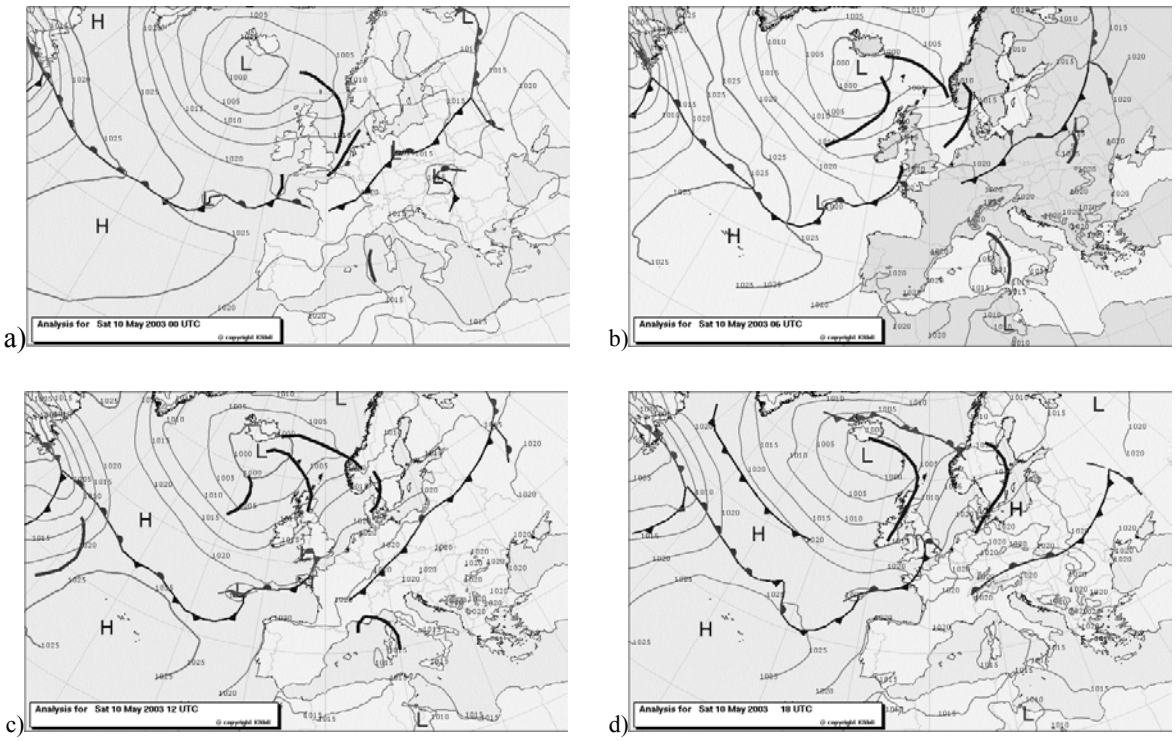

FIGURE 5.5 HIRLAM analysis for 10 May a) 00 UTC, b) 06 UTC, c) 12 UTC and d) 18 UTC surface pressure.

Model initialization

Figure 5.6 shows the input profiles for liquid water potential temperature $\overline{\theta}_l$ and total specific humidity $\overline{q}_t$ every two hours, between 06 and 18 UTC. We immediately note the large tendencies of temperature – and to some extent, humidity – in the boundary layer, that is characterized by the large differences that can be seen closer to the surface. The stable profile that is shown in the profile of $\overline{\theta}_l$ at 06 UTC completely disappears during the morning and an unstable situation in the surface layer can be distinguished in the other profiles for 10 May. Only in the 18 UTC profile the stable regime returns. In the profiles of total specific humidity, we observe a drying of the first 700 – 800 metres of the boundary layer from about 0.0065 g/g at 06 UTC to 0.005 g/g at noon. In spite of this, above the boundary layer a moistening can be seen, which is caused by presence of a cloud layer in this height interval during daytime.

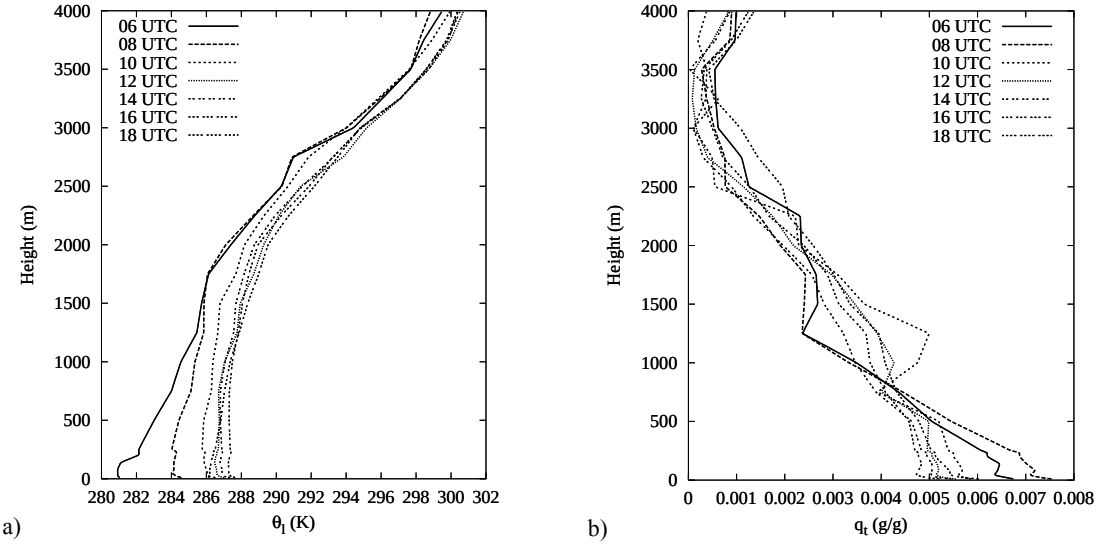

FIGURE 5.6 Two-hourly input profiles for a) liquid water potential temperature and b) total specific humidity, on 10 May 2003.

In Figure 5.7 the reader can find the time series of $\overline{\theta_l}$ and $\overline{q_t}$ at 20 m and at 200 m and the surface fluxes of heat (sensible heat flux, SHF) and moisture (latent heat flux, LHF) and surface pressure p_{srf}. The nighttime difference between the 20 m and 200 m levels is considerably large (for both variables), but after sunrise (05:30) the positive surface fluxes tend to smooth this difference and develop a well-mixed layer. From 09 UTC, we observe an unstable situation in the surface layer, which is characterized by a value for the 20 m liquid water potential temperature that exceeds the 200 m value. This goes on until about 16 UTC, whereafter both temperatures diverge and the stable situation sets in. After sunset the difference of 2 K between 20 m and 200 m temperatures that was observed in the early morning, is reached again.

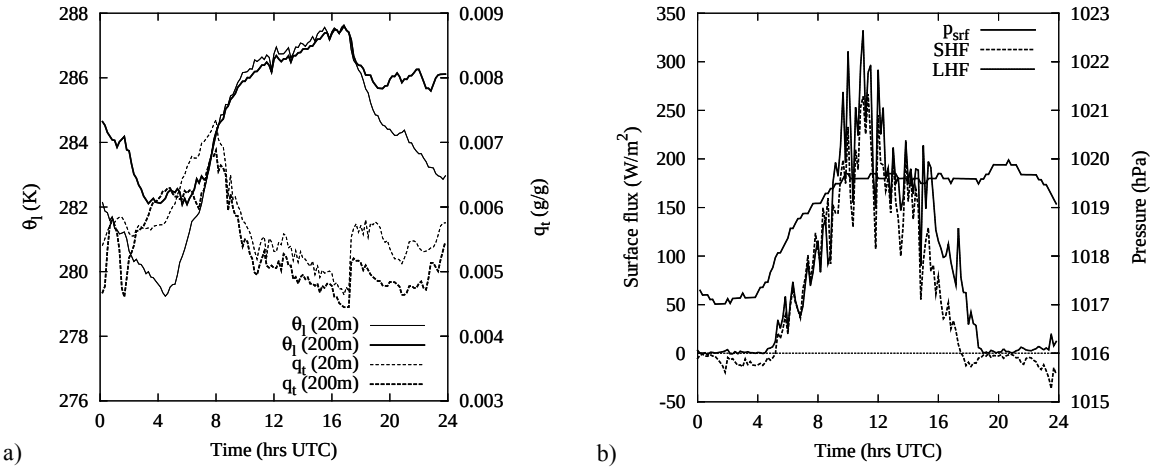

FIGURE 5.7 Time series of a) liquid water potential temperature and total specific humidity at 20 and 200 metres and b) surface sensible heat flux (SHF), surface latent heat flux (LHF) and surface pressure, on 10 May.

SHF and LHF reach surface values up to $320 Wm^{-2}$ around 12 UTC and follow each other closely. The surface pressure shows a positive tendency from 04 UTC until 09 UTC. This is related to the ridge of high pressure, that builds up after the passing of the trough between 00 and 06 UTC, as

discussed earlier in the text about the HIRLAM analysis. The remainder of this day, p_{srf} is fairly constant.

Updraft properties

Now the synoptic setting of this case study and its essential initialization profiles are known, we consider the updraft properties that are calculated for this day, making use of the REF run of 1D SPAM (description in subsection 5.3.1). A typical result for the cloud boundaries that are simulated is shown in Figure 5.8. The observations of the CT75K lidar ceilometer are also plotted in this figure, which makes a comparison of cloud base heights possible. It should be remarked here that the 'envelope CT75K cloud base' is introduced here to make a best guess of the actual cloud base instead of considering all the observed points available. The enormous spread in observed cloud base is caused by the fact that the lidar is able to measure only directly above the instrument, which e.g. causes higher values of observed cloud base when looking into the periphery or inlet of a cloud.

Since the cloud bases observed around 06 UTC are associated with the passing trough, we will primarily focus on the convective period between 08 UTC and 16 UTC. We observe a gradually developing convective boundary layer as already illustrated by the lidar image in section 5.2; the dry inversion height rises from sunset at approximately 05:30 UTC. Shallow cumulus only forms on top if enough CAPE is available to penetrate through the inversion layer. In that case, a cloud base (black dot) is found and the condensation scheme generates in-cloud profiles of thermodynamic quantities, whereafter the cloud top is the height where the vertical velocity becomes zero.

The overall plot of REF results shows reasonable agreement with the observations. We note that the cloud base height is in some cases overestimated up to a maximum of 200 metres with respect to the envelope and that cumulus is also simulated at initialization times that it is not observed (before 09 UTC, after 16 UTC). A sensitivity test later in this chapter will reveal whether this error is systematic or not.

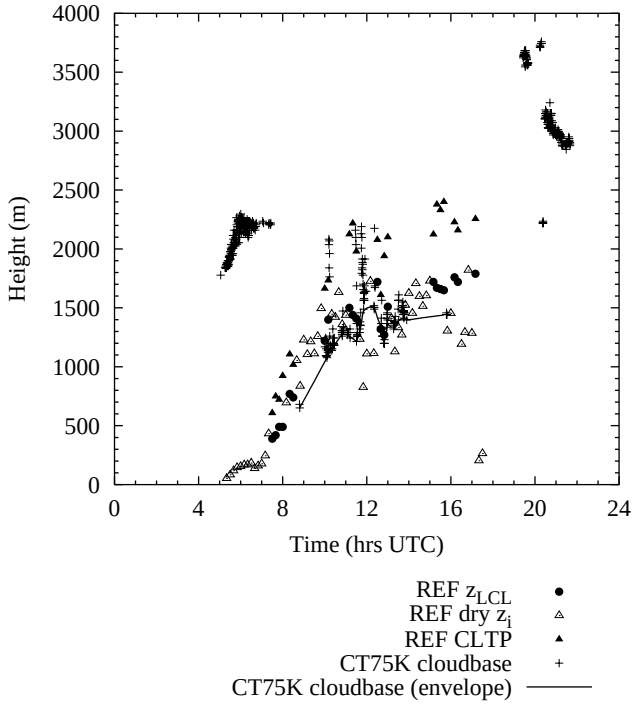

FIGURE 5.8 Cabauw cloud boundary plot for 10 May. Results for: REF modeled cloud base (black dots), dry inversion height (open triangles), cloud top (solid triangles) and CT75K observed cloud base ('+' sign and solid line).

Simulated clouds are only several hundreds of metres thick. Unfortunately, direct cloud top measurements are not available and therefore a comparison is difficult to make. From the Cloudnet[2] database, we qualitatively estimated cloud top height during the day from a radar-lidar combined retrieval for Cabauw, to gain some insight in the quality of the results of the simulated clouds in 1D SPAM. For 10 May, the cloud top height that was observed (not shown) shows good agreement with the envelope of simulated cloud tops during the REF run. It obtains value starting at 900 m for the first convective clouds at 08:30 UTC and the maximum cloud top height is around 2300 m at 12 UTC. A graph with liquid water contours for 10 May is shown in Figure 5.9.

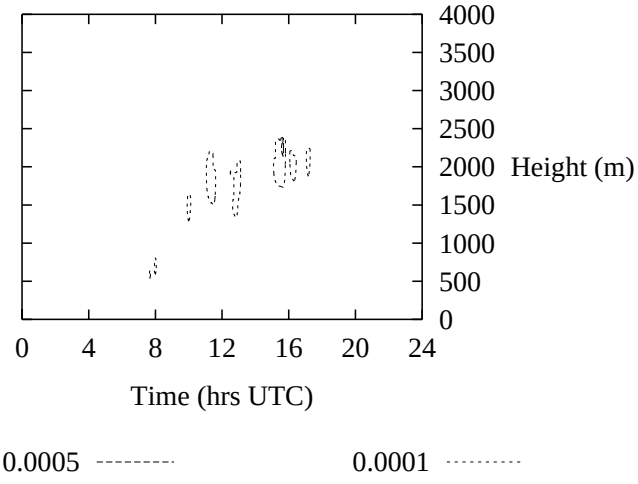

FIGURE 5.9 Contourplot for modeled updraft liquid water content on 10 May 2003. Contours have the unit g/g.

[2] Cloudnet is a European project in which retrieval of cloud microphysical properties with remote sensing instruments plays a major role. For more information visit www.met.rdg.ac.uk/radar/cloudnet

Two-hourly vertical profiles of updraft values of virtual potential temperature excess, vertical velocity, total specific humidity excess and liquid water content are shown in Figure 5.10. Starting at a value of approximately 0.5 K in $\Delta\theta_v$ at 10 m, the parcel mixes with colder environmental air during its ascent and hence the excess will decrease. For this case, all the parcels presented become negatively buoyant near the top of the dry boundary layer, but the 10, 12 and 16 UTC ascents reach their saturation specific humidity such that a cumulus cloud is formed. This is expressed in the liquid water content that becomes positive at the corresponding height, but it can also be recognized in the increasing $\Delta\theta_v$ due to latent heat release that is inextricably bound up with the condensation process. After a maximum in this excess of a few tenths of a Kelvin, lateral mixing has a great impact and destroys the buoyancy source $\Delta\theta_v$ until the cloud top is reached.

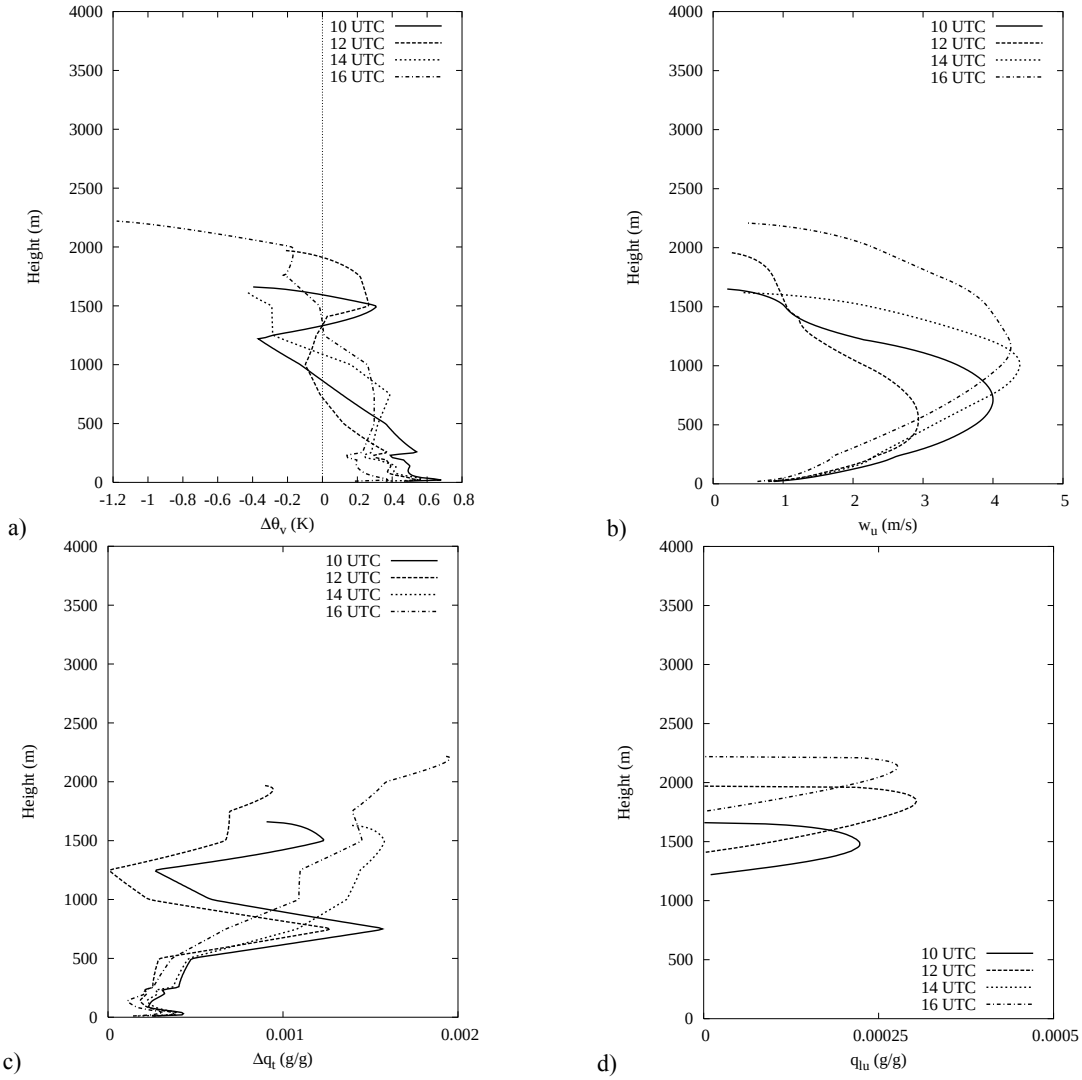

FIGURE 5.10 REF results for 10 May 2003, for a) updraft virtual potential temperature excess, b) updraft vertical velocity, c) updraft total specific humidity excess and d) updraft liquid water content.

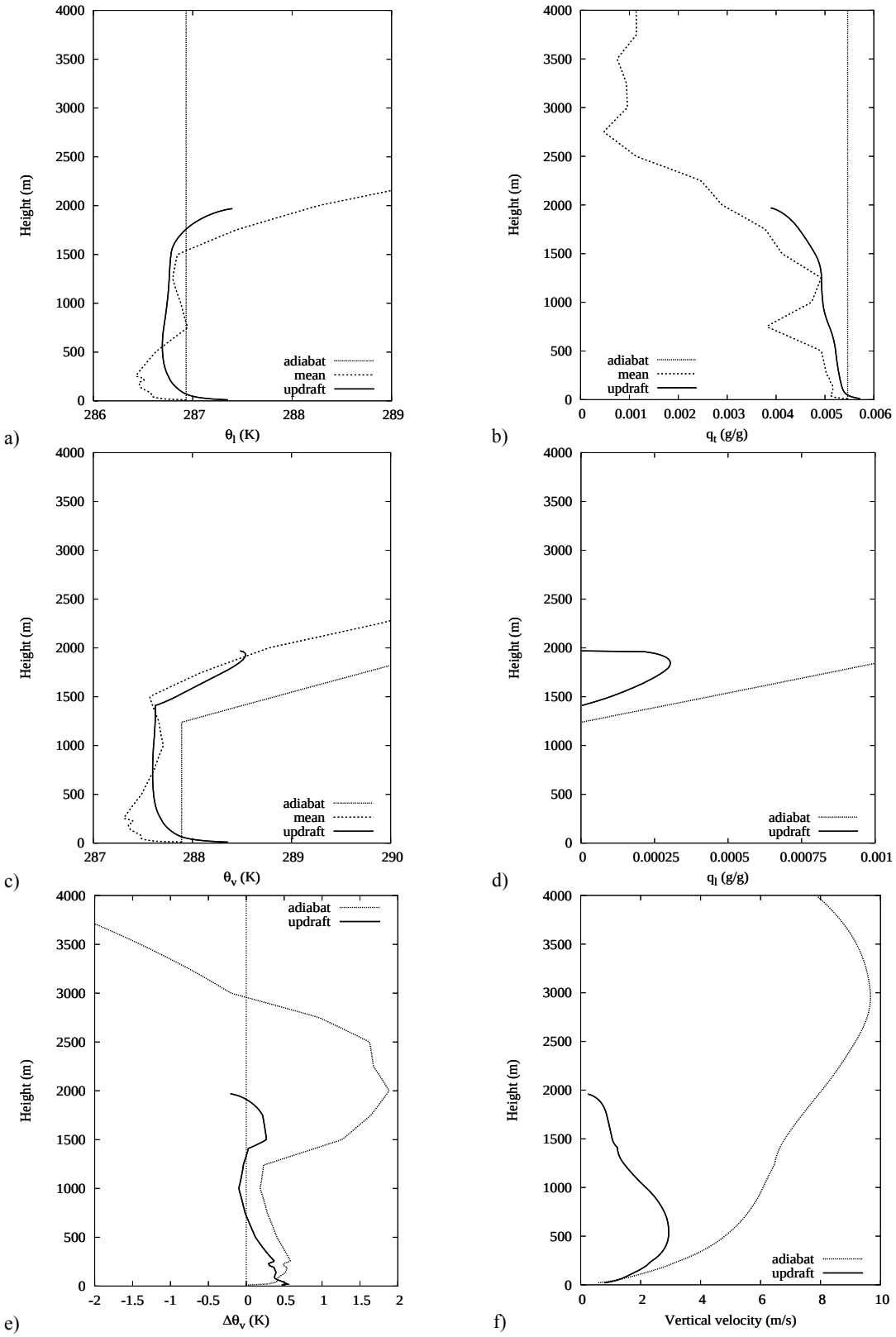

FIGURE 5.11 REF results for 10 May 2003 12 UTC, for a) liquid water potential temperature, b) total specific humidity, c) virtual potential temperature, d) liquid water content, e) virtual potential temperature excess and f) vertical velocity. In the figures, the adiabat is depicted, as well as the updraft and mean profiles (for a), b) and c) only).

The vertical velocity shows an expected quadratic profile in the convective boundary layer with maximum values for w_u of about 3 to 4 m/s. At the top, the profiles associated with cloud profiles (10, 12, 16 UTC) show slower decreasing values of w_u which is accordance with the positively buoyant circumstances they are in, as earlier mentioned considering the vertical profile of $\Delta\theta_v$. Also note that, in spite of the lateral mixing process, the total specific humidity excess gradually rises, which implies that the mean values show a decreasing vertical profile. This is confirmed by Figure 5.6.

The six panels in Figure 5.11 show updraft and mean properties for the 12 UTC response. If possible, an adiabatic value is presented. The latter is obtained as the updraft profile that is calculated for an UND run, which implies that nor release excesses nor lateral mixing are taken into account. We first note the relatively large amount of lateral mixing that occurs above cloud base (1410 m), which is a direct consequence of the implementation of a entrainment formulation that is dependent on the updraft vertical velocity. This can be observed in the profiles for the conserved quantities $\phi = \{\theta_l, q_t\}$. The liquid water content profile shows very good agreement with Rodts (2001) who found that the ratio of q_l and the adiabatic value of q_l should be in the range 0.3 – 0.4 for shallow cumulus. Especially in the higher part of our 12 UTC cloud profile this is the case. Of course, the consideration of more events and the use of aircraft observations for validation should give more value to this statement.

5.3.3 Case study: 11 May 2003

Sunday 11 May is – as already mentioned – different with respect to the previous case study. The HIRLAM analyses for 00, 06, 12 and 18 UTC are given in Figure 5.12. South of Iceland, the slowly evolving low pressure system is still present. The weak front that was discussed in the 10 May case study moves very slowly and is over the North Sea for the greatest part of the day. This causes an almost persistent deck of stratocumulus during daytime, between 2000 and 3000 m. In the evening, the front passes over and causes some rainfall in The Netherlands. The winds are mostly from south to southwest, veering to east after the overpass of the front.

Sunday 11 May 2003 - De Bilt, The Netherlands (06260)

Temperature		**Precipitation**	
Average	13.8 °C	Amount	1.0 mm
Max. / Min.	19.6 °C / 6.4 °C	Duration	1.2 hrs
Sunshine and cloudiness		**Winds**	
Sunshine duration	7.5 hrs (49 %)	Average wind speed	2.5 m/s
Average cloud cover	6/8	Max. hourly wind speed	5.0 m/s
	(Cloudy)	Max. wind gust	9.0 m/s
Min. visibility	7.0 km	Average wind direction	216° (SW)
Relative humidity		**Pressure**	
Average	74 %	Average	1018.9 hPa

TABLE 5.3 Weather overview for De Bilt on 11 May 2003. Source: Climatological Service, KNMI, De Bilt, The Netherlands.

For the expected cloud layers, we again have a look at the meteo briefing that was generated for this day:

```
(Written by Rob van Dorland, date: 2003-05-11 08:37 UTC)
According to the temp (De Bilt, 00 UTC and Hirlam, 12 UTC) cumuli may occur from
9 to 10 UTC onwards with cloud base at 2000 to 3000 ft. Due to the much drier air
than yesterday cloud cover will be less 2-3 octa, but less near the coast. Cloud
tops are estimated at 6000 ft in the early afternoon. Behind the cold front cloud
tops may grow to 18000 ft later in the afternoon. Then cloud cover may also
increase to 4-6 octa. Large cirrus fields are moving into the south of The
Netherlands. At 12 to 13 UTC the edge will be situated over De Bilt.
```

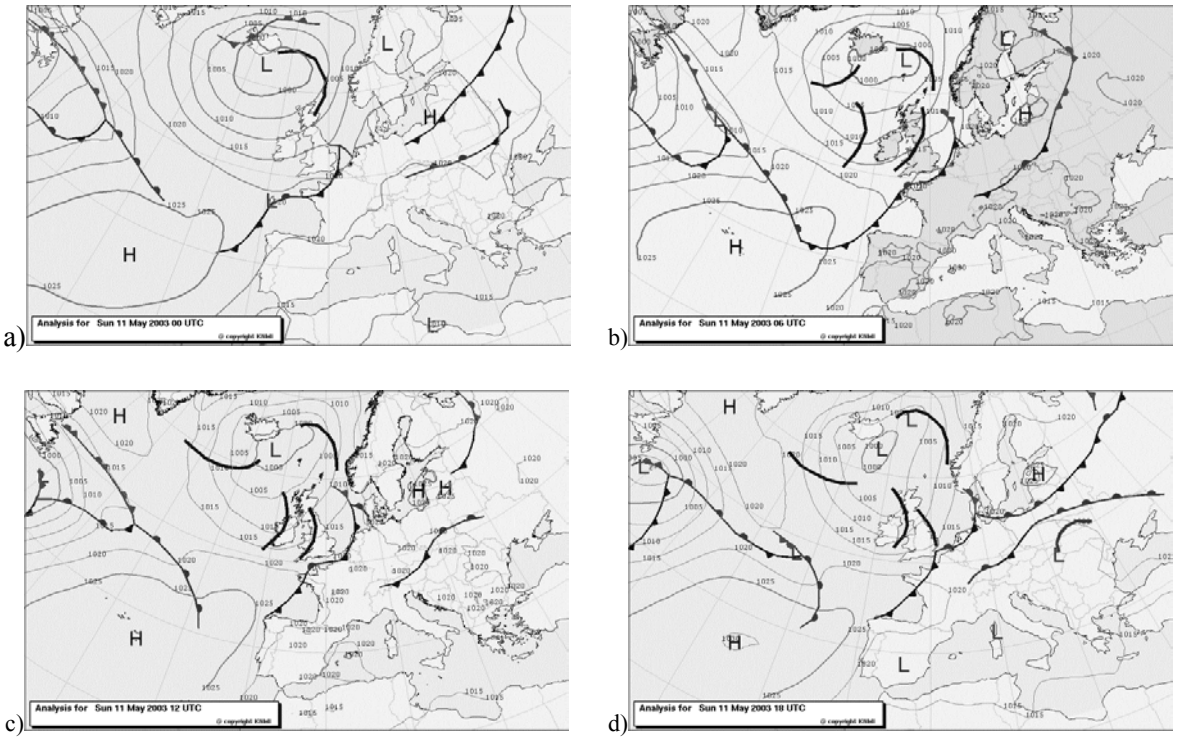

FIGURE 5.12 HIRLAM analysis for 11 May a) 00 UTC, b) 06 UTC, c) 12 UTC and d) 18 UTC surface pressure. The Icelandic Low is slowly traveling to the Benelux, which causes the surface pressure to drop as the reader can see in Figure 5.16. At 18 UTC, the cold front is above The Netherlands and generates the observed rainfall in the evening.

Besides of the multiple layer clouds that are expected, the synoptic situation on this day was considerably favourable and generated several events with shallow cumulus clouds. We have illustrated this behaviour in Figures 5.13 and 5.14 . In 5.13, the (RIVM) lidar backscatterplot for the lowest 4 km of the atmosphere is presented. Just from 10 UTC, convection starts and cumuli are formed, but there are some considerable cloud-free periods in between. We can make a distinction between three periods of cumulus clouds, with each time subsequent periods in which no shallow convection is observed. Six snapshots from the Cabauw video stream are depicted in Figure 5.14. In a), c) and e), the three distinct cumulus events that were just discussed can be seen, while in b), d) and f) a snapshot of the subsequent cumulus-free period is presented. The cumulus events are characterized by nice cauliflower clouds, the cumulus-free periods only show higher cloud decks consisting of stratocumulus and altocumulus.

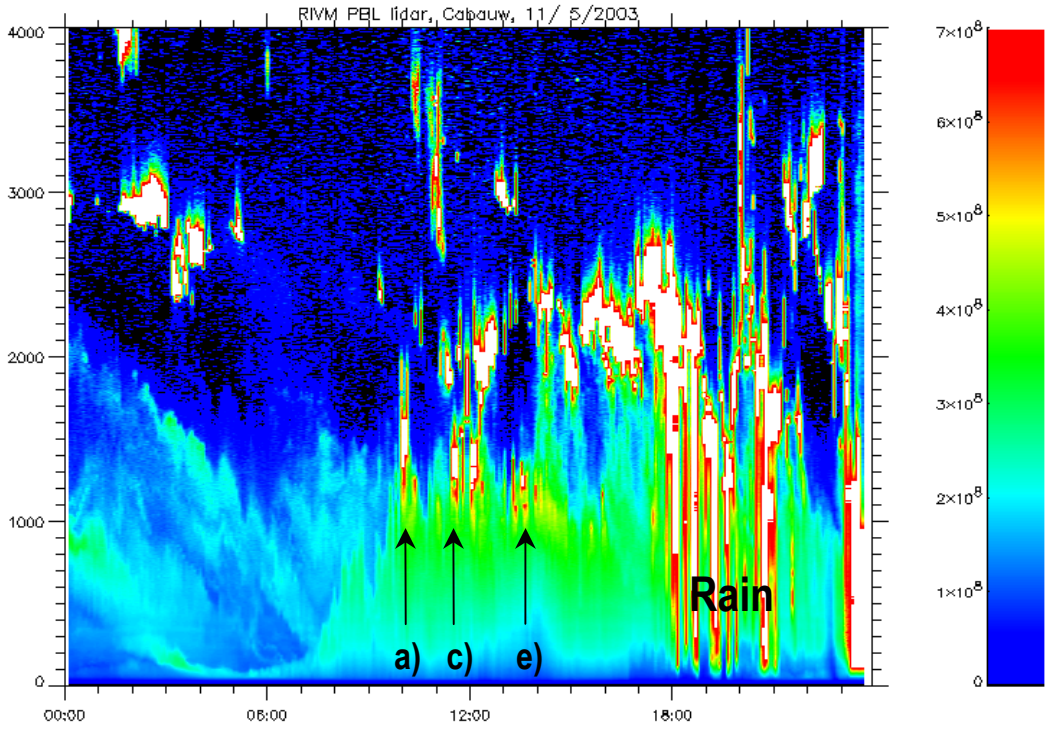

FIGURE 5.13 RIVM lidar backscatter (arbitrary units) in time and height for 11 May 2003. Higher values denote stronger echoes and are a footprint for cloudy air. Note the three shallow cumulus periods, which are indicated with arrows accompanied by the characters of the corresponding snapshots in Figure 5.14.

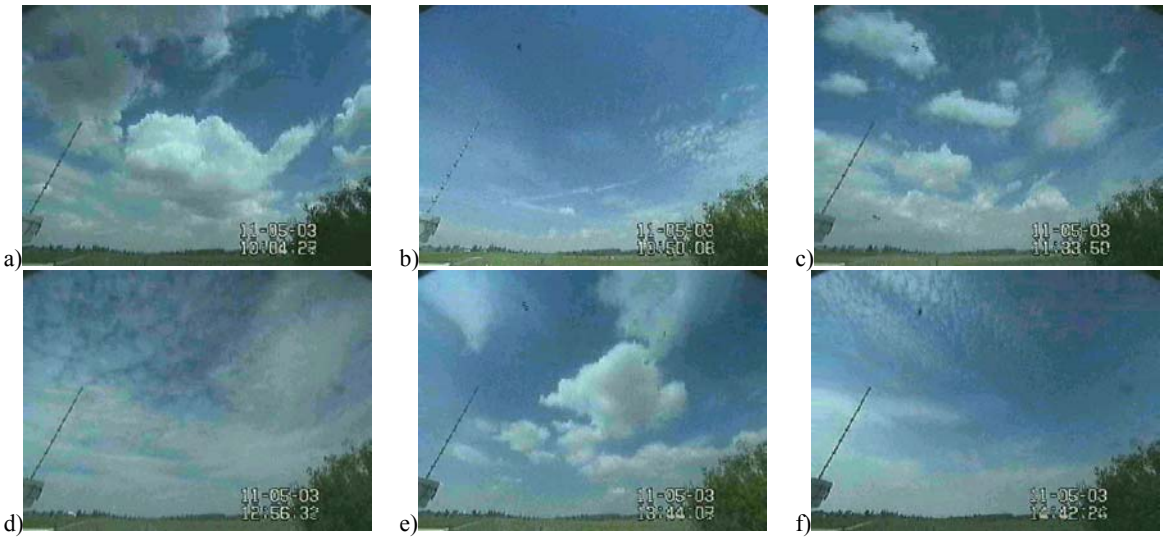

FIGURE 5.14 Snapshots from the Cabauw video stream on 11 May a) 10:04, b) 10:50, c) 11:33, d) 12:56, e) 13:44 and f) 14:42. a), c) and e) depict shallow cumulus convection events, while b), d) and f) depict the subsequent 'shallow cumulus'-free period for each event. See the lidar observations in Figure 5.13 for backscatter contourplots.

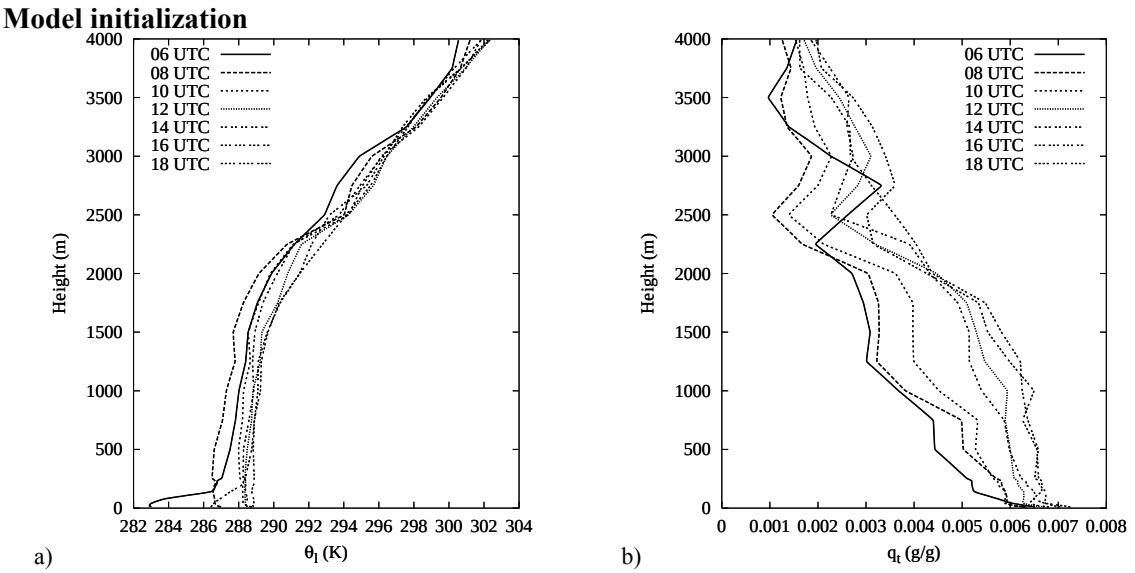

FIGURE 5.15 Two-hourly input profiles for a) liquid water potential temperature and b) total specific humidity, on 11 May 2003.

The input profiles of liquid water potential temperature and total specific humidity for 11 May 2003 are shown in Figure 5.15. The unstable surface layer develops during the morning, while in the late afternoon a slight stabilization can be seen. The profile for $\overline{\theta_l}$ at 16 UTC already shows a cooling in the lowest hundred metres, whereas in the 18 UTC profile the stable situation is more clearly present. The profiles of total specific humidity show a 0.002 to 0.003 g/g moistening of the 4 km deep column, while the surface layer value for $\overline{q_t}$ is in the order of 0.006 to 0.007 g/g during the day. With respect to the 10th, the large difference is mainly caused by a significant moistening of the boundary layer during the day. In addition to this, the contribution of the second layer of clouds to the mean profile of q_t is substantial, which we recognize in the increasing values above 2000 m.

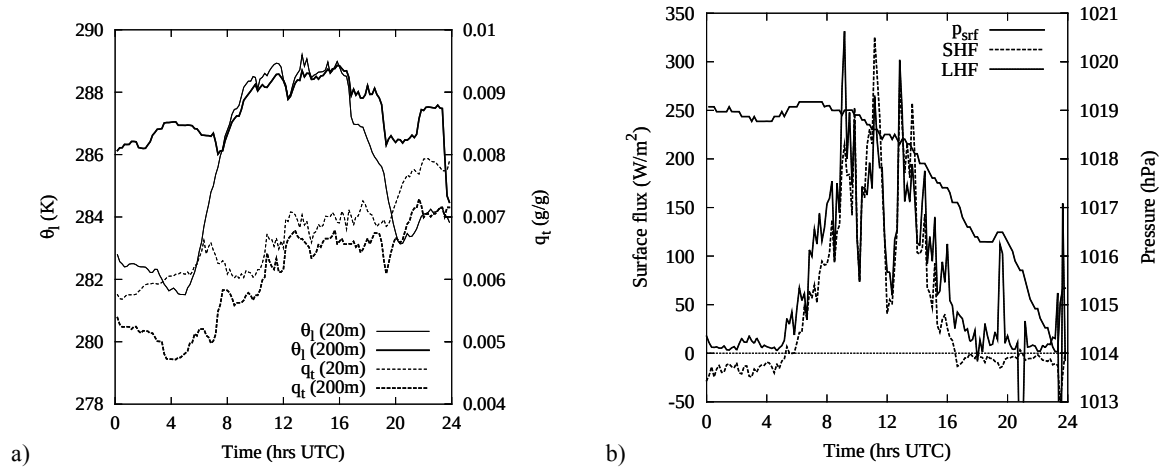

FIGURE 5.16 Time series of a) liquid water potential temperature and total specific humidity at 20 and 200 metres and b) sensible heat flux (SHF), latent heat flux (LHF) and surface pressure, on 11 May.

In Figure 5.16, the time series of $\overline{\theta_l}$ and $\overline{q_t}$ at 20 and 200 metres and the surface heat (SHF) and moisture (LHF) fluxes and surface pressure are presented. In these figures, the development of an

unstable surface layer is nicely illustrated. During the night, we see large differences between the 20 and 200 metres values for both $\overline{\theta_l}$ and $\overline{q_t}$ and near-zero values for the surface fluxes. After sunset (somewhat after 05 UTC), the fluxes increase very rapidly and tend to warm and moisten the surface layer, which can be seen in the time series in the left panel. The SHF and LHF reach again peak values of $320 Wm^{-2}$ during the day, respectively. From 08 UTC the convective warming process is complete, i.e. $\overline{\theta_l}$ obtains a higher value at 20 metres than at 200 metres. This causes an unstable situation in the surface layer and hence the possibility for near surface air to rise and form shallow cumulus clouds.

This situation is present until 17 UTC, where a frontal system passes over The Netherlands from the southwest and causes some rainfall between 18 and 19 UTC and also later in the evening. This causes some sudden changes in the order of 1K in $\overline{\theta_l}$, and $\overline{q_t}$ not to drop in the evening because of the presence of a considerable amount of moisture, as seen in Figure 5.16a. The uniformly decreasing time series of the surface pressure on 11 May also shows the incoming front.

Updraft properties

The 1D SPAM REF run for this case study generated the cloud boundary plot that is presented in Figure 5.17. The more messy character on this day can be seen in the CT75K observations that are plotted, with a lot of clouds that are associated with the incoming front, while at three distinct times (around 10, 12 and 13:30 UTC) shallow cumulus clouds form under the stratocumulus deck.

The simulated cloud base heights in REF show good agreement with the envelope of the observations of the lidar, while also the time of occurrence of convection agrees fairly well. There is some cloud-free time simulated between the periods that cumulus clouds occur, which supports the observed evolution in time that was discussed by making use of Figures 5.13 and 5.14.

In this figure (5.17), the ABL height that was derived from RASS and windprofiler measurements, is also depicted. It shows a maximum during the observed (and modeled) cloud bases at the three distinct events and is characterized by a dip in the in-between cloud-free periods. Furthermore, we note that during some of these periods, the dry inversion height more or less agrees with this derived ABL height.

The cloud tops that were again obtained from the Cloudnet radar-lidar retrieval (not shown) teach us that cloud tops simulated by 1D SPAM REF are overestimated a few hundred metres. Looking at the three ShCu periods, we obtain cloud top height values of approximately 2100, 1700 and 1600 m, respectively. The model overshoots the simulated clouds throughout the observed second layer that starts around 2000 m. This possibly occurs due the contribution of the second layer of clouds in the thermodynamic properties of the mean profile, which on its turn can have a significant impact on the dilution of the updraft. The overshoot of the clouds is also explained by the inversion that is a few hundreds of metres higher than on 10 May, and is now located between 2200 and 2500 m during the day. This gives an air parcel the opportunity to penetrate to higher levels.

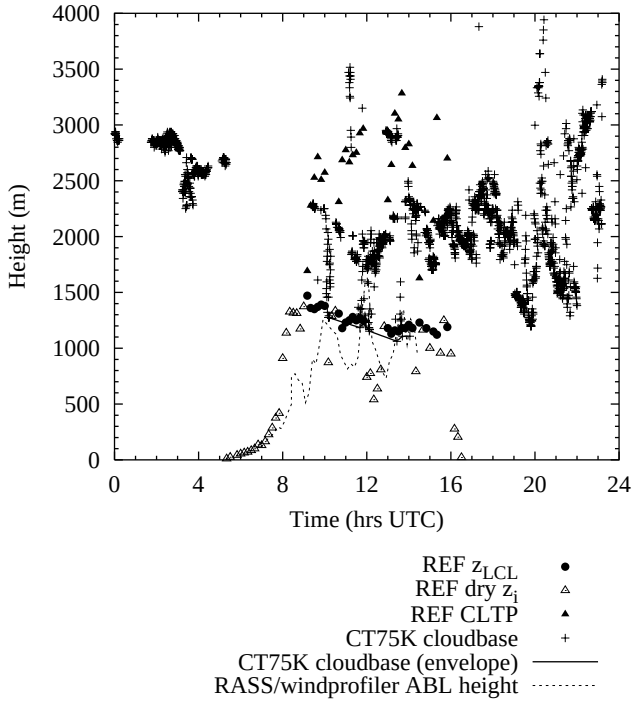

FIGURE 5.17 Cabauw cloud boundary plot for 11 May. Results for: REF modeled cloud base (black dots), dry inversion height (open triangles), cloud top (solid triangles), CT75K observed cloud base ('+' sign and solid line) and the ABL height determined with help of RASS/windprofiler observations (dashed line).

The cloud liquid water contours, which are depicted in Figure 5.18, in fact show us the presence of clouds and the in-cloud distribution of q_l during the day. At a glance, it is a very nice figure for making an estimate of cloud base, top and in-cloud liquid water profiles, but also the occurrence of convection. We note that for this day the modeled maximum value for q_l exceeds 0.002 g/g, which is around the maximum value assumed for shallow cumulus without precipitation. For 10 May, the maximum values are a factor 4 smaller. These high values for the 11th most of the time occur higher in the clouds and hence might be caused by the overestimated cloud top.

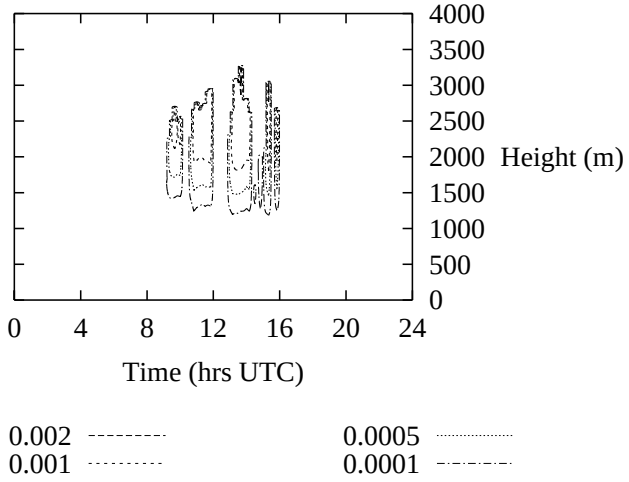

FIGURE 5.18 Contourplot for modeled updraft liquid water content on 11 May 2003. Contours have the unit g/g.

The vertical profiles for four updraft properties at 10, 12, 14 and 16 UTC are shown in Figure 5.19. We immediately note that the profiles still exists at heights between 2500 and 3000 m, which is in agreement with the earlier mentioned overshoot. We note a striking difference with the tempered profiles of updraft properties found for 10 May. The 11 May profiles are characterized by a higher CAPE that is built up by a considerable amount of in-cloud virtual potential temperature excess (5.19a). This causes the cumuli to rise higher than in the 10 May case, with more enhanced properties in the cloud layer. For example, $\Delta\theta_v$ reaches peak values of 1.5 K, while liquid water content varies between 0.0011 g/g and 0.0018 g/g for the considered cases. A significant lower entrainment rate ε for 11 May is the cause of this behaviour.

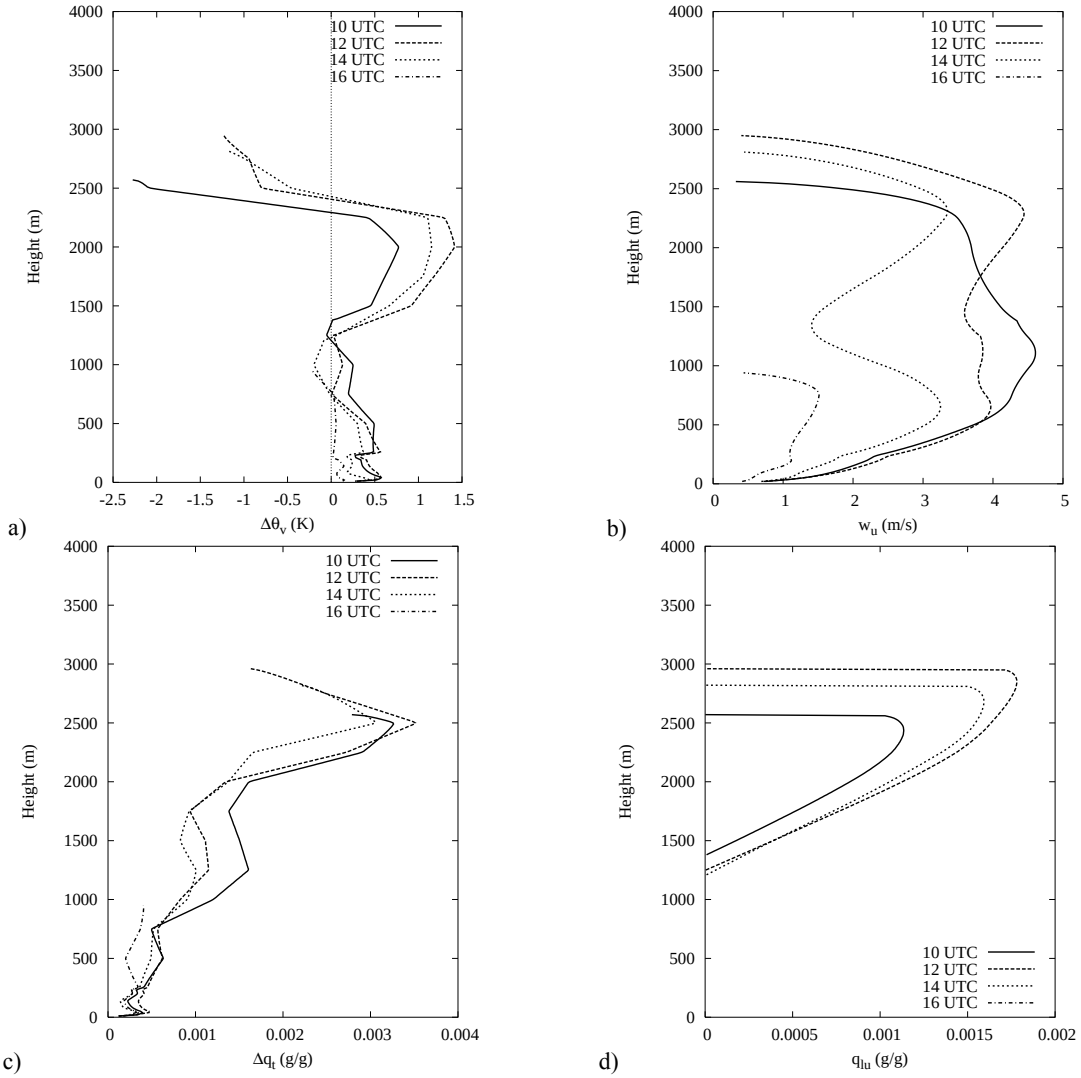

FIGURE 5.19 REF results for 11 May 2003, for a) updraft virtual potential temperature excess, b) updraft vertical velocity, c) updraft total specific humidity excess and d) updraft liquid water content.

Another remarkability that we note is the shape of the profiles for w_u for this case, especially for the 14 UTC response. We observe a shape that looks like the mirrored Greek letter ε. This is also the basis of choosing a fractional entrainment rate that depends on the updraft vertical velocity. The absolute differences in w_u may be somewhat large, but we note a local minimum for the generally

negatively buoyant height interval around cloud base height, whereafter the latent heat release motor takes care of the further rise and builds up vertical velocity. The negative buoyancy due to the presence of an inversion causes the vertical velocity to drop again, until cloud top is reached. The large differences between in-cloud and mean total specific humidity that occur in the inversion layer cause an enormous evaporative cooling which causes the cumulus clouds to dissolve. This is illustrated in Figure 5.19c, that shows the total specific humidity excess of the updraft.

For 12 UTC, we again made a comparison between the REF updraft properties and the mean and (if available) adiabatic properties, which is presented in Figure 5.20. First, we again note the lateral mixing that is nicely illustrated in the profiles of liquid water potential temperature and total specific humidity. The larger gradients towards the cloud top indicate the high entrainment rate that occurs due to the dependency on updraft vertical velocity, in combination with the high excesses $\phi_u - \overline{\phi}$ that cause the product $\varepsilon(\phi_u - \overline{\phi})$ in the dilution equation (4.9) to be large. The mean profile contributes for a substantial part in this product, note e.g. the minimum in the mean value for q_t at approximately 2500 m.

The typical shape of the vertical velocity profile that we observed in the two-hourly vertical profiles in Figure 5.19, is to some extent also visible in this figure. From cloud base (1250 m) the virtual potential temperature of the updraft rises, which causes $\Delta\theta_v$ to generate buoyancy and a subsequent increase of w_u. The buoyancy reversal around 2400 m coincides with the starting point for decreasing vertical velocity, until the cloud top is reached (2950 m). At that point, the vertical velocity becomes zero.

For the liquid water profile we notify that the ratio $q_l / q_{l,adiabat}$ is much higher (0.6 – 0.7) than for 10 May, where we observed a value of 0.3 – 0.4 (Rodts, 2001). This is strongly related to the prescribed fractional entrainment rate ε. Although the used formulation is the same in both cases, the mean profile has a considerable impact on the dilution (equation 4.9). We may conclude here that ε is lower in the largest part of the considered vertical domain for 11 May than it is for 10 May. This is confirmed in one of the sensitivity studies, discussed in subsection 5.5.5. In the next section, the airborne validation study that is carried out for 10, 11 and 21 May might give us more insight in the correctness of the modeled vertical profiles.

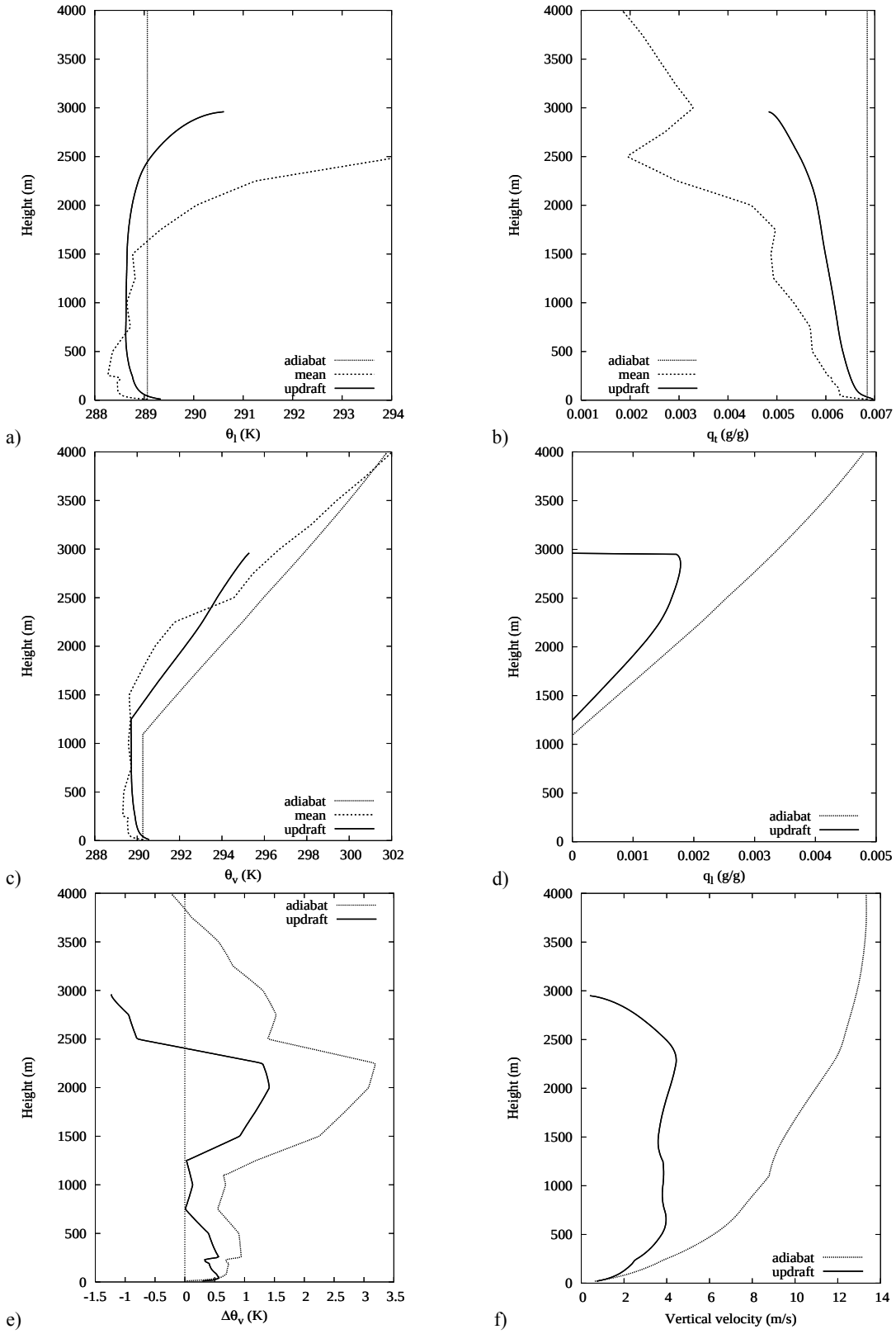

FIGURE 5.20 REF results for 11 May 2003 12 UTC, for a) liquid water potential temperature, b) total specific humidity, c) virtual potential temperature, d) liquid water content, e) virtual potential temperature excess and f) vertical velocity. In the figures, the adiabat is depicted, as well as the updraft and mean profiles (for a), b) and c) only).

5.3.4 Discussion

The REF run set up in the 1D Single Parcel Ascent Model shows good results for the chosen case studies 10 and 11 May 2003. In general, we observe the simulated parcel ascents to generate vertical profiles that are in good agreement with typical shallow cumulus values, which gives us confidence in the performance of the model in order to make an estimate of cloud convective properties.

Unfortunately, we have seen some discrepancies with respect to the considered observations. First of all, we have to remark here once again that 1D SPAM is a fairly simplified reconstruction of reality. We consider the modeled clouds to have bulk properties and sharp boundaries in the periphery and hence do not take into account the inhomogeneity of cumulus clouds. This is caused by the mass-flux approach that is commonly used and accepted, in spite of this simplification. On the other hand, the mass-flux approach is very useful in the description of an ensemble of clouds in one grid box, as we would like to achieve here.

The parameters in the REF run that we set up in subsection 5.3.1 were chosen on basis of recent LES studies, but they were tuned on simulating clouds as good as possible according to the observations. This means that we of course can set up another run that describes cloud boundaries and in-cloud profiles better than REF, but this would not be in agreement with the goal of evaluating a unified formulation for the trigger function.

5.4 Evaluation with aircraft observations

5.4.1 Introduction

As mentioned in chapter 3, for validation purposes the Merlin IV aircraft of Meteo France delivers the most useful measurements for thermodynamic profiling of the cloud layer. The great amount of instrumentation on board gives us opportunity to compare sampled data points in cumulus clouds and their environment with output of the 1D SPAM offline model for several events during the Golden Days of the BBC2 campaign.

Figure 5.21 shows the flight tracks of the Merlin on 10, 11 and 21 May 2003. Note the prevailing easterly orientated tracks after Cabauw overpasses, in order to avoid the forbidden airspace around airport Schiphol. The flights are also listed in Table 5.4. On 10 and 21 May a morning and an afternoon flight were carried out, while on 11 May only one flight (morning) can be seen. This might be related to the frontal system that takes possession of The Netherlands in the early evening of the 11th (subsection 5.3.3), which made it rather senseless to perform a flight with the focus on boundary layer clouds in the afternoon.

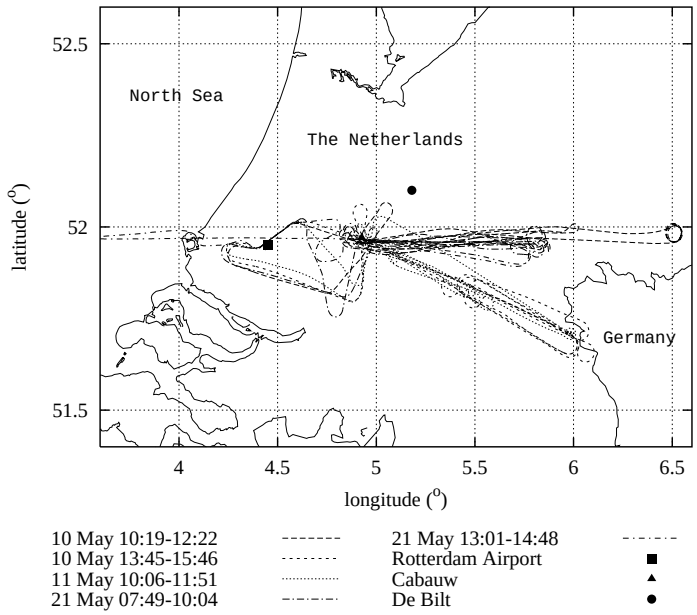

FIGURE 5.21 Flight tracks of the Merlin aircraft on 10, 11 and 21 May 2003. The triangle, dot and square denote Rotterdam Airport, Cabauw and De Bilt respectively.

To gather a significant amount of sampled points that we can compare with model output, we first sampled the Merlin data sets on geographical position. This was done for all points in a grid box of $0.5^\circ \times 0.5^\circ$ around Cabauw, which leaves us with measured profiles that represent an area of approximately $50km \times 50km = 2500km^2$. Secondly, we downsampled the signal for computational reasons to 20 Hz, and such that the measured vertical profiles did not change at a glance. This implies a resolution of about 5 metres for a typical cruise speed of $100ms^{-1}$. For a qualitative comparison purpose, we assume this sampling frequency to be sufficient.

Date	**Flight**	**Flight time** (*hrs* UTC)	**Profile used**	**Profile boundaries** Lower – upper (*m*)	**Comparison time** (*hrs* UTC)
10 May	M10-01	10:19 – 12:22	A	1600 – 3000	11:10
	M10-02	13:45 – 15:46	-		
11 May	M11-01	10:06 – 11:51	A	1600 – 3000	10:00
21 May	M21-01	07:49 – 10:04	B	1000 – 2500	09:00
			C	600 – 2900	09:50
	M21-02	13:01 – 14:48	-		

TABLE 5.4 Merlin flights during the BBC2 Golden Days 10, 11 and 21 May 2003. For the comparison with model output, we used the nearest ascent at which a cloud was detected. Subsequent profiles during one flight – which are already sampled in 0.5^o x 0.5^o grid box around Cabauw – are listed as A, B, C etcetera.

A comparison of the liquid water content instruments mounted on the Merlin is presented in Figure 5.22. The aircraft was equipped with a Gerber PVM-100 and a King probe. We note that the measured values agree considerably well with each other, especially for the lower values of q_l. The results shown in this section are based on measurements with the PVM-100 probe. We here remark

that in this subsection, liquid water content values are presented in g/m^3. Such a value of q_l of course corresponds to a certain value in g/g, which can be achieved by a multiplication with the density of air.

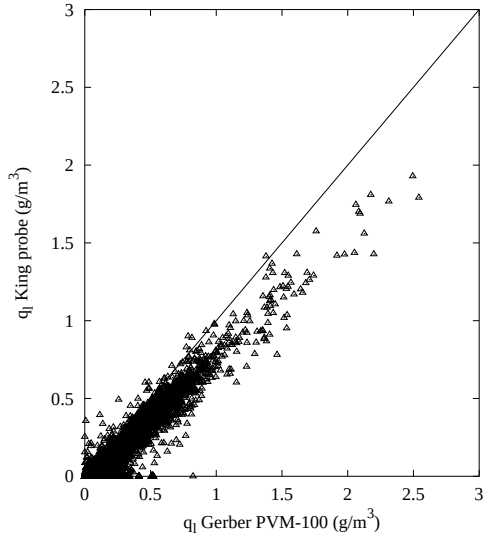

FIGURE 5.22 Scatterplot of liquid water content measured with instruments mounted on the Merlin IV aircraft. The used PVM-100 observations for all five flights on the x-axis versus King probe measurements.

5.4.2 Evaluation events

Measurements gathered during three flight tracks of the Merlin on the chosen BBC2 Golden Days 10, 11 an 21 May are analyzed and compared with output of the REF run of 1D SPAM that was also used in subsection 5.3.

Merlin flight M10-01

Figure 5.23 shows the altitude of all the points and the grid box sampled points during flight M10-01, in the morning of 10 May. The used profile (A) was flown around 10:30 and has a vertical range of 1600 – 3000 m. Thereby, data is only sampled on position – inside the Cabauw 0.5° x 0.5° grid box – hence no further conditional sampling was carried out.

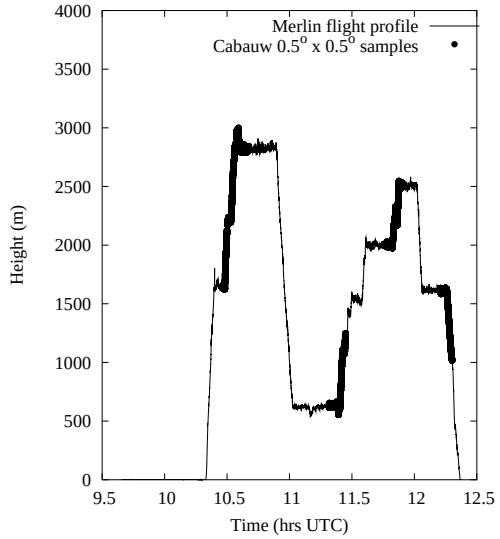

FIGURE 5.23 Time series of altitude for Merlin flight M10-01 for all points (line) and sampled points in the 0.5° x 0.5° grid box around Cabauw (dots).

In Figure 5.24, the comparison of the observed vertical profiles of θ_v, w and q_l with 1D SPAM output is presented. We note a good resemblance between the aircraft observations and the simulated updraft profiles, while outside the cloud (above 2100 m) the profiles show a more environmental behaviour; the virtual potential temperature is in very good resemblance with the mean profile instead of the updraft profile, the vertical velocity is smaller than in the cloud and liquid water content becomes zero. It is also nicely illustrated that lateral mixing indeed occurs in the cloud layer. The maximum values calculated for q_l do not reach the adiabatic profile, which is in general associated with a diluted situation ($\varepsilon \neq 0$).

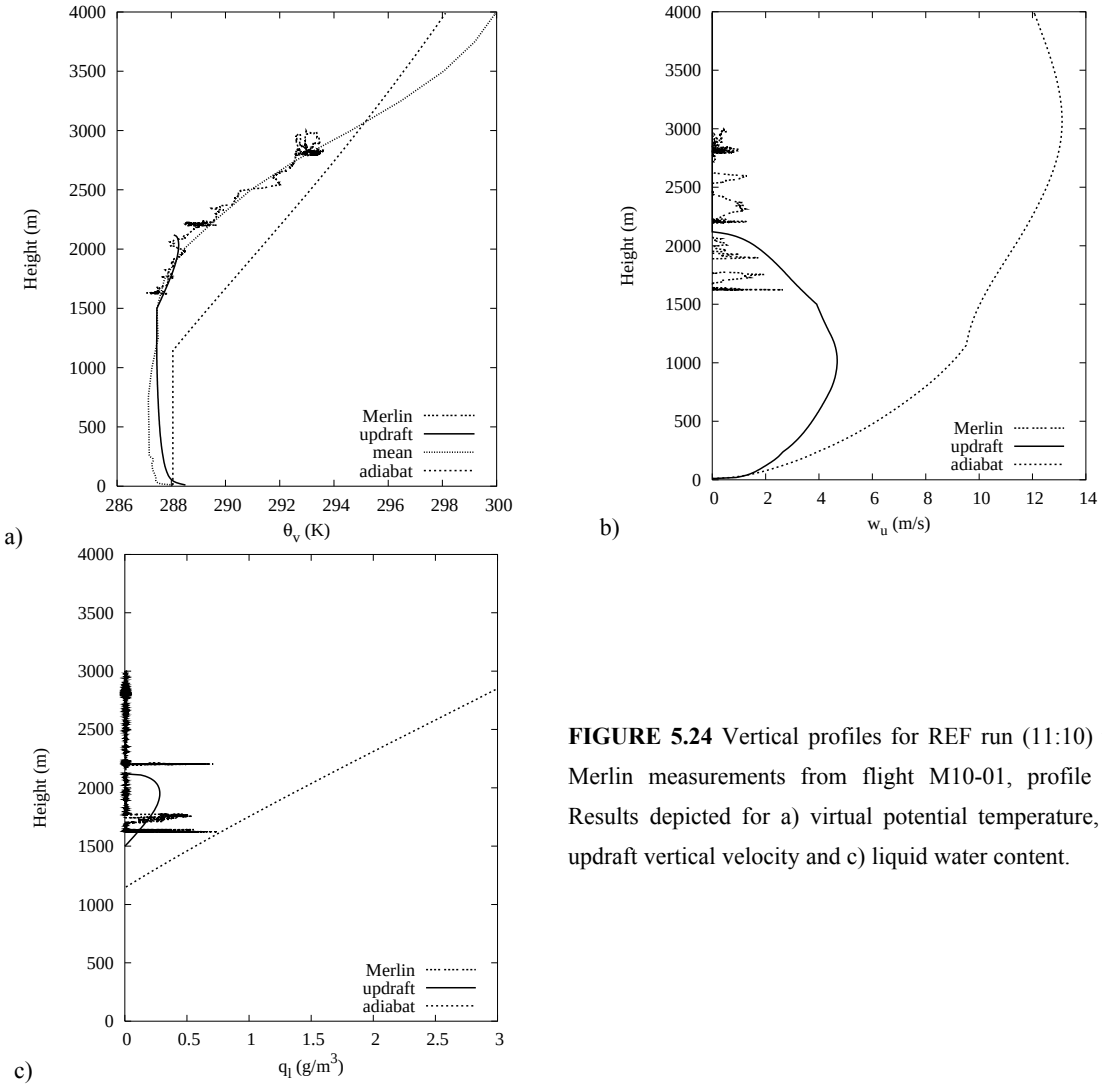

FIGURE 5.24 Vertical profiles for REF run (11:10) vs. Merlin measurements from flight M10-01, profile A. Results depicted for a) virtual potential temperature, b) updraft vertical velocity and c) liquid water content.

Merlin flight M11-01

For 11 May, Figure 5.25 shows the altitude of all the points and the grid box sampled points for flight M11-01, the morning of 11 May. The used profile – the only one available for this flight – started around 10:15 and has a vertical range of 1600 – 3000 m.

In Figure 5.26, the comparison of the vertical profiles of θ_v, w_u and q_l with 1D SPAM output is presented. We again note a good resemblance between the aircraft observations and the simulated

updraft profiles, where especially the change from updraft resemblance (in-cloud) to mean resemblance (above the cloud) of the profile of virtual potential temperature is striking. The maximum observed value of q_l in the lowest cloud layer corresponds also well to the 1D SPAM output of q_l in the respective height interval. Above the cloud a stratocumulus layer is present, which we can recognize in the peak of the profile for liquid water content at a height of approximately 2700 m.

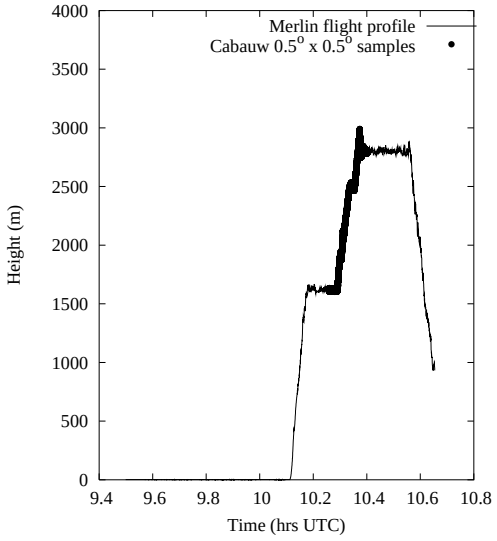

FIGURE 5.25 Time series of altitude for Merlin flight M11-01 for all points (line) and sampled points in the 0.5° x 0.5° grid box around Cabauw (dots).

The observed vertical velocity is substantially smaller than the modeled values, which we can not directly explain. An overview of introduced errors by the measurements, sampling methods and model can be found in subsection 5.4.3.

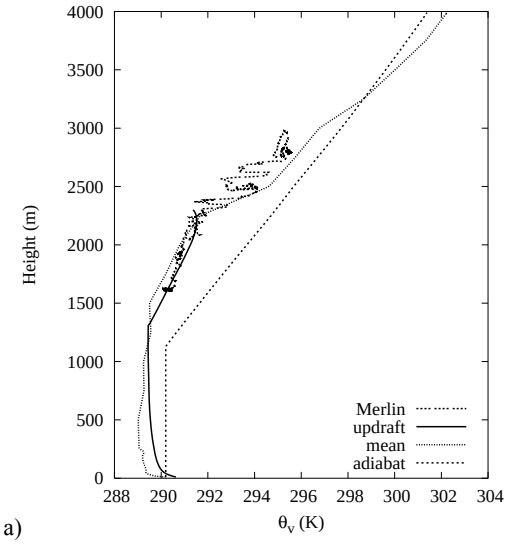

a)

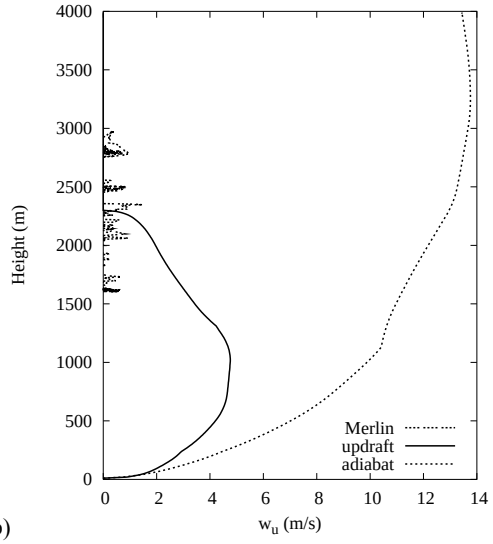

b)

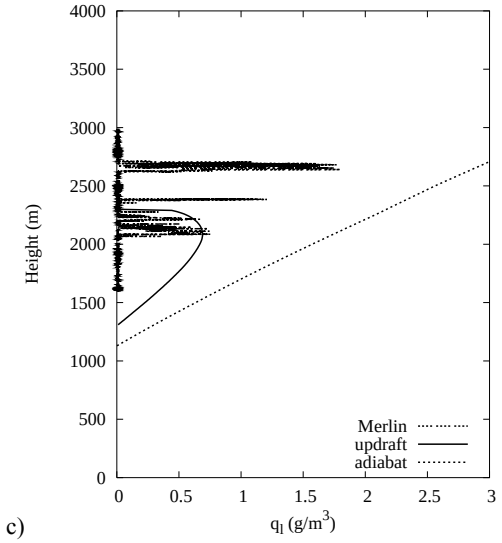

c)

FIGURE 5.26 Vertical profiles for REF run (10:00) vs. Merlin measurements from flight M11-01. Results depicted for a) virtual potential temperature, b) updraft vertical velocity and c) liquid water content.

Merlin flight M21-01

The altitude of all the points and the grid box sampled points for flight M21-01 are presented in Figure 5.27. Two profiles of this flight were used for the evaluation, one started around 09:00 (B) and one around 10:00 (C). These profiles have a vertical range of 1000 – 2500 m and 600 – 2900 m respectively.

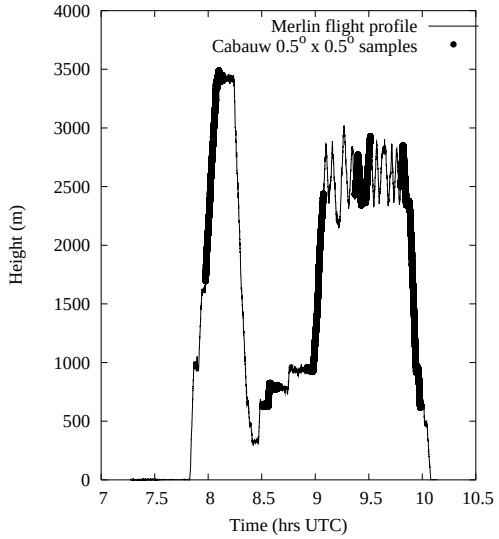

FIGURE 5.27 Time series of altitude for Merlin flight M21-01 for all points (line) and sampled points in the 0.5° x 0.5° grid box around Cabauw (dots).

For the two profiles gathered from this flight, the comparison of the vertical profiles of θ_v, w_u and q_l with 1D SPAM output is shown in Figure 5.28.

We again note a fairly good resemblance between the aircraft observations and the simulated updraft profiles, where especially the change from updraft resemblance (in-cloud) to mean resemblance (above the cloud) of the profile of virtual potential temperature looks very good. The maximum observed value of q_l in the cloud layer corresponds also very well to the 1D SPAM output of q_l in the respective height interval.

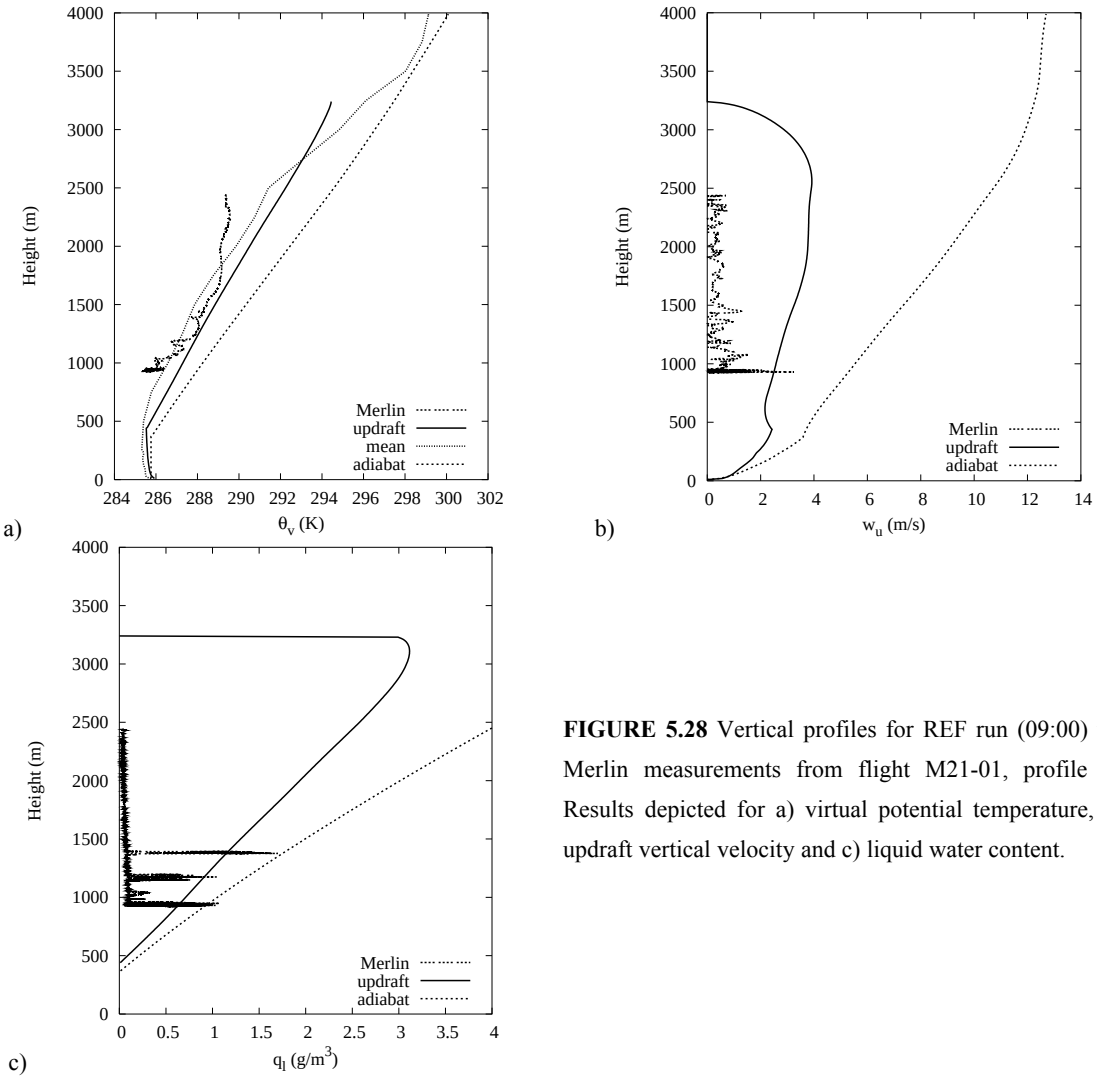

FIGURE 5.28 Vertical profiles for REF run (09:00) vs. Merlin measurements from flight M21-01, profile B. Results depicted for a) virtual potential temperature, b) updraft vertical velocity and c) liquid water content.

For profile C (Figure 5.29) we note that the vertical velocity profile persists in showing a considerably high value with a maximum around 4 m/s until its upper limit at about 2900 m. It agrees very well on an order of magnitude with the model results. Unfortunately, the virtual potential temperature deviates substantially from the modeled updraft profile and shows more agreement with the mean profile, in spite of the cloud presence in the measurements between approximately 800 and 2200 m.

Finally, we note that the vertical gradient of the maximum observed value for q_l resembles the modeled liquid water profile fairly well. We can even see that the maximum values get very close to the adiabatic profile (dotted), reaching peak values of $0.0028 g/m^3$. This is an indication for an actual dilution that is positioned between zero and the dilution prescribed in the corresponding REF run.

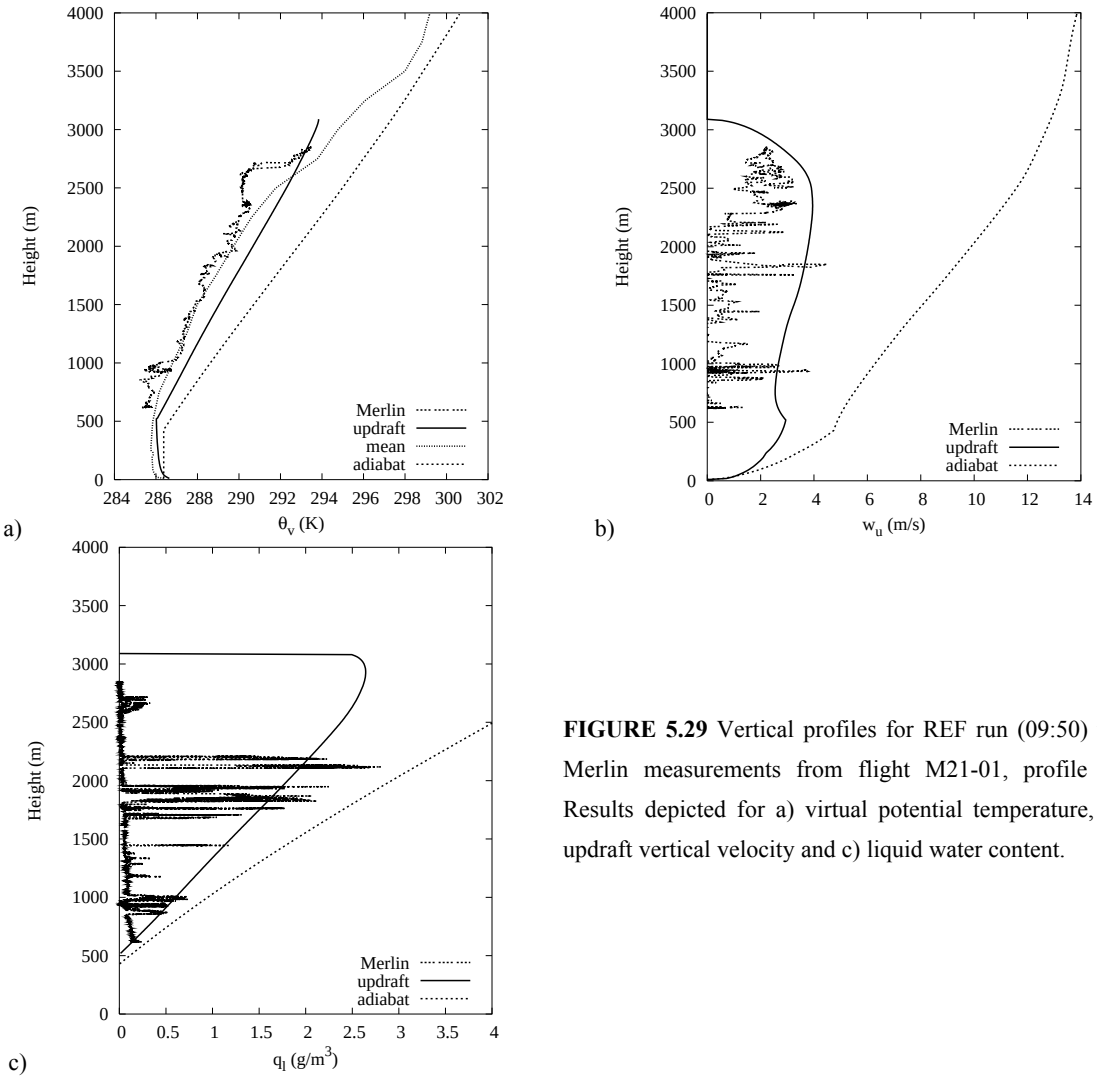

FIGURE 5.29 Vertical profiles for REF run (09:50) vs. Merlin measurements from flight M21-01, profile C. Results depicted for a) virtual potential temperature, b) updraft vertical velocity and c) liquid water content.

5.4.3 Discussion

It should be stressed that, for all measured variables, it is very difficult to estimate the value of the comparison of aircraft observations with output of the 1D SPAM offline model.

The measured profiles of the shown vertical profiles of θ_v, w_u, q_l and T and their variability on a fixed height are strongly dependent on the profile the aircraft has flown through the cloud. If for example the periphery of a cloud is sampled, we expect to find a lower value for liquid water content than for the core of a cumulus cloud. We do not make a distinction between mean cloud ($q_l > 0$) and core ($q_l > 0 \cup w_u > 0$) profiles, but we try to derive an order of magnitude value that we can compare with the 1D SPAM output of the respective variables. We assume this output to be near the maximum values that can be found for the updraft, which gives reason to compare them with the highest values of the mentioned thermodynamic variables measured by the Merlin.

Secondly, the grid box around Cabauw is about $50km \times 50km$ wide, which leaves us with the question if points sampled in this box are representative for output of the parcel model that was initialized with data representative for Cabauw itself. The assumption of homogeneity of e.g.

surface and land use does not seem to be valid anymore. Above that, we can not make a distinction between strongly localized convective clouds and other (stratocumulus) layers that in fact do contribute in the measurements but are not taken into account in 1D SPAM.

Finally, biases in the sensors mounted on the aircraft and errors in the model (and its initialization) contribute in the difficulty to make an estimate of the added value of this airborne evaluation.

5.5 Sensitivity studies

5.5.1 Introduction

The parcel ascent model consists of numerous parameters that have a significant impact on the modeled vertical thermodynamic structure of the ABL and hence on the positioning of cloud boundaries and other critical levels. In the sensitivity study carried out here, we try to gain an insight in the general sensitivity of some essential model parameters. When possible, observations are used to carry out a validation. For certain periods, this is done quite extensively, whereafter the outcome for other BBC2 days is gathered and plotted together to depict the general impact of modifications with respect to the reference run in 1D SPAM.

5.5.2 Sensitivity to sub-cloud lateral mixing

First of all, we would like to sketch a picture of the effects of lateral mixing in the sub-cloud layer. Therefore we make a first estimate of the quality of the chosen REF run with respect to the traditional UND run, by considering the triggered convection by an analysis of the cloud base height. In Figures 5.30 a-c, the modeled and observed cloud base heights are depicted in a scatterplot for each day. The ensemble of these plots is presented in Figure 5.30d.

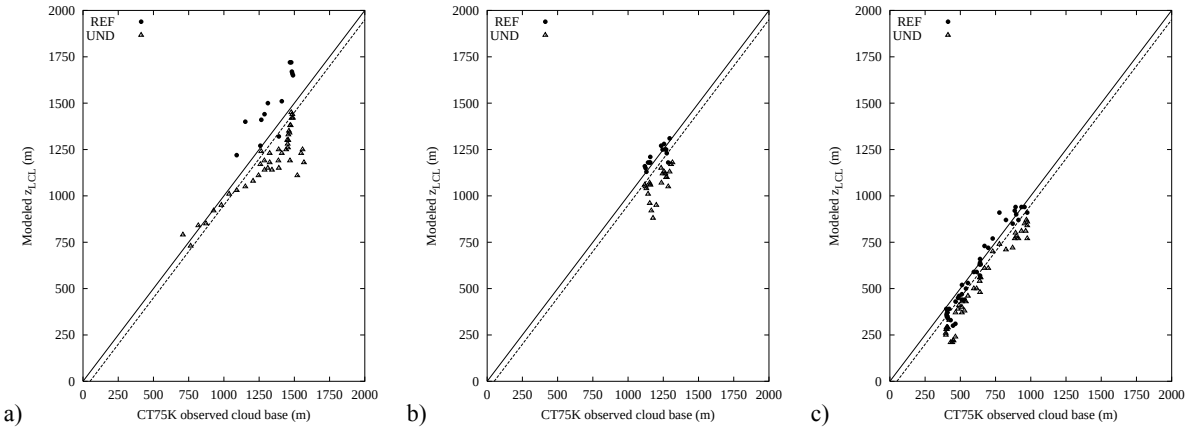

FIGURE 5.30 Scatterplots for observed versus modeled cloud base heights in REF and UND runs on a) 10, b) 11 and c) 21 May. In d), the observations of these three days are depicted together. The solid line represents the line on which the observed and modeled cloud base heights are equal, the dashed line corrects for the 30-60 metres bias in the Vaisala CT75K lidar (see chapter 3).

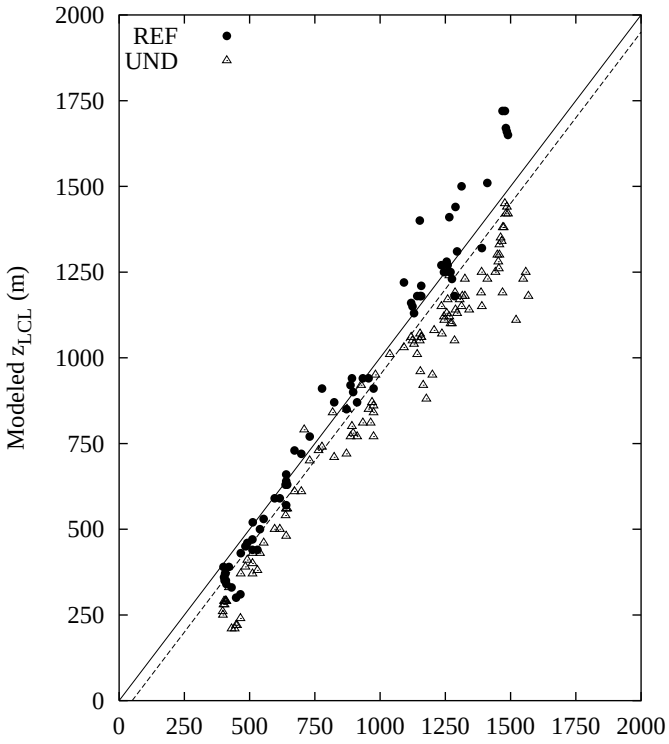

d)

It seems that especially for 11 and 21 May, contrary to the relatively calm 10 May, the REF run tends to pull the modeled cloud bases more towards the observed values. The entraining parcel is subjected to two effects, which counteract each other during the ascent. Due to entrainment of colder air from the environment into the updraft, its saturation specific humidity will decrease which causes the updraft to reach its condensation level lower than in a situation without mixing. On the other hand, the entrainment of dry air from the environment decreases the updraft value for total specific humidity, which on its turn causes a higher condensation level. This is because the profile for updraft total specific humidity in that case deviates more from the saturation curve. Taking into account these two effects, we might have a first indication that the latter prevails above the effect of a lower saturation value, based on Figure 5.30.

5.5.3 Sensitivity to entrainment formulation

The REF run contains an entrainment formulation that was proposed by e.g. Neggers (2002) and Cheinet (2003), i.e. $\varepsilon = \max[c_\varepsilon(1/z), 1/(\tau w_u)]$. It contains a dependency on the inverse product of eddy turnover time and updraft vertical velocity, which was chosen to tune the fractional entrainment rate in regions where it was underestimated. The latter generally occurs near the negatively buoyant region between the LNB and LFC and near the inversion height. To test the sensitivity to several commonly used parameterizations for ε, the sensitivity study in this subsection was performed.

In Figure 5.31 - 5.33 we will focus on the 11:30 UTC parcel ascent on 11 May, investigating the sensitivity to a certain range of entrainment formulations. In Table 5.5, eight flavours of parameterizations for ε are listed.

Name	Sub-cloud $\varepsilon(m^{-1})$	In-cloud $\varepsilon(m^{-1})$	Excess factor b_ϕ	Entrainment factor c_ε
ε_A	0.0	0.0	0.0	0.0
ε_B	0.0	10^{-3}	0.0	0.0
ε_C	$\max[c_\varepsilon(1/z),1/(\tau w_u)]$	$\max[c_\varepsilon(1/z),1/(\tau w_u)]$	1.0	0.4
ε_D	$\max[c_\varepsilon(1/z),1/(\tau w_u)]$	$\max[c_\varepsilon(1/z),1/(\tau w_u)]$	1.0	0.55
ε_E	$c_\varepsilon(1/z)$	$c_\varepsilon(1/z)$	1.0	0.4
ε_F	$c_\varepsilon(1/z)$	$c_\varepsilon(1/z)$	1.0	0.55
ε_G	$c_\varepsilon(1/z)$	$c_\varepsilon(1/z_{LCL})$	1.0	0.4
ε_H	$c_\varepsilon(1/z)$	$c_\varepsilon(1/z_{LCL})$	1.0	0.55

TABLE 5.5 Entrainment formulations used in the sensitivity study. The REF run contains the formulation as shown in the description of ε_C.

The table shows some unified and non-unified prescriptions for ε. Formulation ε_A is associated with a complete undiluted parcel ascent (adiabatic). In ε_C we recognize the REF formulation, while in ε_B the old ECMWF entrainment formulation is presented, i.e. a sub-cloud undiluted parcel ascent with in-cloud a fixed value $\varepsilon = 10^{-3} m$ (for shallow cumulus). If we want to investigate the changes that have been caused by the new formulation, it is thus important to focus on B and C. The values shown for c_ε (0.4 and 0.55) both are in the range of values found in recent LES studies (Jakob and Siebesma, 2003; Siebesma et al., 2004). The excess factor b_ϕ is chosen fixed on 0.0 for undiluted and 1.0 for diluted ascents. Later in this chapter, we will investigate the sensitivity to b_ϕ.

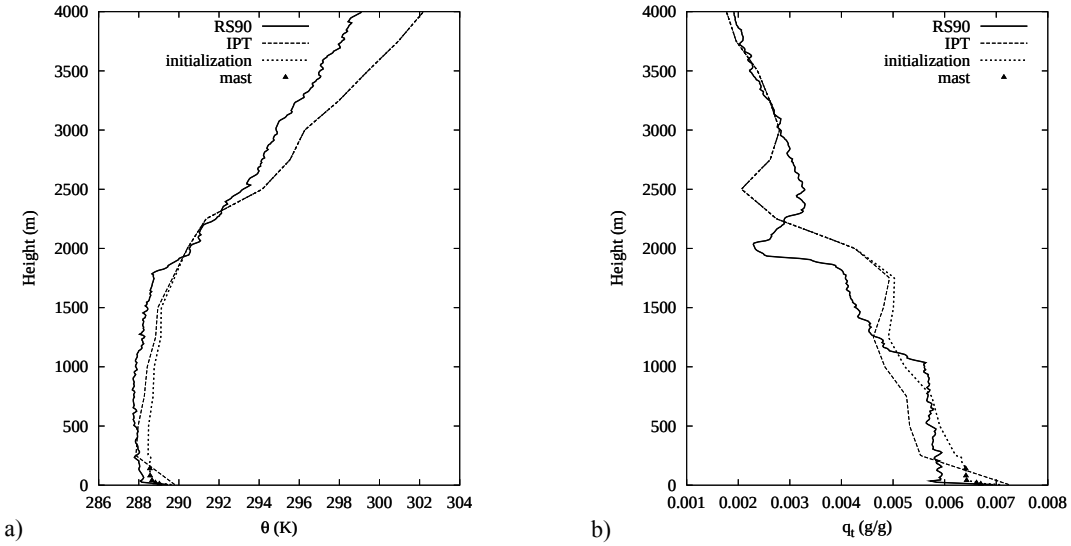

FIGURE 5.31 Mean profiles of a) potential temperature and b) total specific humidity for 11 May 11:30 UTC. Profiles generated by RS90 (solid), IPT (dashed), mast (triangles) and the initialization method that contains as well mast as IPT observations (dotted), are depicted.

In Figure 5.31, the mean profiles of θ and q_t for initialization with the original mast/IPT method and by means of the radiosonde data are shown. At 11:27 a RS90 sonde was launched, which gives us a great opportunity to compare profiles and cloud boundaries between the original and RS90

initialization. We note a striking difference in measured potential temperature in the boundary layer between the IPT and RS90, which might be caused by our translation of the IPT profile towards the mast at the fitting level (chapter 3). This is the case for this specific comparison event, but for other Golden Days this difference is not present to this large extent (not shown). On the other hand, for humidity we note that the translation method has brought the IPT profile closer to the radiosonde.

Figure 5.32 shows us the updraft properties calculated for 11 May 11:30 UTC for the eight different prescriptions for ε. The fractional entrainment rates in the cloud layer are generally somewhat smaller than the typical value of $10^{-3}m^{-1}$ that is known for shallow cumulus. Both of the formulations that are dependent on w_u (C and D) show a minimum in as well the cloud layer as the sub-cloud layer and a blow-up of entrainment rate near the inversion height, as discussed earlier. The only difference between them is the value of c_ε (0.4 and 0.55, respectively).

For the sub-cloud layer we recognize three regimes of profiles for θ_{lu}, $\Delta\theta_v$, w_u and Δq_t, which is associated with the three possible values for c_ε (0.0, 0.4 and 0.55) that are prescribed there. The relatively small value for updraft vertical velocity as well as the fact that we are looking low in the ABL (z is small) causes the fractional entrainment rates that are described with $\max[c_\varepsilon(1/z),1/(\tau w_u)]$ to choose for the $c_\varepsilon(1/z)$ part . Above the detected LCL, which is lowered for the undiluted sub-cloud ascent, the profiles tend to diverge due to the different formulations that hold in the cloud layer. We first note the remarkable 'come-back' of profile B; after a sub-cloud undiluted ascent (together with A) the thermodynamic properties converge towards the in-cloud values of the profiles corresponding to the other formulations, constrained by the in-cloud fixed value $\varepsilon = 10^{-3}m^{-1}$. It is especially very close to formulation D, the most active lateral mixing assumption available in this comparison. Leaving formulation A out of consideration, we observe the highest in-cloud values for e.g. vertical velocity and liquid water content for the in-cloud least mixing updraft that is described by formulation E ($\varepsilon = 0.4/z$). Logically, for E we also find the highest cloud top. On the other hand, we find formulation D to generate the lowest in-cloud profiles of the mentioned variables and also the lowest cloud top. This is enhanced by the $1/\tau w_u$ form of ε, which gives an enormous boost to the prescribed mixing for lower values of the updraft vertical velocity.

The sequence that is seen in the entrainment profiles (from left to right) also determines the in-cloud distribution of thermodynamic properties. I.e. the formulations G and H that adopt the value for ε at cloud base calculated by the sub-cloud c_ε/z, lies between the least mixing (E and F) and the most active mixing (C and D) formulations. This can also be extracted from the sequence of the depicted profiles for the thermodynamic properties and the sequence of calculated cloud top, especially in the figures for w_u and q_{lu}.

Figure 5.33 presents us the same formulation comparison as just discussed, but for the radiosonde input profiles instead of combined mast/IPT profiles. We first note the fairly craggy profiles for $\Delta\theta_v$ and Δq_t, that are a direct consequence of the temperature and humidity profiles measured by the RS90 radiosonde on a relatively high vertical resolution.

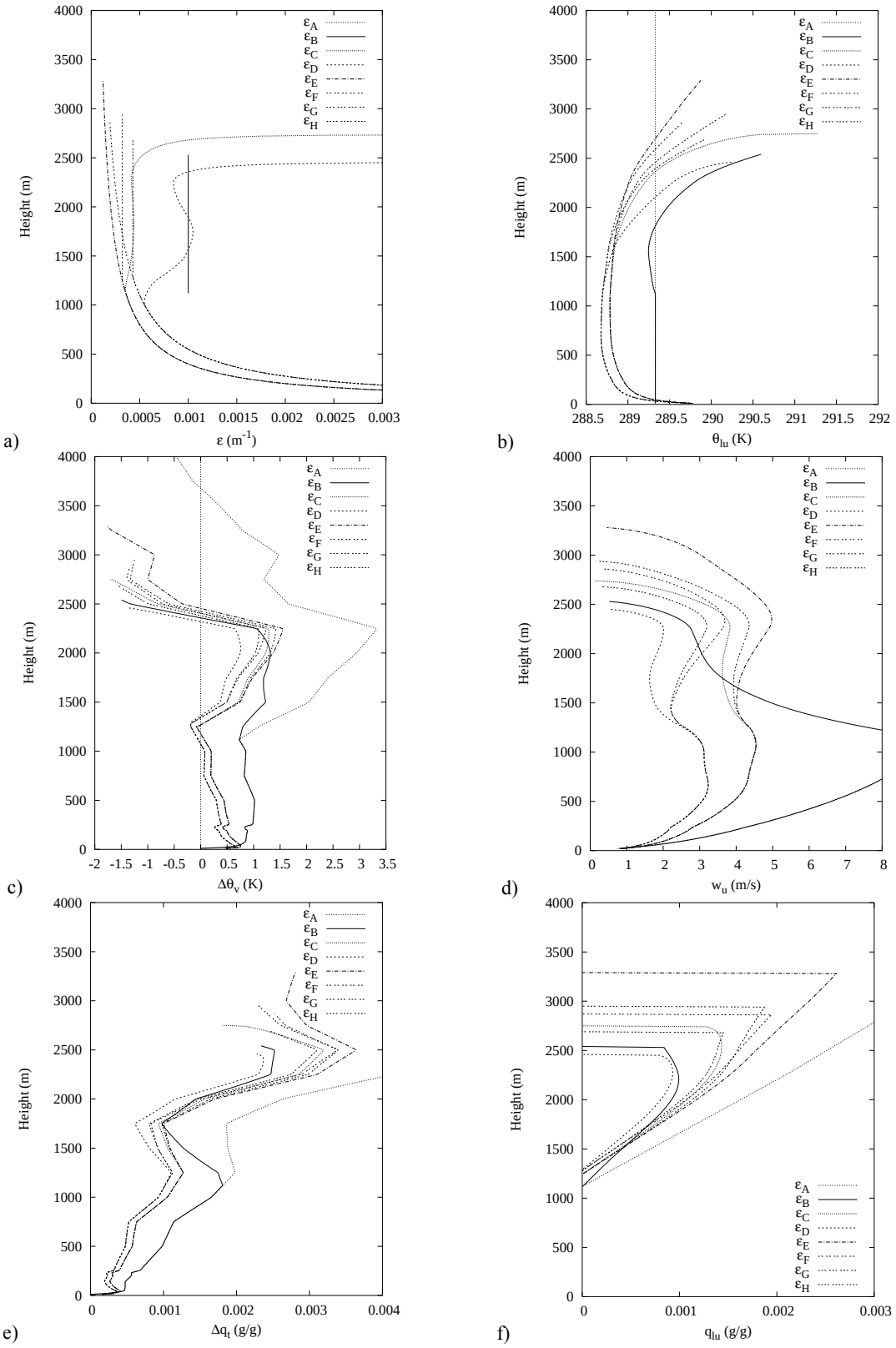

FIGURE 5.32 Updraft properties for eight 1D SPAM entrainment formulations for 11 May 11:30 UTC, as described in Table 5.5. The depicted updraft profiles: a) fractional entrainment rate, b) liquid water potential temperature, c) virtual potential temperature excess, d) vertical velocity, e) total specific humidity excess and f) liquid water content.

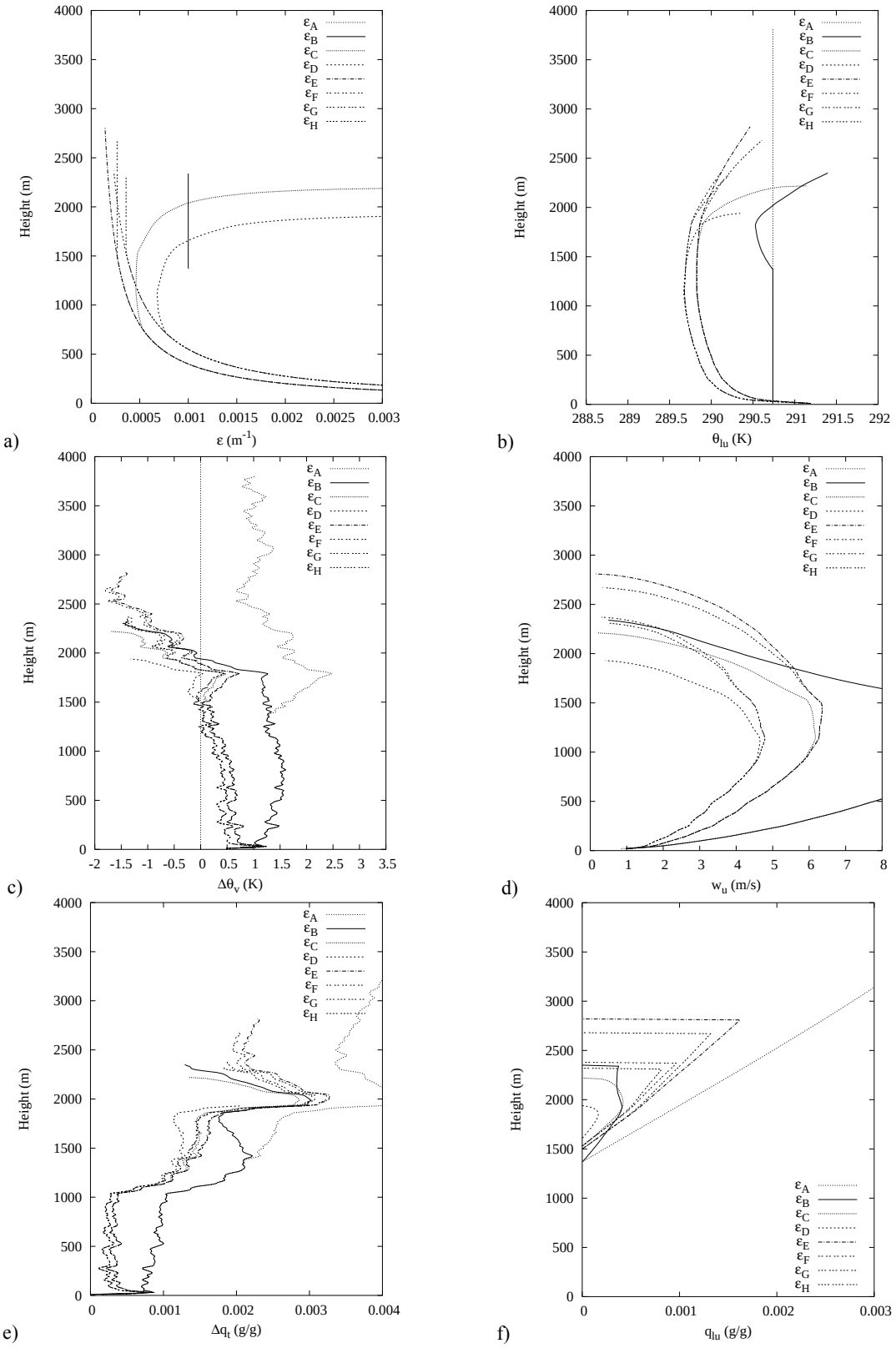

FIGURE 5.33 Same as Figure 5.32, but for RS90 input profiles on 11 May 11:27 UTC.

The sequence of the formulations that we noted in Figure 5.32, is also present here. This implies that the behaviour is the same and we hence find the same formulations that cause the most tempered (C and D) and least tempered (E) profiles for updraft properties and cloud top.

The sub-cloud/in-cloud decoupled shape for w_u is not clearly visible in this figure. This possibly has to do with the marginal virtual potential temperature excess that is observed near cloud base, which logically gives reason for a tempered vertical velocity profile. The cloud base height is higher with respect to the mast/IPT case, which causes the latent heat release that is associated with condensation to start at a higher level.

Furthermore, we notify that in general the absolute values that are calculated for the profiles of e.g. updraft vertical velocity and updraft liquid water content have substantially changed with respect to the case of mast/IPT initialization. In the latter we see e.g. REF maximum values of w_u and q_{lu} in the order of 4 m/s and 0.0015 g/g, while for the RS90 case we observe maximum values of around 6 m/s and 0.0004 g/g respectively. These differences are solely caused by the different initialization profile that is given to 1D SPAM before diagnosing the parcel ascent. Because we are investigating the sensitivity to entrainment formulation here, we will not go into further detail about this aspect but keep it in mind when we evaluate the value that we ascribe to the outcome of the used parcel model.

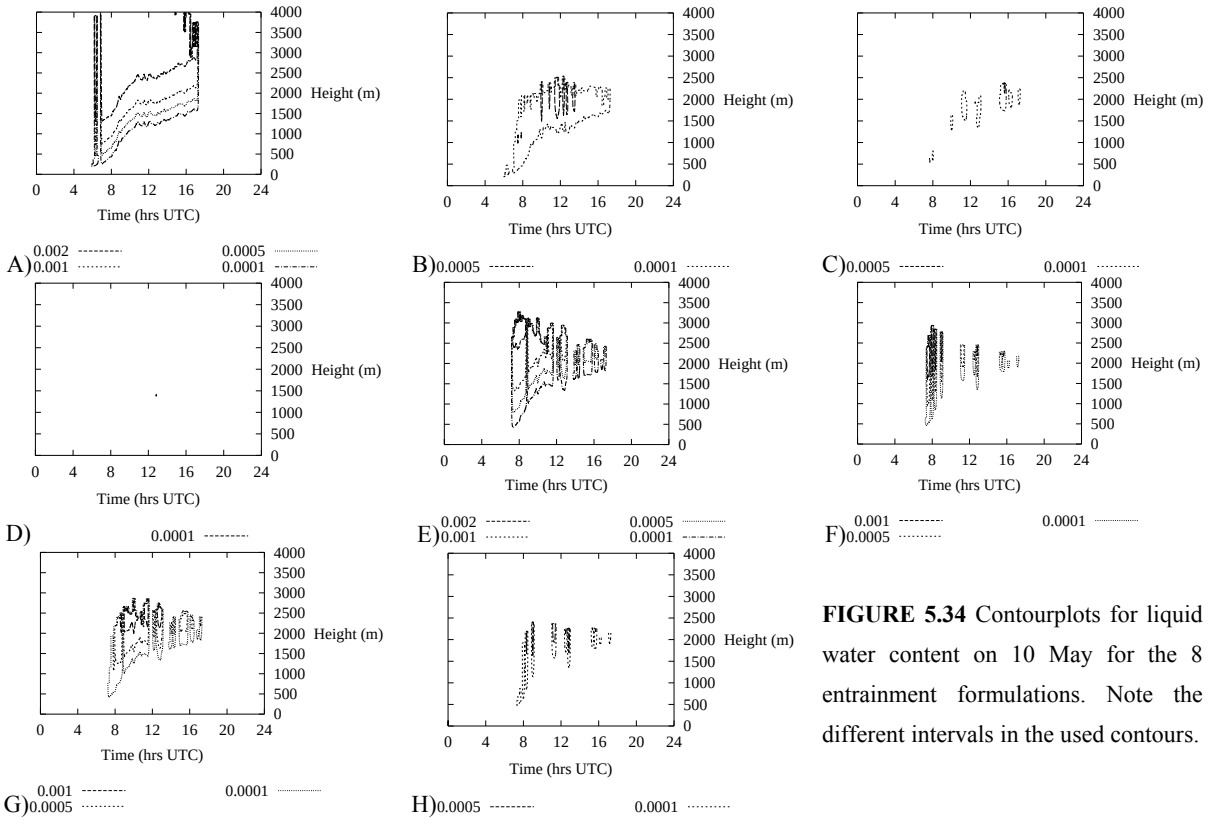

FIGURE 5.34 Contourplots for liquid water content on 10 May for the 8 entrainment formulations. Note the different intervals in the used contours.

To illustrate the overall impact of the 8 investigated entrainment formulations in this section, we depicted the liquid water contours for a mast/IPT initialization on 10 and 11 May in Figure 5.34

(and 5.35). The reader can notify here that in general, a higher entrainment factor c_ε especially reduces the presence of the simulated clouds. This logically follows from the idea that it is more difficult for thermals to penetrate and make it as a cloud, considering increasing lateral mixing. Furthermore, we observe a lowered cloud top for these cases (D, F and H) with respect to their corresponding formulation with a lower c_ε (C, E and G).

The undiluted ascents that are associated with A do not even reach a cloud top in the chosen 4 km domain, while B shows cloud boundaries that fairly agree to a typical value that follows from the other formulations. That formulation D contains the most enhanced lateral mixing is nicely seen in its contourplot for both days, where only a few thin clouds are shown.

As we have seen in Figures 5.32 and 5.33, the vertical velocity dependency of ε in C and D is hardly seen in the sub-cloud layer because c_ε / z prevails above $1/\tau w_u$ for the biggest part here. This causes the cloud base height not to differ very much for the various formulations, if one groups the formulations with the same c_ε. A more detailed comparison of cloud presence and cloud base height on 11 May is presented in Figure 5.36. It is shown that the sub-cloud undiluted formulations A and B underestimate cloud base height and overestimate cloud presence. We can clearly see this phenomenon demonstrated in the uninterrupted line of the modeled LCL that is positioned much lower than results of the diluted formulations and the CT75K observations. For this day, we already compared the lidar observations with video images (Figure 5.13 and 5.14) and concluded that three distinct shallow cumulus periods should occur under the second cloud layer.

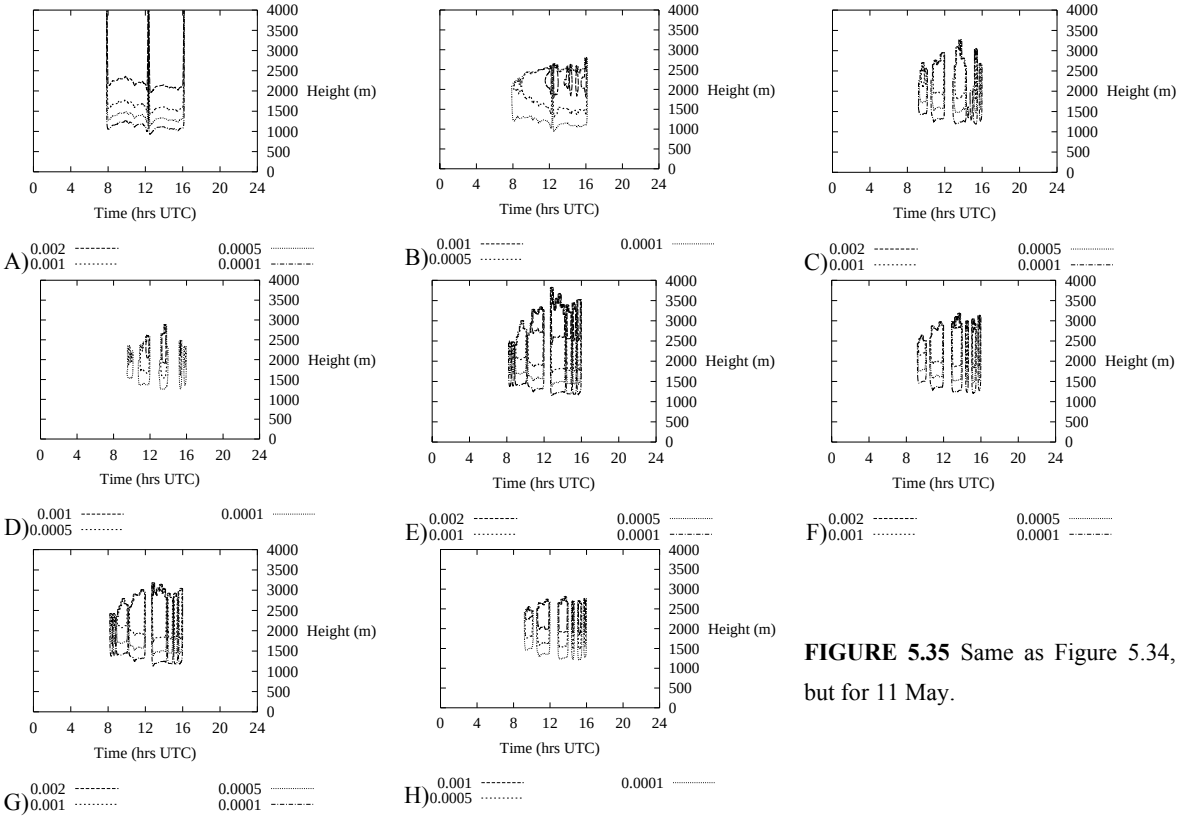

FIGURE 5.35 Same as Figure 5.34, but for 11 May.

Note that a significant number of the modeled cloud base heights in Figure 5.36 coincide (E and G, F and H) and hence can not be distinguished. The general image is that sub-cloud dilution causes a suppressed presence of cumulus clouds, as we had already noticed in the contourplots for liquid water. The diluted formulations are performing considerably better than the sub-cloud undiluted formulations A and B, for the considered cases. Furthermore, we note that the formulations containing the dependency on w_u generally lead to a higher LCL, caused by an increase in fractional entrainment rate just below the modeled cloud. This increase is seen for example in Figure 5.32a for formulation D, where ε increases from 1000 m due to the twofold expression, while cloud base is detected just around 1250 m.

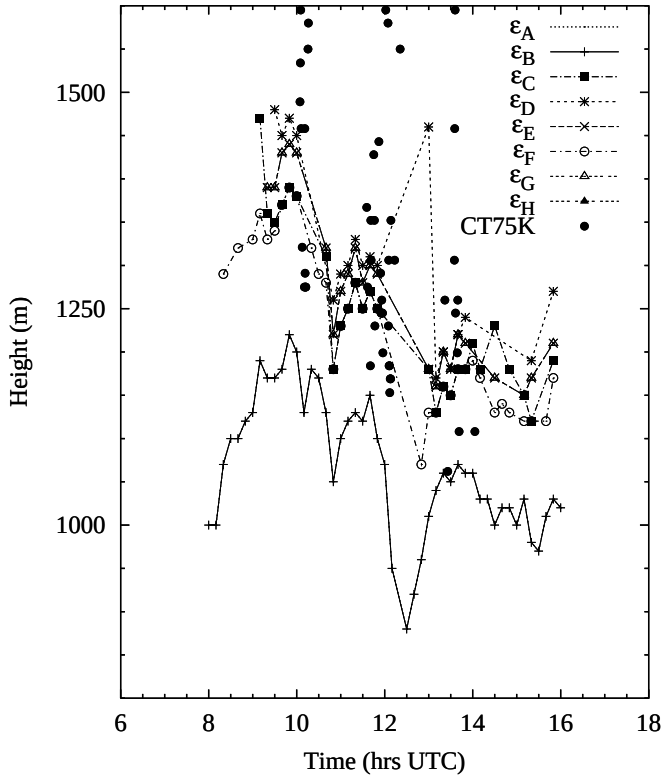

FIGURE 5.36 Modeled cloud base heights for the 8 different 1D SPAM entrainment formulations, as described in Table 5.5. The black dots represent the corrected CT75K observations of shallow cumulus on 11 May.

5.5.4 Sensitivity to parcel release height

The height at which the parcel starts its ascent and obtains the prescribed excesses, may also be important to the cloud convective properties we are interested in. For the ECMWF model this height is chosen 10 m which is possible due to its high vertical resolution, but other GCMs generally choose their first model level. This can be in the range 10 – 100 m and one can imagine that this might have an enormous effect on the updraft properties that are calculated during the ascent. There have been indications that a fractional entrainment prescription that is inversely proportional to height might deal with this problem, because it shows an independent behaviour to properties of the parcel at the release height. (Jakob and Siebesma, 2003). Therefore we compared the REF and UND run on 11 May 11:30, see Figure 5.37. Furthermore an entrainment formulation associated with $0.4/z$ is shown (5.37b).

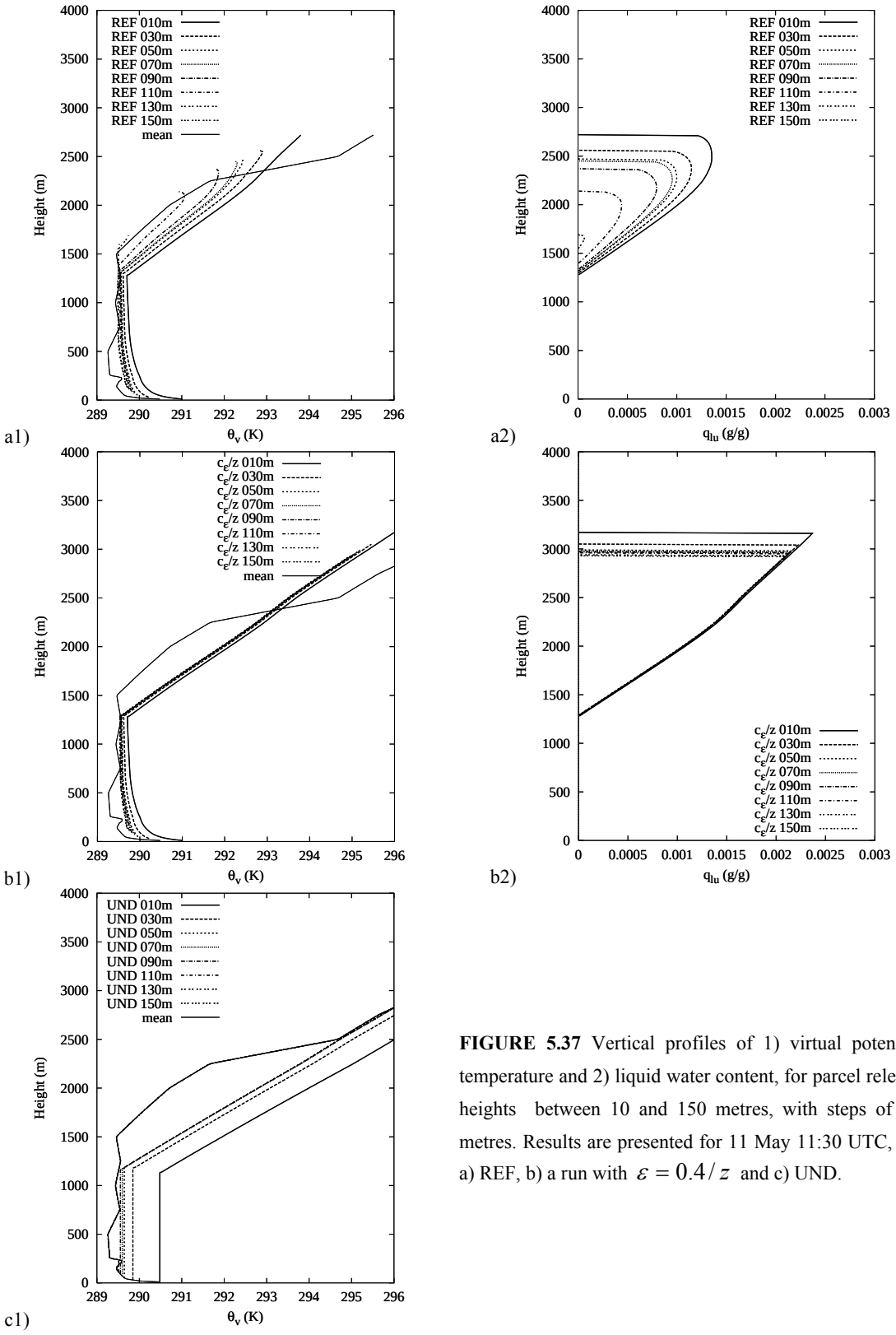

FIGURE 5.37 Vertical profiles of 1) virtual potential temperature and 2) liquid water content, for parcel release heights between 10 and 150 metres, with steps of 20 metres. Results are presented for 11 May 11:30 UTC, for a) REF, b) a run with $\varepsilon = 0.4/z$ and c) UND.

The REF updraft profiles of θ_v show that parcels released higher in the surface layer reach their lifting condensation level higher in the ABL. Here, it should be stressed that the results for 10 m

and 30 m release height substantially deviate in all panels from the results for other release heights, because of the extreme (negative) gradients of the mean profiles of potential temperature and specific humidity in the lowest part of the surface layer. This is nicely illustrated in the sub-cloud layer of the θ_v profiles in the UND case and can be seen in e.g. the difference of approximately 0.7 K between the 10 m and 30 m value.

The nice features of the $1/z$ entrainment description are also shown in Figure 5.37. The profiles for θ_{vu} and q_l converge very well (especially in-cloud). Analogous to that, the cloud boundaries are less sensitive to release height than in the case of the REF run. Cloud base height is located at a fixed point as the reader can observe in the starting point of the liquid water content profiles. Subsequently, only for the earlier discussed 10 and 30 m release heights the cloud top is heightened with about 180 and 70 m respectively. We hereby notice, that in spite of the lower sensitivity, the absolute updraft values of e.g. q_l and w_u (not shown) are considerably larger due to a weaker in-cloud entrainment than in REF. The formulation that is used in REF plays a significant role here, because of the dependency on the updraft vertical velocity. We can see that the virtual potential temperature excess is larger for parcels that are released lower, which causes a higher buoyancy and hence a higher value for the resulting vertical velocity. This on its turn causes a suppressed fractional entrainment rate, which is expressed in a typical in-cloud value of $5 \cdot 10^{-4} m^{-1}$ for $z_r = 10m$ against $1.2 \cdot 10^{-3} m^{-1}$ for $z_r = 150m$. Apparently, this difference in entrainment rate fully determines the change in for example maximum in-cloud liquid water content and cloud top.

For the REF profiles it holds that parcels that are released lower, generate a higher cloud top and a lower cloud base. The spread that is found in cloud base heights is considerably less with respect to the UND run, as shown in Figure 5.38. We note again that cloud presence for 10, 11 and 21 May is also reduced in the REF case, according to the lower number of points found in the respective scatterplot.

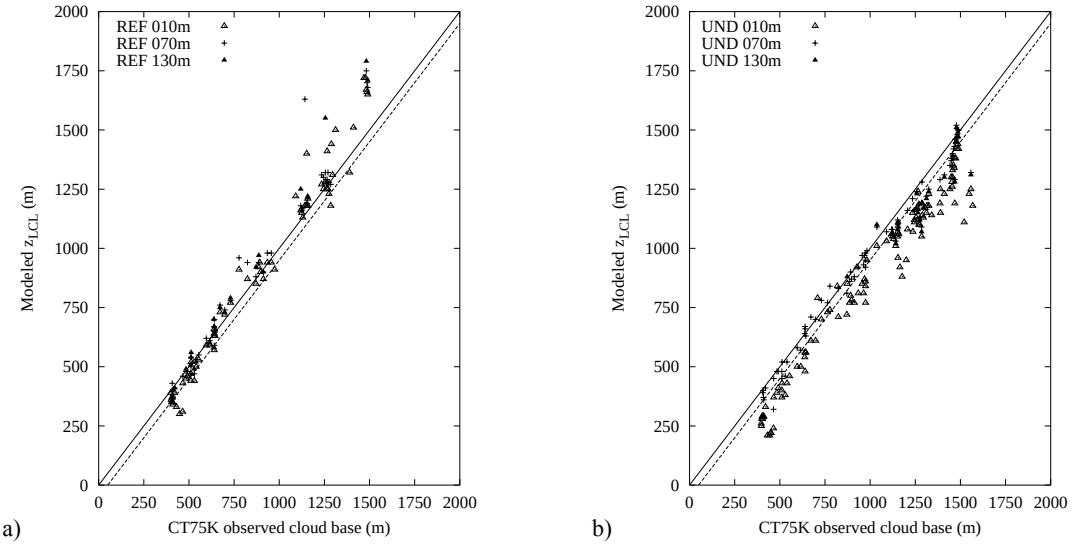

FIGURE 5.38 Scatterplot for observed versus modeled cloud base heights in a) REF and b) UND runs for 10, 11 and 21 May. Results for release heights 10 m, 70 m and 130 m.

Finally, we generated contourplots for liquid water content on 10 and 11 May, presented in Figures 5.39 and 5.40. Overall, we notice less and thinner clouds for increasing release height, which has to do with the lower excesses a parcel is subjected to when it is released higher. This is primarily caused by the large negative gradients in temperature and humidity in the lowest part of the surface layer.

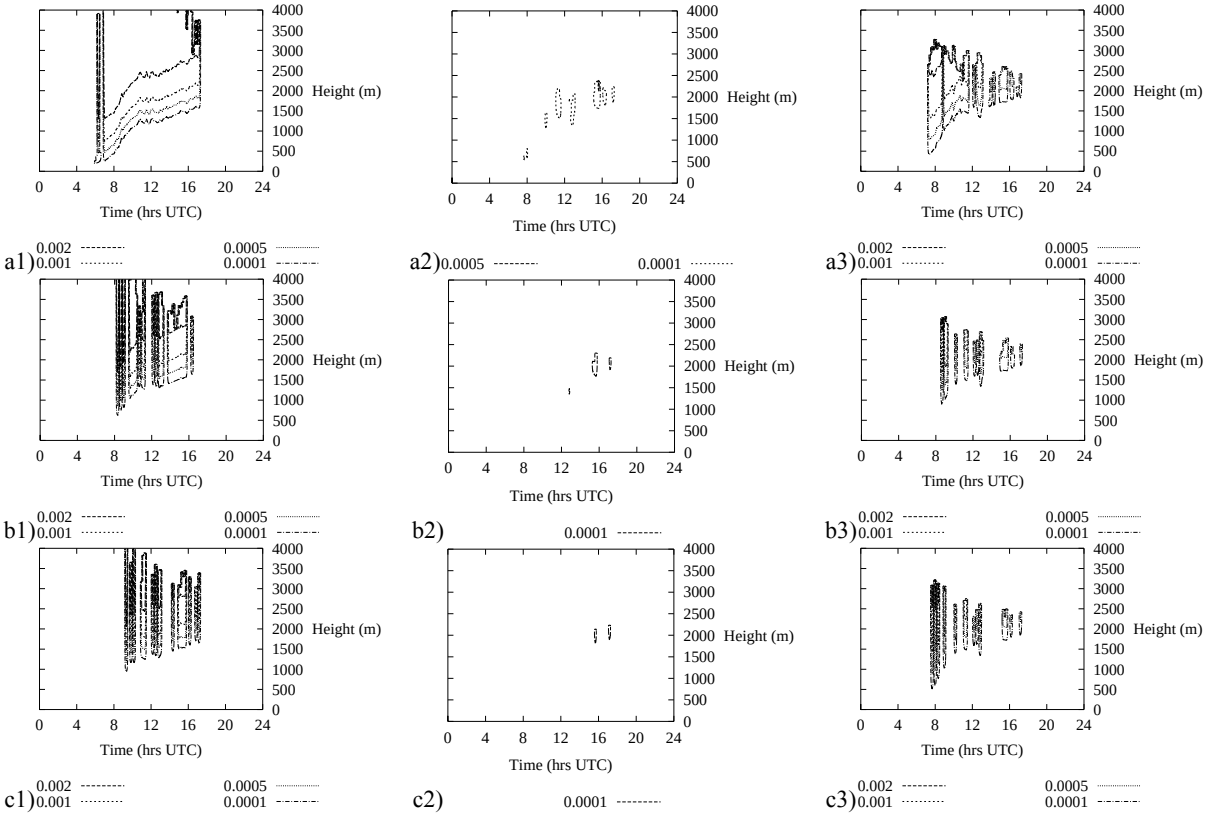

FIGURE 5.39 Contourplots for liquid water content on 10 May. Results for release heights a) 10 m, b) 70 m and c) 130 m for 1) UND, 2) REF and 3) a run with prescribed $\varepsilon = c_\varepsilon / z$.

Furthermore, we observe the earlier mentioned large extent of insensitivity to z_r for the $0.4/z$ formulation. This is demonstrated in cloud presence as well as in cloud boundaries. Thereby it should be remarked that it is not that clearly visible for 10 May as it is for 11 May. In analyzing the updraft profiles of θ_v and q_l we already noticed that in spite of this favourable behaviour, as a consequence the values that are modeled for e.g. liquid water content are substantially higher.

We thus have shown that both of the dilution formulations (c_ε / z and REF) have their own advantages and disadvantages, with respect to the sensitivity study carried out here. Sensitivity of cloud boundaries and updraft profiles to release height is enormously tempered in the case of c_ε / z, while the cloud properties themselves obtain very high values. This is mainly caused by a relatively low value of ε in the cloud layer.

On the other hand, cloud boundaries and updraft profiles in REF show a huge sensitivity to release height, but the cloud properties like liquid water content and vertical velocity, as well as cloud top,

show more reasonable values with respect to (lidar and aircraft) observations. This property gives the opportunity to tune the parcel model with respect to the parcel release height.

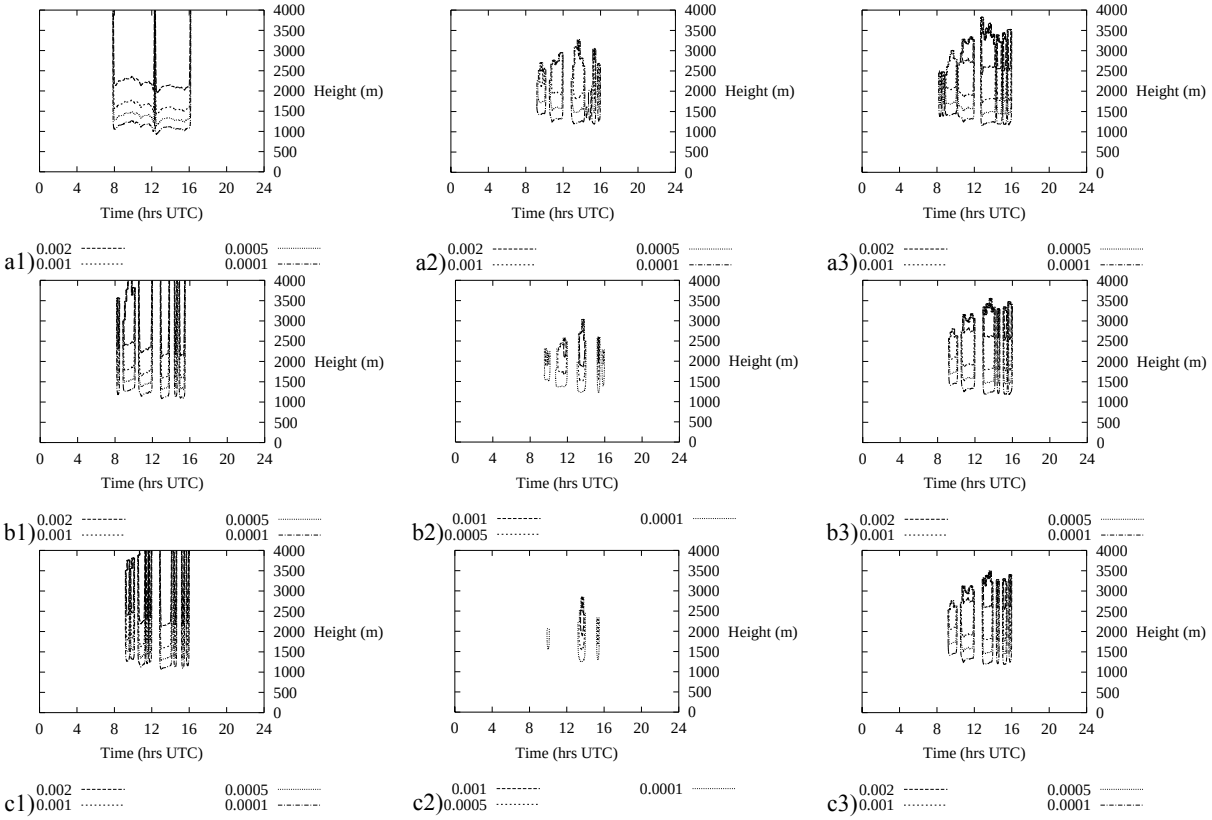

FIGURE 5.40 Same as Figure 5.39, but for 11 May.

5.5.5 Sensitivity to release excesses

The last sensitivity we investigate in this study is the sensitivity to the excess factor that determines the excesses in temperature and humidity, given to the rising parcel at the release height. As the reader can conclude from chapter 4, this excess for the updraft properties $\phi_u = \{\theta_{lu}, q_{tu}\}$ is assumed to scale with the surface flux of the corresponding property divided by the standard deviation for vertical velocity at z_r. The (excess) proportionality factor b_ϕ, that is not necessarily equal for θ_l and q_t, is set on 1.0 in the REF run that is discussed in subsection 5.3.1.

#	b_{θ_l}	b_{q_t}
1	0.0	0.0
2	1.0	1.0
3	0.0	1.0
4	1.0	0.0
5	2.0	2.0

TABLE 5.6 Excess factors used in Figures 5.41-5.43.

The REF run of 1D SPAM contains the formulation as shown in description #2.

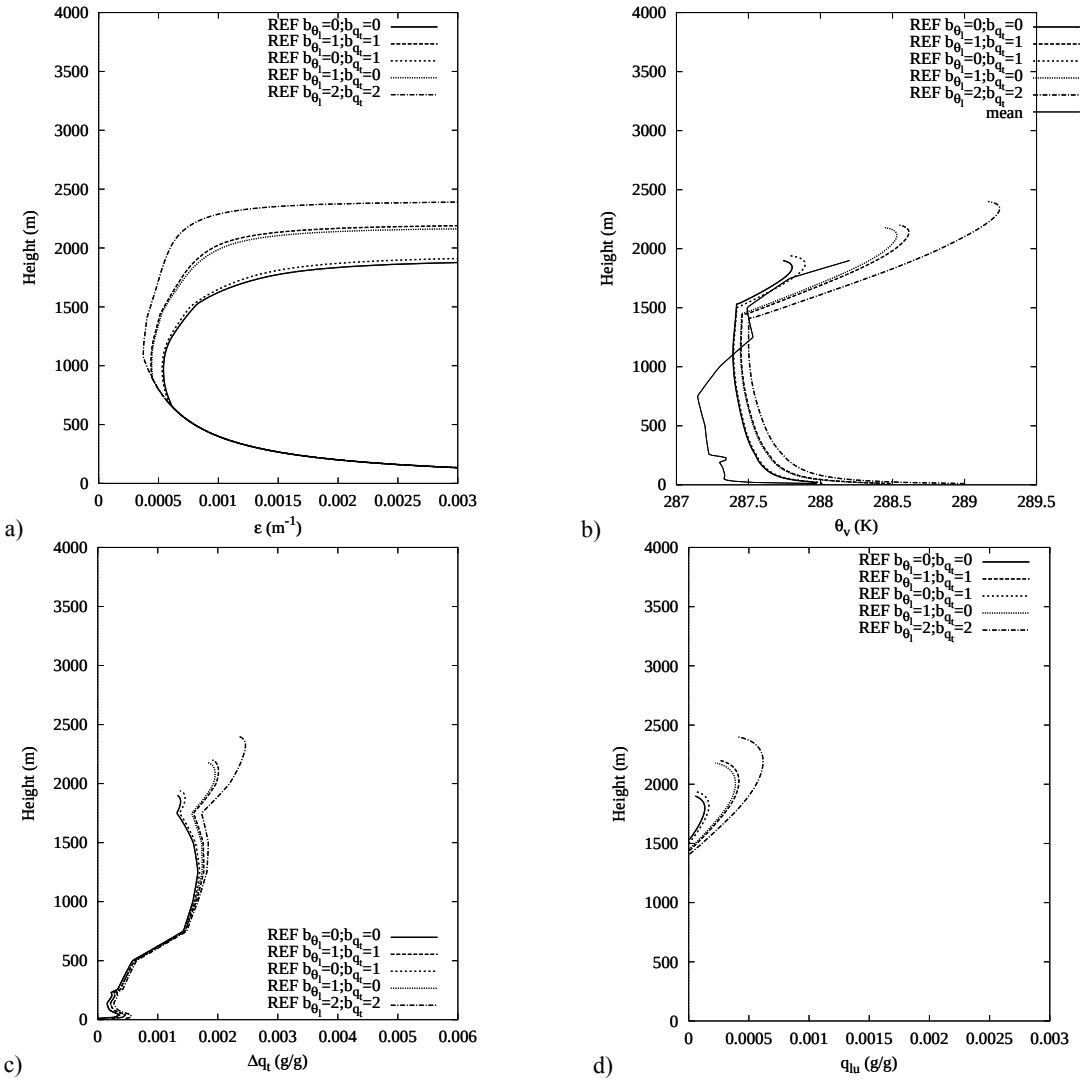

FIGURE 5.41 Vertical profiles of a) fractional entrainment rate, b) virtual potential temperature, c) total specific humidity excess and d) liquid water content, for 10 May 11:30 UTC. Results are presented for the five combinations of excess factors as described in Table 5.6.

For the 10 May 11:30 response, Figure 5.41 shows the updraft profiles for the five combinations of excess factors b_{θ_l}, b_{q_t} that are listed in Table 5.6. Except for the changed excess factors, we use the same parameters as specified in the REF run. For this time, the ambient surface fluxes $\overline{w'\theta_l'}$ and $\overline{w'q_t'}$ have values of $0.19 Kms^{-1}$ and $0.11 gmkg^{-1}s^{-1}$, which lead to maximal excesses of 0.84 K and 0.49 g/kg in case of combination #5 with a given value $\sigma_w(z_r) = 0.45 ms^{-1}$ (equation 4.16). For 11 May 11:30, depicted in Figure 5.42, these surface fluxes were equal to $0.21 Kms^{-1}$ and $0.07 gmkg^{-1}s^{-1}$. Besides, $\sigma_w(z_r) = 0.46 ms^{-1}$.

First of all, we note that cloud base is the lowest and cloud top is the highest for the case with the most enhanced release excesses (#5). Because the formulation of ε is again twofold, we note that e.g. for 10 May a few hundred metres below the detected cloud base, the $1/\tau w_u$-dependent part prevails above c_ε / z. This is the main cause for the lower cloud base, while for lower excess factors (combinations #1 - #4) this transition between the two formulations inside the max-operator

(equation 4.11) occurs lower in the ABL. The higher value for ε above this transition height causes a higher cloud base. Because the parcel becomes negatively buoyant, warmer air from the environment will mix into it, which causes the saturation value to increase. Subsequently, the entrainment of dryer air from the environment causes the updraft total specific humidity to decrease. Taking into account both of these effects, we indeed expect a higher LCL, because they both act in the same direction. This is only the case for these negatively buoyant parcels between the height at which switching of the entrainment formulation occurs and cloud base height. This is illustrated in the figures for 11 May (Figure 5.42). The positively buoyant parcels there cause an almost unchanged cloud base height, because the two effects mentioned above counteract each other and more or less compensate.

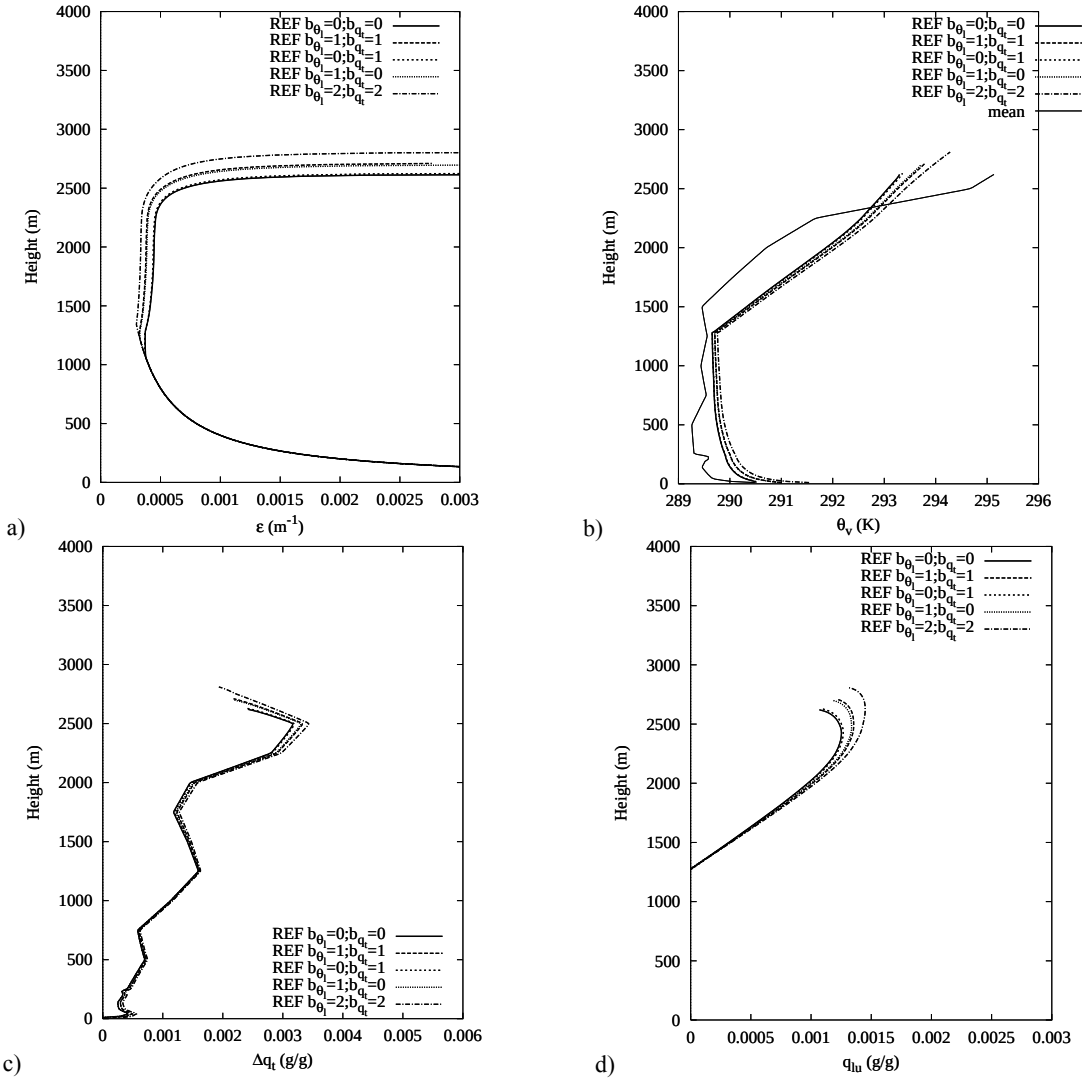

FIGURE 5.42 Same as Figure 5.41, but for 11 May 11:30 UTC.

Above all, we observe in Figure 5.41 and 5.42 that it is especially the excess factor for temperature, b_{θ_l}, that makes the difference in the vertical profiles of the presented updraft properties. For example, we notice that a change from the situation with no excesses (b_{θ_l}, b_{q_t} = 0,0) to a situation with only an excess in specific humidity (b_{θ_l}, b_{q_t} = 0,1) hardly has any impact on the modeled

updraft profiles. On the other hand, a change to a situation with only an excess in liquid water potential temperature (b_{θ_l}, b_{q_t} = 1,0) delivers completely different updraft profiles. Together with the higher cloud top, this gives support to the statement that the response to the given initialization profiles is more sensitive to changes in b_{θ_l}, than it is to changes in b_{q_t}. This behaviour is caused by a positive feedback that acts through the dependency of ε on updraft vertical velocity, in general higher in the ABL. The sub-cloud generation of more buoyancy for higher values of b_{θ_l} causes a lower fractional entrainment rate due to a larger build-up of vertical velocity. We did not investigate this sensitivity with respect to a c_ε / z entrainment formulation, but we surely expect to find a lower sensitivity of cloud thickness and in-cloud properties to the release excess factors in that case.

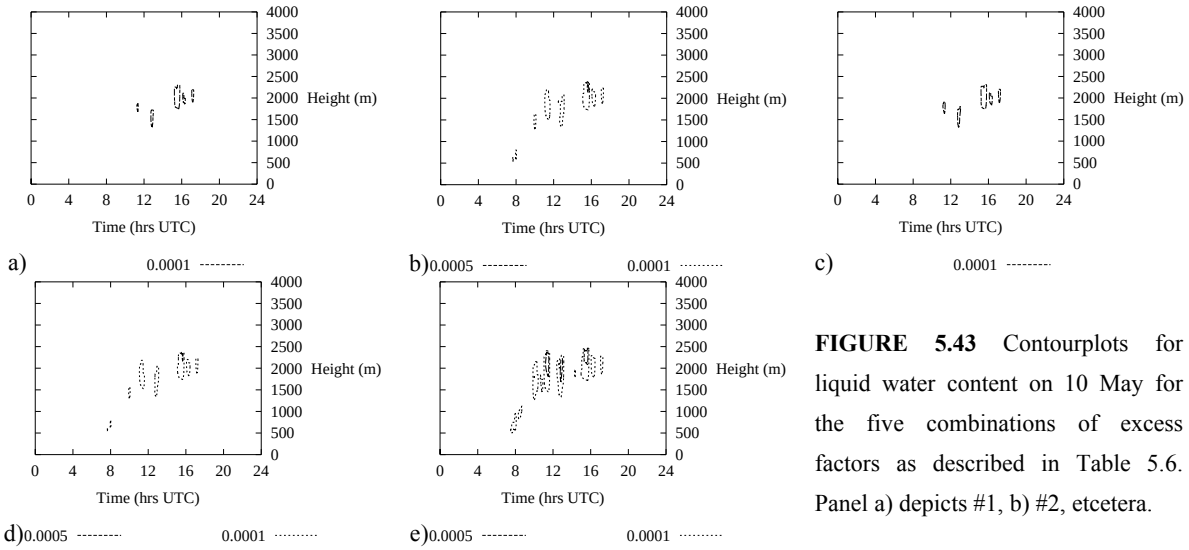

FIGURE 5.43 Contourplots for liquid water content on 10 May for the five combinations of excess factors as described in Table 5.6. Panel a) depicts #1, b) #2, etcetera.

To illustrate the overall response to changing b_{θ_l}, b_{q_t}, contourplots for liquid water content on 10 May are presented in Figure 5.43. We here note again that it is especially b_{θ_l} that has a substantial impact on the cloud response to the given initialization profiles; a) and c) are almost equal, the same holds for b) and d). As we have discussed in the text above, this is mainly caused by REF's twofold formulation for the fractional entrainment rate.

5.5.6 Discussion

In this section, we have tried to gather a general image of the sensitivity of cloud properties to certain model parameters that are very essential for the proposed new trigger function.

The sensitivity of a property to a model parameter is strongly dependent on the environmental circumstances, i.e. the mean profiles of thermodynamic quantities. Looking at a certain set of vertical profiles on a fixed time therefore might be dangerous sometimes, because the mean thermodynamic profiles may contain unrealistic biases that cause the sensitivity not to occur or to occur the other way around. For this reason, we have considered more events and e.g. looked at contourplots of liquid water to get a complete daily overview of the general sensitivity of cloud boundaries to each model parameter.

In the sensitivity to entrainment formulation (see subsection 5.5.3) we have seen that a change in the mean profiles for input in 1D SPAM generates significant absolute differences in modeled updraft properties. The profiles generated for mast/IPT and RS90 input show more or less the same general relative behaviour but in absolute sense we have noticed considerable differences. With the correction procedure for the combined mast/IPT profiles still in mind, this gives us reason to handle the obtained results with care. Of course, the performed sensitivity studies are valuable for a study like this one because we are able to study the relative behaviour to certain prescribed changes in model parameters. Nevertheless, we should not overrate it considering the observed discrepancies in the absolute values.

5.6 Identification of thermal structures

5.6.1 Introduction

For thermal structure identification purposes, BBC2 did not provide optimal conditions, while sonic anemometers were only operational at 5 and 180 metres. The sonics at the levels in between, at 60 and 100 metres, were mounted afterwards and measurements started mid August 2003.

For 10 May, 15 May, 16 August and 13 September 2003, we first carried out wavelet analysis (subsection 5.6.2) on the convective period 09:00 – 14:00 UTC in half-hourly intervals. Analysis of the global wavelet spectra gives us information about how much variance of the signal is explained by coherent structures associated with a certain period. With this result, we would like to find dominating thermal time scales for each level, hoping that it is fairly constant in time. By considering the mean horizontal wind speed, we can make an estimate of the length scale that is associated with thermals.

With the derived time (and length) scale we have solved a part of the thermal criterion (see subsection 4.5.2), on which we can sample high-frequent time series of humidity, temperature and vertical velocity. This is also carried out for daytime during BBC2 and non-BBC2 days, in subsection 5.6.3. Collecting properties for selected thermal data points, we can build up statistics about mean thermal anomalies which we use eventually for making an estimate of the excess factors b_{θ_l} and b_{q_t}, which are essential parameters in the offline parcel model 1D SPAM.

5.6.2 Wavelet analysis

In Figure 5.44, wavelet analysis results are shown for the 5 and 180 m time series of humidity, temperature and vertical velocity, for 10 May 11:30 – 12:00. The global wavelet spectrum gives us information about the time scale at which most of the energy variance of the signal is explained.

We note a large extent of thermal time scale consistency for the different variables at 5 m, while the spread in the maximum at 180 m shows a higher uncertainty. For this specific case, we find average values $T_c = 23.5 \pm 1.0s$ for the 5 m level and $T_c = 43.4 \pm 7.9s$ for the 180 m level.

The obtained dominating time scale for the period 09:00 – 14:00 UTC for the studied days is presented in Table 5.7, of course only for the available mast levels. In this table, a gradual increase in dominating time scale with increasing height can be recognized, as also presented in the average values in Figure 5.45.

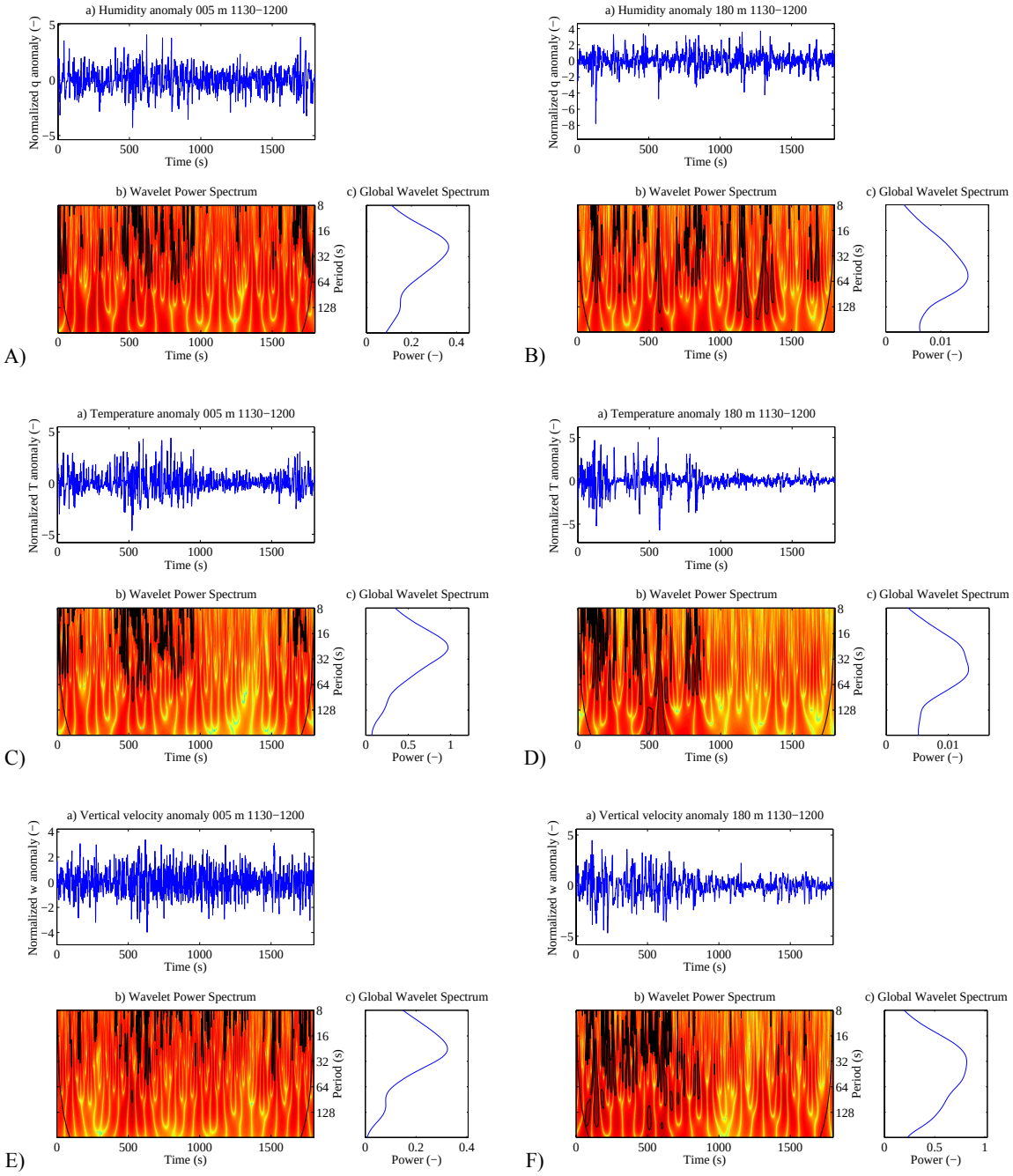

FIGURE 5.44 Wavelet analysis results for 10 May 11:30 – 12:00 UTC for time series of A) humidity 5 m, B) humidity 180 m, C) temperature 5 m, D) temperature 180 m, E) vertical velocity 5 m and F) vertical velocity 180 m. Results shown in a) (variance-normalized) time series of respective quantity, b) wavelet power spectrum and c) global wavelet spectrum. Wavelet power increases with darker colors in the wavelet power spectrum (b).

In this figure, we notice that besides the increasing average thermal time scale, the spread in the time scale also increases with height. The dots printed at each level depict the locations of the maximum in global wavelet spectrum that were found for the half hour intervals during the convective period of the four analyzed days. For the 5 m level, we observe values between 18.9 and 39.1 s, with an average of 27.1 s. This is in good agreement with results from Krusche and de Oliveira (2004), who found a surface layer coherent structure duration between $23.7 \pm 0.5s$ and $37.8 \pm 3.0s$ for three sonic anemometers located at 3, 5 and 9.4 m.

Date	**var**	**5 m** $T_c(s)$	**60 m** $T_c(s)$	**100 m** $T_c(s)$	**180 m** $T_c(s)$
10 May 2003	q	30.2 ± 6.7	-	-	40.6 ± 13.2
	T	28.5 ± 6.1	-	-	36.5 ± 8.3
	w	22.8 ± 1.9	-	-	35.5 ± 10.2
15 May 2003	q	27.0 ± 3.0	-	-	36.0 ± 6.4
	T	27.6 ± 3.0	-	-	38.7 ± 14.8
	w	23.8 ± 3.5	-	-	47.2 ± 16.6
16 August 2003	q	27.2 ± 4.4	-	35.2 ± 9.2	34.0 ± 8.1
	T	27.7 ± 4.1	-	36.7 ± 11.3	41.6 ± 15.1
	w	28.6 ± 3.5	-	40.0 ± 10.7	39.2 ± 10.7
13 September 2003	q	27.8 ± 6.6	33.4 ± 10.7	29.9 ± 4.4	38.6 ± 12.4
	T	30.0 ± 7.3	31.0 ± 4.7	30.7 ± 8.3	31.1 ± 8.7
	w	24.4 ± 3.2	36.1 ± 7.5	33.5 ± 7.7	40.7 ± 13.8

TABLE 5.7 Results for derived thermal time scale for the four analyzed days. Presented time scales are mean values for 10 intervals of 30 minutes, in the period 09:00 – 14:00 for the corresponding day. For each averaging interval, this time scale corresponds to the first maximum in the global wavelet spectrum.

As discussed in chapter 4, we can calculate the corresponding length scales by making use of the Taylor hypothesis, which tells us to multiply the found time scale with the mean absolute horizontal wind speed $ff = \sqrt{u^2 + v^2}$ for the corresponding averaging period. This delivers us the following length scales for the 5 m level: 10 May 110 to 190 m, 15 May 50 to 80 m, 16 August 40 to 70 m and 13 September 30 to 70 m, with daily average values of 133 m, 67 m, 59 m and 57 m, respectively. Thereby we should mention that only 10 May is subjected to fairly high horizontal wind speeds, with a value of 4.9 m/s on average. The other days are more tempered and have mean horizontal wind speeds between 2.0 and 2.5 m/s for the convective period. Nevertheless, it seems that we can not detect a systematic connection between the derived thermal time scale and the horizontal wind speed. Maybe that more statistics would assign such a function of ff. Next, we have tried to find a relationship between T_c and boundary layer height h or the stability parameter z / L_{MO}, where L_{MO} represents the Monin-Obukhov length scale. Unfortunately, these studies were also not succesful.

We will hereafter focus on the 5 m level for two reasons. First of all, the spread in time scale generally increases with height, which may also cause higher uncertainties in mean thermal properties derived by making use of this time scale. Furthermore, the prescribed release height in

the REF run is 10 m, which is located reasonably close to the 5 m sonic level. For our purposes, this level thus offers the best opportunities.

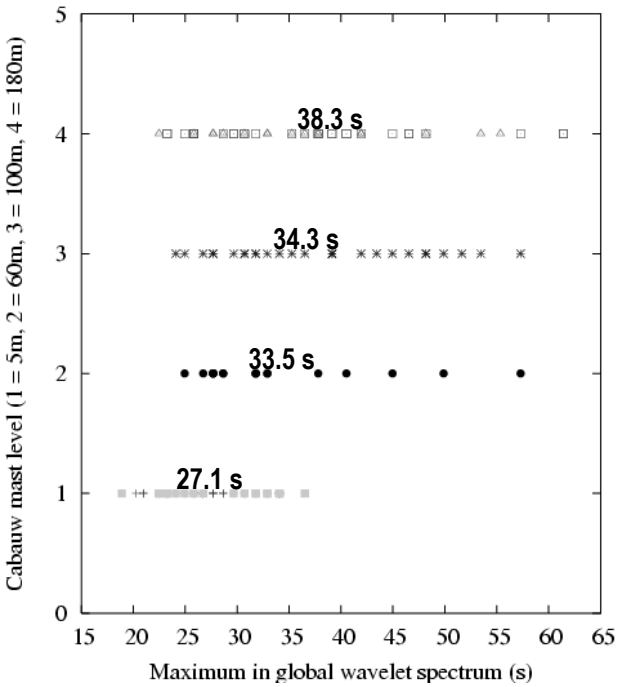

FIGURE 5.45 Overview of the dominating time scales for the four sonic anemometers in the Cabauw mast, for the 09:00 – 14:00 periods on 10 May, 15 May, 16 August and 13 September. Values presented in the figure are average values for temperature, humidity and vertical velocity for these four days.

It should be stressed that a direct bias is introduced with the derivation of the maximum in the global wavelet spectrum, due to resolution limitations in the wavelet scale $s_j = s_0 2^{j\delta j}$. This uncertainty grows with the wavelet scale index j and can be estimated in the range 0.3 s – 8.7 s for the shortest and longest wavelet scales respectively. It has not been taken into account in the analysis of derived dominating time scales, of which the results have been presented in Table 5.7.

5.6.3 Thermal sampling

With the derived prevailing time scale we can sample the used data sets on the occurrence of thermals. Of course, prior to doing so, we have to make a choice in criterion parameters (see subsection 4.5.2). Two combinations of criterion parameters are chosen, which are presented in Table 5.8.

For the BBC2 days 10, 11 and 15 May and the non-BBC2 days 16 August and 13 September, we split up the 10 Hz data sets of temperature, humidity and vertical velocity in the period 09:00 – 16:00 UTC in twelve half hours (averaging period $\tau_c = 1800s$). On these data sets we carried out thermal sampling for a given thermal time scale of 15.0 s. This was chosen such that, according to the lower limit of derived time scale out of the wavelet analysis for 5 m (i.e. 18.9 s), all the

structures that apparently contribute are indeed taken into account. Considering these five days, the results in this section are based on a total of 70 half hours of sonic anemometer data.

#	Time scale $\tau_c(s)$	Averaging period $T_c(s)$	Criterion
1	15.0	1800	$T' > 0 \bigcup q' > 0$
2	15.0	1800	$w' > 0$

TABLE 5.8 The two different sampling methods, with the criterion parameters as discussed in subsection 4.5.2. The sensitivity to each of them in the determination of the excess factors is discussed in this section.

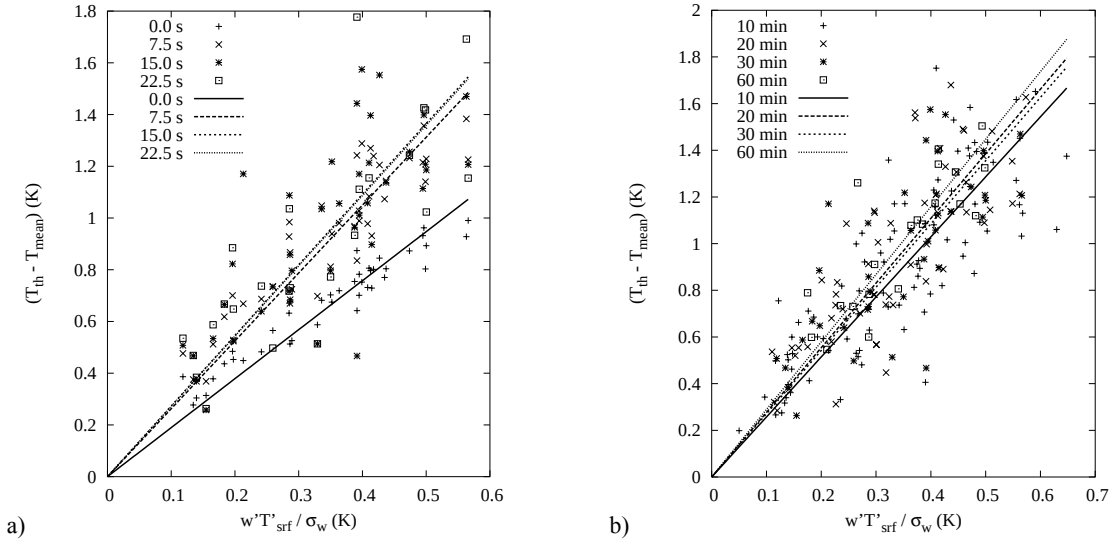

FIGURE 5.46 Criterion #1 sensitivity to chosen criterion parameters for 10, 11, 15 May, 16 August and 13 September 2003, depicting resulting fits for the derivation of excess factor b_T . Results split up in sensitivity to a) thermal time scale and b) averaging period.

Criterion #1 is more consistent with the intuitive interpretation of a thermal in the surface layer, especially when we take into consideration the release excesses that are given to the parcel in 1D SPAM. The thermal has to be warmer and moister than its environment in first place, which forms a good basis for this selection criterion. On the other hand, without vertical velocity a thermal is not able to contribute to convection in a later stadium, which favours criterion #2 at a glance. Above all, the LES studies in which the value of this excess factor ($b_\phi = 1.5$) is estimated take into account the strongest 1% to 5% of the updrafts that are simulated in the respective run. Although the criteria do not exactly match, this also is more in favour of criterion #2, provided that we want to compare the results with the mentioned LES study.

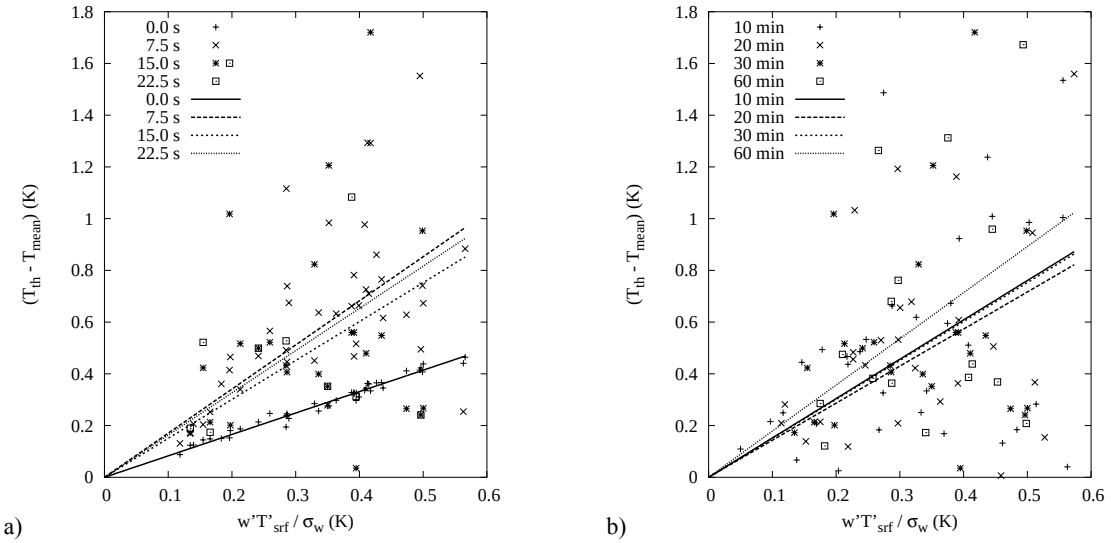

FIGURE 5.47 Same as Figure 5.46, but for criterion #2.

The sensitivity to the criterion parameters τ_c and T_c on the five analyzed days are presented in Figures 5.46 and 5.47, for criterion #1 and #2 respectively. The sensitivity to the chosen criterion variable(s) is subsequently presented in Figure 5.48. The excess factor, which we use as a measure for this sensitivity, can be calculated by using equation (4.16), which leaves us with

$$b_\phi = \frac{\phi_u(z_r) - \overline{\phi}(z_r)}{\overline{w'\phi'}_{srf} / \sigma_w(z_r)} \tag{5.1}$$

that gives us opportunity to make an estimate for b_ϕ by making a linear fit between the term $\overline{w'\phi'}_{srf} / \sigma_w(z_r)$ and the calculated thermal anomaly $\phi_u(z_r) - \overline{\phi}(z_r)$, where z_r denotes the height of the sonic anemometer in this case.

In Figures 5.46a and 5.47a, we notice that the sensitivity of the excess factor to the chosen thermal time scale only substantially differs for $\tau_c = 0.0s$. This time scale in fact implies that all positive anomalies do contribute in the calculated thermal characteristics, they do not have to persist for a certain longer period. Logically, this makes the criterion less strict, what has the consequence that the mean thermal anomalies for temperature and humidity decrease. As the surface fluxes and σ_w do not change, this means that the gradient of the linear fit according to equation (5.1) also decreases. Hence, the stricter the criterion gets (increase of τ_c), the higher the value determined for b_ϕ. For b_q (not shown), we find the same behaviour.

For the averaging period (Figures 5.46b and 5.47b), we observe that it does not really matter what to choose. First of all, we notice that the two criteria do not show the same sequence of derived factors. Above that, the extreme values for derived temperature excess factor are considerably close to each other; for criterion #1 we find a range for b_T of 2.57 ± 0.06 (10 minutes) to 2.89 ± 0.11 (60 minutes). For criterion #2, this range is 1.59 ± 0.20 (20 minutes) to 1.84 ± 0.21 (60 minutes). Again, the spread in b_q does not differ much from that presented in b_T.

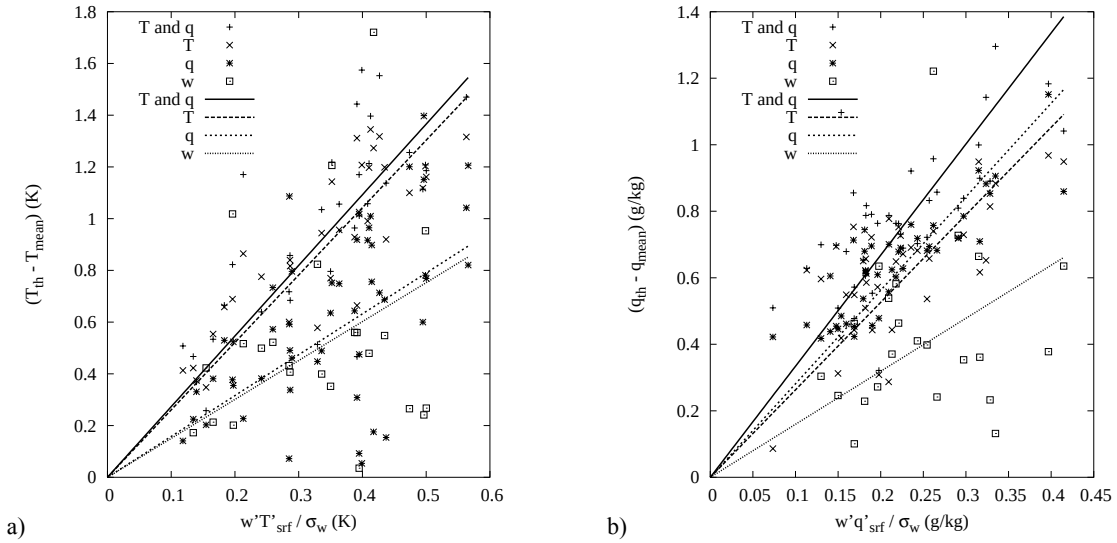

FIGURE 5.48 Sensitivity to chosen criterion variable(s), for 10, 11 and 15 May. Results shown for a) b_T and b) b_q .

The reader can note a striking difference between the values derived for the excess factors by means of criterion #1 and the values found by making use of criterion #2. It is also remarkable that the spread in the points that are linearly fitted in Figures 5.46 and 5.47, is much larger for criterion #2 than for criterion #1. This can be explained by means of the used sampling variable(s).

In Figure 5.48, the sensitivity of b_T and b_q to sampling variable(s) is plotted for four cases, criterion #1 corresponds to sampling on T and q, criterion #2 corresponds to sampling on w. Because we are looking here at mean thermal anomalies for temperature and humidity (on the y-axis), sampling on w logically leads to lower derived values for the excess factors. It is namely dependent on the correlation between vertical velocity and temperature and between vertical velocity and humidity, especially for the longer time scales. For example, when the identification routine detects a data point in a time series with a positive vertical velocity anomaly it is detected as potential thermal and is seen as 'real' thermal data point when the positive anomaly persists for a certain time scale τ_c. The corresponding values for temperature and humidity are automatically taken into account, irrespective of the sign of their anomaly. This causes the so-called indirect sampling of T and q via w, which leads to lower values for the derived mean thermal anomalies of T and q. As we have seen in the discussion about the chosen thermal time scale, this subsequently leads to a lower value for the excess factors. Hence, we here also note: the stricter the criterion, the higher the value for b_ϕ .

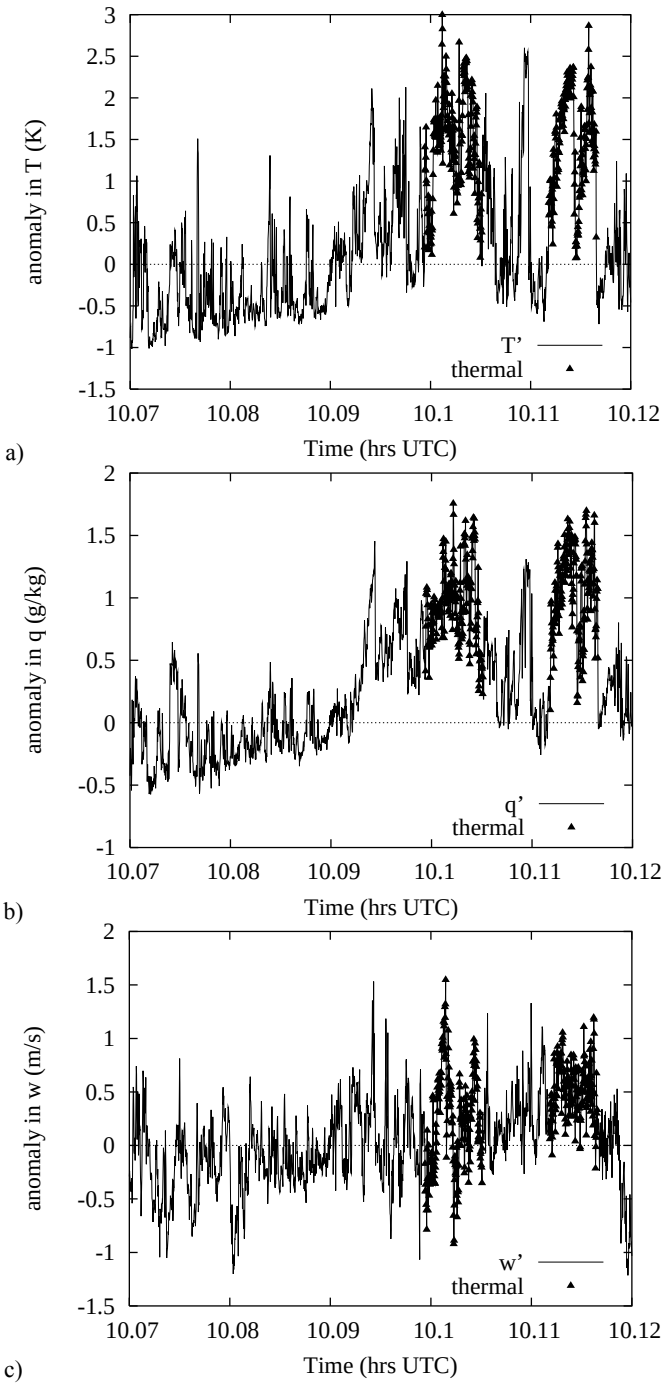

FIGURE 5.49 Example of the thermal sampling procedure for criterion #1 as listed in Table 5.8, for a) temperature, b) humidity and c) vertical velocity. The triangles represent data points that are identified as thermal data points. Negative values of vertical velocity anomaly can occur due to direct sampling on T' and q', considering the criterion used here. Time series are depicted for the interval 10.08 – 10.12 hrs UTC on 10 May, representing an interval of 144 s.

The thermal sampling by means of criterion #1 is illustrated in Figure 5.49. It shows time series for temperature, humidity and vertical velocity for an interval of 144 s in the morning of 10 May. Considering the description of criterion #1, sampling occurs on $T' > 0 \bigcup q' > 0$, which means that

also negative anomalous values for w' are possibly taken into account in the calculation of the mean thermal anomaly for the corresponding averaging period. This leads to lower values for the mean vertical velocity associated with thermals than in the case of sampling on criterion #2. For sampling on the latter, it is the other way around; we then derive lower mean thermal anomalies of temperature and humidity. Typical values for these mean thermal characteristics during the days that have been studied are listed in the next section.

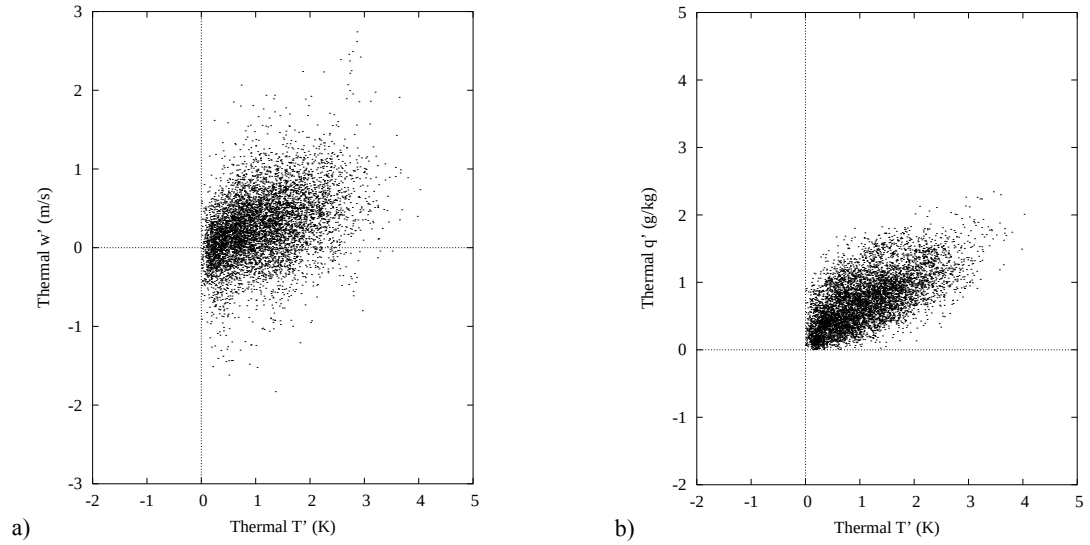

FIGURE 5.50 Scatterplots for 10 May 09:00 – 16:00 UTC, for thermal temperature anomaly T' (K) versus a) thermal vertical velocity anomaly w' (m/s) and b) thermal total specific humidity anomaly q' (g/kg). Results are shown for criterion #1, 6900 of 252000 data points (2.7%) were identified as thermal data points.

Scatterplots that indicate the correlation between the sampling parameters at a glance are presented in Figure 5.50. Results are shown for 10 May, 09:00 – 16:00 UTC. In panel a) we observe once again the effect of indirect sampling; using criterion #1 ($T' > 0 \cup q' > 0$), the mean thermal anomaly for vertical velocity on this day is suppressed by a significant number of thermal data points that have a negative vertical velocity anomaly. In panel b) the direct sampling causes that only points exist in the upper right quadrant of the graph, where as well the anomaly for temperature as for humidity are positive.

For both scatterplots we besides note a positive correlation; for rising values of thermal temperature anomaly T' both w' and q' lapse more or less rising. This is more clearly seen for humidity anomalies than it is seen for vertical velocity anomalies. Considering absolute values for this period, we observe maximum values for T' in the order of 3.5 K, for q' in the order of 0.002 g/g, while w' peaks with fairly high values up to 2.5 m/s.

5.6.4 Overall results

As mentioned before, we will primarily focus on results for the 5 m sonic anemometer level. At the end of this section we will briefly show some results of 13 September, the only day in the analysis on which all Cabauw anemometers were operational.

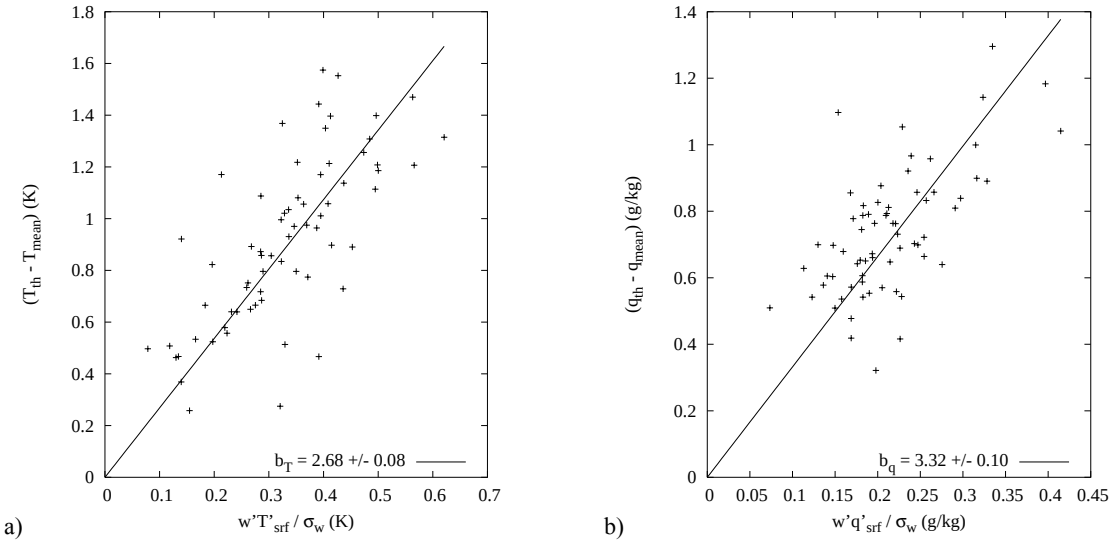

FIGURE 5.51 Excess factors a) b_T and b) b_q determined from criterion #1 sampling on 10, 11, 15 May, 16 August and 13 September, for the 5 m level.

The excess factors b_T and b_q are determined by a linear fit that starts at (0,0) by applying equation (5.1). Average results for 10, 11 and 15 May for both criterion #1 and #2 are shown in Figures 5.51 and 5.52. As these figures tell us, by sampling on temperature and humidity (#1), we obtain $b_T = 2.68 \pm 0.08$ and $b_q = 3.32 \pm 0.10$, while sampling on the vertical velocity criterion (#2) delivers $b_T = 1.51 \pm 0.23$ and $b_q = 1.59 \pm 0.21$.

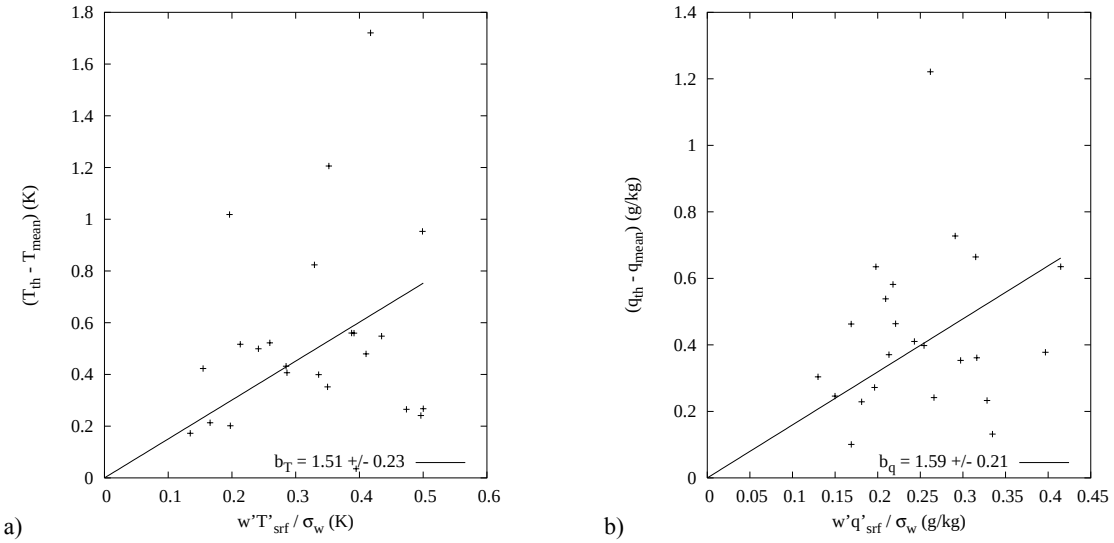

FIGURE 5.52 Same as Figure 5.51, but for criterion #2.

In Table 5.9, the overall results of mean thermal characteristics found with criterion #1 are listed. We note a considerably low anomaly for w that is on average around 0.2 m/s, while calculated anomalies for T and q vary in the range 0.8 – 1.1 K and 0.6 – 0.9 g/kg respectively. For the indirect sampling on criterion #2 (not shown), we find on average that $\langle w' \rangle_{th}$ is 0.5 m/s, while mean anomalies for T (0.5 K) and q (0.4 g/kg) are considerably lower than in the criterion #1 case.

Taking into consideration the number of thermals during the convective period, we distinguish between two quantities in Table 5.9; the fifth column represents the number of thermal data points as percentage of total time, while the sixth column is bound up with the average absolute number of separate thermals that is detected in one averaging period τ_c, that is chosen 30 minutes for both criteria. We observe that on average between 2.7 and 6.9 % of the time consists of thermal data points, for sampling on criterion #1. Next, this implies on average between 2 and 5 thermals per half hour averaging period, irrespective of length and intensity.

Day	$\langle w' \rangle_{th}$ **(m/s)**	$\langle T' \rangle_{th}$ **(K)**	$\langle q' \rangle_{th}$ **(g/kg)**	**thermals % of time**	**thermals 30 min^{-1}**	b_T	b_q
10 May	0.27	1.11	0.74	2.7	2.4	2.67	3.48
11 May	0.25	1.06	0.66	3.5	2.9	2.80	4.11
15 May	0.20	0.74	0.93	6.6	4.5	2.73	3.08
16 Aug	0.16	0.97	0.63	7.1	3.6	2.36	3.00
13 Sep	0.21	0.78	0.70	6.9	4.4	2.95	3.52

TABLE 5.9 Overview of the mean thermal anomalies derived with criterion #1.

Furthermore, we calculated the contribution of the considered thermal coherent structures in the total turbulent fluxes $\overline{w'T'}$ and $\overline{w'q'}$ at 5 metres. For the sampling method that uses $T' > 0 \bigcup q' > 0$ (#1), we find that thermals contribute in 3 – 7 % of total time for 15 – 40 % in fluxes of heat and moisture. For sampling on $w' > 0$ (#2), we observe that the selected thermals occur during 1 – 4 % of total time. During these events, they together contribute for 2 – 25 % in fluxes of heat and moisture. In general we may now conclude that a considerable amount of the turbulent transport of heat and moisture in the surface layer is provided by coherent thermal structures. This has already been investigated in many studies. In 1989, Gao et al. found that thermals might be responsible for up to 75 % of the turbulent fluxes in the surface layer. Later, this was proved to be 40 % on average, see Lu and Fitzjarrald (1994).

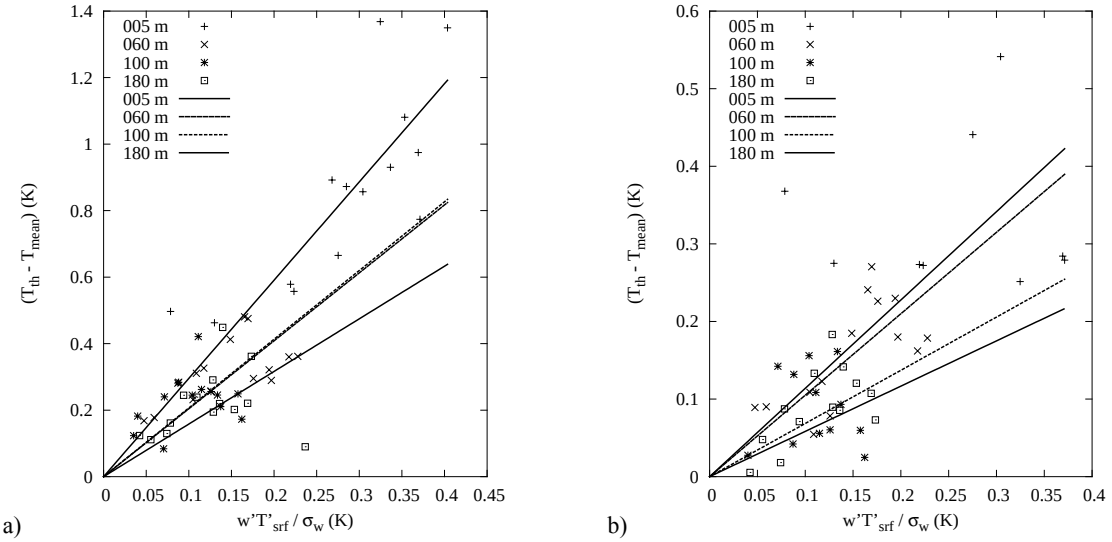

FIGURE 5.53 Excess factors derived for a) criterion #1 and b) criterion #2 for the period 09:00-16:00 on 13 September 2003.

As mentioned earlier, on 13 September all sonic anemometers in Cabauw were operational. Therefore, in Figure 5.53 the linear fits for the determination of b_T at the 5, 60, 100 and 180 m levels on this day are presented, for both criteria. For criterion #1, we find the extremes $b_T = 2.95 \pm 0.17$ (5 m) and $b_T = 1.58 \pm 0.23$ (180 m). For #2, we observe the same sequence of lines, with values between $b_T = 1.14 \pm 0.19$ (5 m) and $b_T = 0.58 \pm 0.13$ (180 m). In subsection 5.6.5 we will try to find an explanation for this phenomenon. Concerning mean thermal anomalies for this day, we find that for criterion #1 (and #2) the mean thermal vertical velocity anomaly $\langle w' \rangle_{th}$ increases from 0.2 m/s (#2: 0.4 m/s) at 5 m to 0.7 m/s (#2: 0.9 m/s) at 180 m, while $\langle T' \rangle_{th}$ and $\langle q' \rangle_{th}$ decrease from 0.8 K (#2: 0.3 K) and 0.7 g/kg (#2: 0.3 g/kg) at 5 m to 0.2 K (#2: 0.1 K) and 0.2 g/kg (#2: 0.1 g/kg) at 180 m, respectively. With increasing height, the thermals thus become stronger rising but less warm and moist with respect to their environment. This can be seen as a conversion from potential (thermal) energy near the surface to kinetic energy that is expressed in a higher vertical velocity at higher levels in the boundary layer.

5.6.5 Discussion

Although the used method and its results in this section seem considerably straightforward, it is not without any discussion.

First of all, for the determination of so-called 'convective periods' for wavelet analysis and thermal sampling, we only looked at the presence of boundary layer clouds during the day and furthermore selected on positive surface buoyancy fluxes. Of course it is possible that in e.g. a 09:00 – 14:00 period there is some time during which convective clouds are not present. We did not make any distinction between these periods and collected all data of these convective periods of the analyzed days together.

The derived thermal time scale for 5 m varies between 18.9 s and 39.1 s. with an average value of 27.1 s. For the thermal sampling we used that the thermal time scale $T_c = 15.0s$, in order to take into account even the smallest thermals detected. Of course, if we apply this time scale of 15.0 s to all data, eddies on smaller scales than the one associated with the location of the maximum in the global wavelet spectrum are also taken into account as contributors. This should be omitted, otherwise the added value of the performed wavelet analysis in subsection 5.6.2 becomes marginal. In fact, for every half hour the derived time scale should be applied to the thermal sampling procedure of the corresponding data sets.

The excess factors we derived are valid for temperature and (water vapor) specific humidity. In 1D SPAM the excess factors are associated with liquid water potential temperature and total specific humidity. Because we perform our analysis close to the surface, we can assume that $q_l \sim 0$ and $p \sim p_{ref}$, such that $\theta_l \simeq T$ and $q_t \simeq q_v$.

Furthermore, there is a 5 m difference between the release height in the 1D SPAM REF run (i.e. 10 m) and the level at which we analyze the sonic data sets (i.e. 5 m). In subsection 5.6.4 we have seen that this approach is not insensitive to height, which means that the mean thermal anomalies and hence the derived excess factors might differ for the two mentioned levels. This is caused by an increasing value for σ_w in this region, while the surface flux is fixed and the excess $\phi_u - \overline{\phi}$

decreases. If we now take a look at equation (5.1), we see that the two changing terms counteract each other to some extent. Subsequently, Figure 5.53 tells us that the excess factor decreases with height for both criteria, which means that the decrease of the excess prevails with its contribution. We might thus expect somewhat lower values for the derived excess factors if we would have been able to analyze 10 m sonic anemometer data, but we can not make an estimate of the absolute decrease that is incorporated with this correction.

The sensitivity of b_ϕ to height is a fairly unpleasant property. The whole idea of scaling the parcel excess with a ratio that is dependent on the surface flux and the vertical velocity standard deviation is based on a certain unified description for all model levels, i.e. it should be independent on release height. Soares et al. (2004) solved this problem by a similar scaling, but with the square root of the turbulent kinetic energy (TKE) instead of with σ_w. The TKE is defined as $e = u^2 + v^2 + w^2$, where u, v and w denote the zonal, meridional and vertical components of the wind vector, respectively. By making a linear fit for the derivation of b_ϕ, in the same way as we did in subsection 5.6.3, they found a height-independent $b_\phi \simeq 0.3$ for $\phi = \theta_v$.

6 Conclusions and Recommendations

6.1 Introduction

The study of which the experimental setup and results have been presented to the reader in the first five chapters, in fact contains two distinct parts; first of all there was the setup, execution and evaluation of the offline model that was developed, 1D SPAM. Together with the sensitivity studies that were carried out, it forms the first major part. Next, the thermal identification method and its results, that consist of wavelet analysis and thermal sampling, is the second distinct part of the study. Of course, the two parts are connected to each other via the new trigger function that is tested. It consists of new ideas that assume that the turbulent transport in the boundary layer is mainly caused by strong narrow updrafts that we can describe as an ensemble of thermals, with their roots at the surface. Therefore, making an estimate of the mean thermodynamic properties of these thermals and determination of the excess factors, which are essential parameters in the new formulation of the trigger function, is inevitable. In this chapter, we will present the drawn conclusions for each part separately and make some recommendations for possible further research.

6.2 Conclusions

Case studies

Undiluted ascents in general predict too many shallow convective clouds. The presence of these clouds is better described with a new 'unified' formulation for the trigger function (Jakob and Siebesma, 2003), considering the studied BBC2 cases on 10 and 11 May 2003. This new formulation is e.g. based on the idea of sub-cloud lateral mixing and enhanced parcel properties that are given at the parcel release height. The mixing induces that not all parcels are able to penetrate through the negatively buoyant area and become clouds, which is the main reason for a suppressed cloud presence. The values and shapes of the vertical profiles of updraft thermodynamic properties show considerably good agreement with typical shallow cumulus cases, at a glance.

Cloud boundaries are also fairly well positioned. Cloud base is somewhat altered due to the new formulation, cloud tops seem to be overestimated in multiple-layer situations (e.g. on 11 May).

Evaluation with aircraft observations

The modeled profiles of virtual potential temperature, liquid water content and vertical velocity agree well with aircraft observations that were sampled in a 0.5^o x 0.5^o grid box around Cabauw. Especially the maximum observed values of liquid water content and vertical velocity are corresponding to the modeled values. This is more or less consistent with the original idea behind the setup of the trigger function, i.e. its parameters are tuned by LES results of the 1 – 5% of strongest updrafts (Siebesma and Teixeira, 2000). Concerning the virtual potential temperature profile, distinction between cloudy ($q_l > 0$) and mean ($q_l = 0$) profiles is even recognized.

Sensitivity studies

Four sensitivity studies are performed in order to detect possible connections between changes in model parameters and the resulting outcome, in the form of cloud presence, cloud base and top and in-cloud thermodynamic properties.

Generally, dilution causes the cloud base to rise. The simulated values get closer to the observations by lidar, but a spread is seen among the studied days. Considering the different fractional entrainment rate formulations that were tested, it is shown that sub-cloud dilution causes cloud convective properties to become less sensitive to parcel release height and release excesses. Nevertheless, the vertical velocity dependency of ε causes a certain sensitivity to parcel release height and release excesses. This dependency on w_u is part of the twofold formulation, proposed by Neggers (2002) and Cheinet (2003). The $1/z$ formulation does not have this unpleasant property, but such a formulation has the disadvantage that fractional entrainment rate is underestimated e.g. near the inversion of the moist boundary layer. Concerning the sensitivity to release excess factors, it is especially the factor for liquid water potential temperature, b_{θ_l}, that influences the cloud convective properties through the huge sub-cloud gaining of CAPE. This is associated with higher vertical velocities, which on their turn temper ε.

Initialization with RS90 delivers us the same relative behaviour in the entrainment formulation sensitivity study, only the absolute values that are generated differ substantially from the values found with the combined mast/IPT input profiles. Fortunately, this does not have any impact on the sensitivity itself.

Thermal identification

Coherent structures along the Cabauw mast are identified with help of high-frequent measurements from sonic anemometers. Wavelet analysis is used to determine prevailing time scales, whereafter the characteristics of thermals during typical convective conditions are studied. For the 5 m level in Cabauw, we find dominant time scales that agree well with values found in Krusche and de Oliveira (2004), i.e. 18.9 – 39.1 s. This dominant time scale grows with height, as well as the uncertainty in it. The feedback of this part of the project on the offline model lies in the excess factors for temperature and humidity that can be derived from these mean thermal properties. We find excess factors $b_T = 2.68 \pm 0.08$ and $b_q = 3.32 \pm 0.10$ for sampling on simultaneous positive temperature and humidity anomalies, while sampling on positive anomalies in vertical velocity delivers $b_T = 1.51 \pm 0.23$ and $b_q = 1.59 \pm 0.21$. The latter is better in agreement with the value for b_ϕ from LES results: $b_\phi = 1.5$.

The derived excess factors are only substantially sensitive to sampling variable(s), in contrast with the chosen averaging period or thermal time scale. We observe that the values derived for excess factors become higher for stricter sampling methods.

Finally, we studied the contribution of thermals to total turbulent fluxes in the surface layer. We here find that thermals contribute in 3 – 7 % (1 – 4 %) of total time for 15 – 40 % (2 – 25 %) in fluxes of heat and moisture, for sampling with the criterion $T' > 0 \cup q' > 0$ ($w' > 0$).This high contribution is fairly consistent with earlier experiments. Results are based on measurements carried out by the Cabauw sonic anemometer at 5 m, during five BBC2 and non-BBC2 days.

Other

It should be stressed that discrepancies in the input profiles have a substantial impact on the modeled cloud convective properties in 1D SPAM. The correction procedure that has been carried

out for a successful fitting of mast and IPT profiles already indicates that significant biases may be expected in the IPT vertical profiles of temperature and humidity. Together with the absolute differences that were found for RS90 input profiles during one of the sensitivity tests, it is very difficult to make an estimate of the quality of SPAM-simulated cloud convective properties.

We have not taken into account the effect of wind shear on entrainment. Brown (1999) investigated this phenomenon and found that the transport of heat and moisture in the boundary layer is – in contrast with the transport of momentum – to a large extent unaffected by wind shear.

6.3 Recommendations

Because we have only taken a few arbitrary cases into consideration here, it is first of all important to test the new formulation of the trigger function by making use of typical trade-wind cumulus cases, like BOMEX. Furthermore, the chosen BBC2 Golden Days should be extensively run in the 1D and 3D versions of KNMI's regional climate model RACMO.

The set of entrainment formulations tested in this study does not contain a formulation of the form $c_\varepsilon[1/z + 1/(z - z_i)]$. It has been shown in LES studies (Siebesma et al., 2004; Soares et al., 2004) that this parameterization for ε works considerably well for the dry and moist convective boundary layer. It solves the problem of the underestimation of ε near the inversion, while independency to release properties is also more or less guaranteed. A disadvantage of it is that it is dependent on the inversion height z_i which makes it necessary to make an estimate of this parameter, e.g. by using information from previous time steps.

Concerning the measurements, it would be extremely useful for studies as this to have the disposal of high quality vertical profiles of temperature and humidity. For parcel release reasons, the profiles in the surface layer should be as good as those in other parts of the atmosphere. Unfortunately, until now the Integrated Profiling Technique (IPT) operates on a resolution of 250 m, which made it necessary to combine the IPT measurements with mast measurements. Therefore, Cabauw mast observations should be taken into account in the list of observations that goes into the IPT Bayesian retrieval. This has already been discussed and approved during the BBC2 Workshop in De Bilt, on 18 and 19 October 2004.

Cloud top measurements are indispensable for a good validation of cloud boundary output. In this study, we indirectly estimated cloud tops from radar-lidar retrieval of cloud liquid water in the Cloudnet database.

Aircraft measurements might be used to make estimates of updraft mass-flux in cumulus clouds, by a conditional sampling of data points that contain liquid water. Next to this, one will need an estimate or measurement of cumulus cloud cover. This may give more insight in the in-cloud profile of mass-flux, which is still an unsolved problem.

For the thermal identification, it is important to build up more statistics. If a distinction is made between cloud and cloud-free periods during the analyzed convective periods, we might get better values for the mean thermal characteristics because they are filtered for the periods you do not want

to take into account. Finally, it would be useful to sample every averaging period on its corresponding thermal time scale.

6.4 Acknowledgements

This is an expression of thanks to everyone who supported and helped me in achieving the results described in this report. I would like to mention some people in particular.

First of all, I would like to thank my first supervisor Pier Siebesma (KNMI) for his guidance and advice during the project period from December 2003 to January 2005. I am very grateful to Pier, who always was immensely enthousiastic and full of interest in the frequent (and sometimes not so frequent...) meetings we had.

I also would like to thank Fred Bosveld and Henk Klein Baltink (KNMI), who kindly provided me with measurements from the Mobibase database and BBC database, respectively. They also gave me support on the interpretation of these measurements. RACMO output, which is unfortunately not incorporated in this study, has been provided by Erik van Meijgaard (KNMI). I would like to thank my second supervisor, Aarnout van Delden (IMAU), for the guidance and useful comments concerning the preparation for the presentation I had to give at Utrecht University.

Subsequently, a word of thanks to: Eddy Moors (Alterra Wageningen), Cindy Werner (National Science Fundation, USA), Harm Jonker (TU Delft), Bruno Piguet (Meteo France), Chris Torrence (Research Systems Inc., USA), Manfred Wendisch and Sebastian Schmidt (IfT Leipzig, Germany) and Nisia Krusche (Federal University of Rio Grande, Brasil).

I would like to thank the people at the Atmospheric Research (AO) department of KNMI for giving me a nice year with joyful discussions and laughs during lunches and coffee breaks. They gave me the feeling of being a real employee instead of ‘just a student’. It was a very pleasant time.

Last, but not least, I would like to thank Marieke, my family and friends for supporting me. I am very grateful for your interest and patience during the last year of intensive work.

Marijn de Haij
De Bilt, January 2005

Appendix A – Basic thermodynamics of moist air

A.1 Introduction

In this appendix, the reader will be made familiar with some essential concepts in the thermodynamics of moist air. The appendix forms a good preparation for the theory that is presented in chapter 2. For more details we refer to Iribarne and Godson (1973).

In general, the atmospheric boundary layer consists of a considerable amount of moisture in vaporized form, while on top of a cloud-topped boundary layer a phase change to liquid water occurs as well. Hence, phase changes and latent heat release that coincides with it play a very important role and should therefore be described accurately.

We will start with the equation of state and the laws of thermodynamics, which form the basics of this appendix. Furthermore, we will discuss the used moisture and temperature variables and explain why they are so useful.

A.2 Basic principles

Atmospheric air is a mixture of various gases, and appears in different phases. Take into consideration an isothermal air parcel that consists of a mass of dry air m_d, a water vapor mass m_v and a liquid water mass m_l. The density ρ of the air parcel that has a total mass m, volume V and temperature T, can be split up in the partial densities

$$\rho = \frac{m}{V} = \rho_d + \rho_v + \rho_l \tag{A.1}$$

where the subscripts d, v and l denote the properties of dry air, water vapor and liquid water, respectively. We hereby made use of the relation $m = m_d + m_v + m_l$.

Equation of state

The equation of state for an ideal gas reads as (e.g. Iribarne and Godson, 1973):

$$pV = nRT \tag{A.2}$$

with p the pressure, n the number of moles of the gas and $R = 8.314 Jmol^{-1}K^{-1}$ the universal gas constant. We can make life much easier when we substitute $n/V = \rho$, which leaves us with a consideration solely in kilograms. Of course, in that case we also have to adapt the gas constant.

If we write equation (A.2) down for the dry air and water vapor part from relation (A.1), we obtain $p_d = \rho_d R_d T$ and $p_v = \rho_v R_v T$. Hereby the gas constants for dry air and water vapor are introduced, they have values $R_d = 287.05 Jkg^{-1}K^{-1}$ and $R_v = 461.50 Jkg^{-1}K^{-1}$. If we now add the partial pressures of dry and moist air by making use of Dalton's law (Iribarne and Godson, 1973), the total pressure of the parcel is delivered as

$$p = \rho R_d T \left[1 + (\frac{1}{\varepsilon_0} - 1)\frac{\rho_v}{\rho} - \frac{\rho_l}{\rho} \right] \tag{A.3}$$

where $\varepsilon_0 = R_d / R_v \simeq 0.622$.

Moisture variables

Equation (A.3) in fact requires the use the *specific humidity for water vapor* q_v and the *liquid water content* q_l . These moisture variables are mixing ratios that indicate what mass of moisture in a certain form is present per mass of air. The definitions logically follow:

$$q_v = \frac{\rho_v}{\rho} \tag{A.4}$$

$$q_l = \frac{\rho_l}{\rho} \tag{A.5}$$

If we leave precipitation and the forming of ice out of consideration, the only sources and sinks that can lead to conversion between the moisture variables q_v and q_l are present in the form of condensation effects. If we want to introduce a moisture variable that is conserved under condensation processes, we obtain the *total specific humidity* q_t :

$$q_t = q_v + q_l \tag{A.6}$$

This quantity is essential in studying turbulent mixing processes, because it exactly determines the amount of moisture that has been subjected to mixing, in the absence of the external sources and sinks.

The maximum amount of water vapor that an air parcel can contain is expressed in the *saturation specific humidity* q_s . If q_v exceeds this value, conversion of water vapor into liquid water will take place. The saturation specific humidity is described in the relationship

$$q_s = \frac{\varepsilon_o e_s}{p + e_s(\varepsilon_0 - 1)} \tag{A.7}$$

where e_s is the saturation vapor pressure, defined as $\rho_s R_v T$. This variable can be derived from an integration of the Clausius-Clapeyron equation (Iribarne and Godson, 1973). Subsequently, we integrate the result and find for e_s

$$e_s(T_l) = e_0 \exp[a\frac{(T_l - T_0)}{(T_l - b)}] \tag{A.8}$$

with $e_0 = 610.78Pa$, $T_0 = 273.16K$ as the temperature at the triple point, $a = 17.27$ and $b = 35.86$.

We conclude from equations (A.7) and (A.8) that the saturation specific humidity is a function of solely pressure and temperature, i.e. $q_s = f(p,T)$. More details about condensation effects can be found in section 2.5.

Laws of thermodynamics

Combining the first two laws of thermodynamics (not shown here, see e.g. Iribarne and Godson, 1973), we obtain for the *specific entropy* s^* of an air parcel (Siebesma, 1998):

$$ds^* = c_{pm} d\ln T + R_m d\ln p - \frac{L}{T} dq_l \tag{A.9}$$

In this equation, the subscript m stands for parcel mean values, i.e. consisting of a dry and moist part. We first simplify it by using $c_{pm} \sim c_p$ for the specific heat capacity and $R_m \sim R_d$ for the gas constant. The last term in (A.9) is associated with condensation effects, this vanishes in the absence of liquid water. The first two terms describe the change in entropy caused by a change in parcel temperature or pressure, respectively.

Temperature variables

When we consider the adiabatic displacement (i.e. no heat is inserted in or extracted from the system, $ds^* = 0$) of a dry air parcel in the atmosphere, its temperature T will be subjected to expansion or compression, dependent on the direction of motion (upward or downward, respectively). This will cause the temperature to decrease in the case of expansion, while compression causes an increase of temperature. This gives reason to introduce a temperature that is conserved under dry-adiabatic displacements and hence corrects for the cooling or warming due to adiabatic pressure change. Using equation (A.9) and substituting $ds^* = c_p d\ln\theta$ in the absence of the condensation term, integration from a reference state p_0 delivers:

$$\theta = T\left(\frac{p_0}{p}\right)^{R_d/c_p} \equiv T/\Pi \tag{A.10}$$

The *potential temperature* θ is defined as the temperature that a parcel would have if it was brought adiabatically from pressure p to a given reference pressure p_0, which is usually chosen $10^5\,Pa$. The Exner function is denoted by $\Pi = (p/p_0)^{R_d/c_p}$, with $R_d/c_p \simeq 0.286$.

The introduction of the potential temperature is very useful, because heating and cooling effects induced by diabatic processes in the atmosphere can be recognized much easier than considering the 'normal' air temperature.

Up till now, we have considered dry air parcels, while in reality completely dry situations do not occur in the atmosphere. Water vapor lowers the density of air, while liquid water makes air denser. It would be favourable to construct a temperature that corrects for this density effect of humidity. The *virtual temperature* T_v is defined as the temperature a parcel would have if all the moisture in it would be removed:

$$T_v = T(1 + 0.61 q_v - q_l) \tag{A.11}$$

It can be obtained by writing equation (A.3) in the form of the equation of state $p = \rho RT$. A nice property of this temperature variable is that it is inversely proportional to the density of air. The virtual temperature is therefore very convenient in considering e.g. the buoyancy of air parcels, which is determined by the difference in density between the parcel and its environment.

If liquid water is formed because the water vapor specific humidity q_v of a parcel exceeds the saturation specific humidity value q_s, the condensation of water vapor causes a latent heat release that on its turn increases the temperature of the parcel. The correction for this effect can be achieved by introducing the *liquid water temperature* T_l. It is defined as the temperature a parcel would have if all the liquid water in it would be removed (by means of evaporation):

$$T_l = T \exp\left(-\frac{L q_l}{c_p T} \right) \tag{A.12}$$

where $L = 2.5 \times 10^6 J/kg$ is the specific latent heat release of the phase change from water vapor to liquid water. Equation (A.12) can be derived from (A.9), if the substitution $ds^* = c_p d \ln T_l$ is made, this time in absence of the second term.

Fortunately, we can simplify this equation by using that q_l is very small in clouds (in the order of 10^{-3}), which causes the term in the exponent to be much smaller than 1. This gives us opportunity to make a Taylor expansion and derive a linearized version of T_l (e.g. Siebesma, 1998):

$$T_l \approx T - \frac{L}{c_p} q_l \tag{A.13}$$

For $q_l = 0$, this relation reduces to $T_l = T$.

In most studies, combinations of (A.11) and (A.10) or (A.12) and (A.10) are used. The result is the introduction of the so-called *virtual potential temperature* θ_v:

$$\theta_v = \theta(1 + 0.61 q_v - q_l) \tag{A.14}$$

and the *liquid water potential temperature* θ_l:

$$\theta_l = \theta - \frac{L}{c_p \Pi} q_l \tag{A.15}$$

Together with the earlier mentioned total specific humidity, θ_l is extremely useful in the application of turbulent mixing studies, because it is conserved under adiabatic pressure changes as well as under adiabatic phase changes.

Appendix B – Pictures

B.1 Introduction

Meteorology is for the general public inextricably bound up with beautiful photographs of cloudy skies, extreme weather events and other interesting phenomena. Especially in a paper about so-called fair-weather cumulus, illustrating pictures are indispensable. Therefore, in this appendix the reader can find some of the various cloud types and of instruments that have provided measurements for this study.

B.2 Cloud types

Cumuliform clouds

FIGURE B.2.1 Shallow cumulus clouds above the Westerschelde, The Netherlands.

FIGURE B.2.2 Altocumulus.

FIGURE B.2.3 Anvil-shaped cumulonimbus cloud.

FIGURE B.2.4 Stratocumulus fields above Honolulu, Hawaii, USA.

Stratiform clouds

FIGURE B.2.5 Stratus layer.

FIGURE B.2.6 Altostratus above McMinnvile, Oregon, USA.

Cirriform clouds

FIGURE B.2.7 Cirrus.

FIGURE B.2.8 Cirrostratus above Mont Saint Michel, France.

FIGURE B.2.9 Cirrocumulus.

B.3 Instruments

FIGURE B.3.1 213 m high Cabauw meteorological mast.

FIGURE B.3.2 Low profile mast, located next to the Cabauw main mast.

FIGURE B.3.3 The Cabauw remote sensing site in July 2004, as seen from the upper level of the main mast.

FIGURE B.3.4 Temperature and humidity sensor mounted on a boom in the Cabauw mast.

FIGURE B.3.5 Wind vane and cup anemometer in the Cabauw mast.

FIGURE B.3.6 Sonic anemometer installed by Alterra at the 100 m level of the mast.

FIGURE B.3.7 Launch of a RS90 sonde during the BBC1 campaign.

FIGURE B.3.8 Vaisala CT75K lidar ceilometer at the Cabauw site.

FIGURE B.3.9 Low-cost HATPRO radiometer, used in the Integrated Profiling Technique.

FIGURE B.3.10 Merlin IV research aircraft, owned by Meteo France, Toulouse.

List of Symbols

α_{Xc}		Treshold fraction for quantity X		
a		Constant	17.27	
a_u		Fractional updraft area		
A		Area		$[\,km^2\,]$
b		Constant	35.86	
b_ϕ		Excess correlation coefficient		
b_w		Proportionality factor for entrainment of w		
c		Speed of propagation of sound waves		$[\,ms^{-1}\,]$
c_1		Constant		
c_2		Constant		
c_ε		Fractional entrainment constant		
c_p		Specific heat capacity for dry air at constant pressure	1004	$[\,Jkg^{-1}K^{-1}\,]$
$CAPE$		Convective available potential energy		$[\,m^2s^{-2}\,]$
δz		Infinitesimal vertical displacement		$[\,m\,]$
d		Anemometer path length		$[\,m\,]$
dd		Wind direction		$[\,^\circ\,]$
D		Detrainment rate		
ε		Fractional entrainment rate		$[\,m^{-1}\,]$
ε_w		Fractional entrainment rate for w		$[\,m^{-1}\,]$
ε_0		R_d / R_v	0.622	
e		Turbulent kinetic energy		$[\,m^2s^{-2}\,]$
e_s		Saturation water vapor pressure		$[\,Pa\,]$
e_0		Constant	610.78	$[\,Pa\,]$
E		Entrainment rate		
η		Non-dimensional wavelet time parameter		
ϕ		Moist-adiabatic conserved property, $\{\theta_l, q_t\}$		$[\,K, gkg^{-1}\,]$
f_{kar}		Von Karman constant	0.4	
ff		Absolute horizontal wind speed, $(u^2+v^2)^{1/2}$		$[\,ms^{-1}\,]$
F_B		Buoyancy force		$[\,kgms^{-2}\,]$
F_p		Pressure perturbation forcing		$[\,kgms^{-2}\,]$
γ		Proportionality factor		
γ_h		Specific heat ratio	1.4	
Γ		Lapse rate of virtual potential temperature		$[\,Km^{-1}\,]$
	Γ_d	Dry adiabatic Γ	0	$[\,Km^{-1}\,]$
	Γ_m	Moist adiabatic Γ		$[\,Km^{-1}\,]$
g		Gravitational constant		$[\,ms^{-2}\,]$
h		Moist-adiabatic energy		$[\,m^2s^{-2}\,]$
H		Column height		$[\,m\,]$
λ		Turbulent mixing length scale		$[\,m\,]$
L		Specific latent heat release of phase change	2.5×10^6	$[\,Jkg^{-1}\,]$

		from water vapor to liquid water		
L_c		Thermal structure length scale		$[\,m\,]$
L_{MO}		Monin-Obukhov length scale		$[\,m\,]$
N		Number of data points in an averaging period		
Π		Exner function		
p		Atmospheric pressure		$[\,Pa\,]$
p_0		Reference atmospheric surface pressure	10^5	$[\,Pa\,]$
p_{srf}		Atmospheric surface pressure		$[\,Pa\,]$
q		Specific humidity		$[\,g/g\,]$
	q_l	Liquid water specific humidity		$[\,g/g\,]$
	q_s	Saturation specific humidity		$[\,g/g\,]$
	q_t	Total specific humidity		$[\,g/g\,]$
	q_v	Water vapor specific humidity		$[\,g/g\,]$
ρ		Atmospheric density		$[\,kgm^{-3}\,]$
RH		Relative humidity		$[\,\%\,]$
R_d		Gas constant for dry air	287.05	$[\,Jkg^{-1}K^{-1}\,]$
R_v		Gas constant for moist air	461.50	$[\,Jkg^{-1}K^{-1}\,]$
σ_X		Standard deviation of variable X		
s		Wavelet scale		
S		Source or sink		
θ		Potential temperature		$[\,K\,]$
	θ_l	Liquid water potential temperature		$[\,K\,]$
	θ_v	Virtual potential temperature		$[\,K\,]$
τ		Variance dissipation time		$[\,s\,]$
τ_*		Eddy turnover time		$[\,s\,]$
τ_i		Integration time		$[\,s\,]$
τ_c		Averaging period		$[\,s\,]$
t		Time		$[\,s\,]$
T		Temperature		$[\,K\,]$
	T_l	Liquid water temperature		$[\,K\,]$
	T_v	Virtual temperature		$[\,K\,]$
T_0		Temperature at triple point		$[\,K\,]$
u		Zonal wind speed		$[\,ms^{-1}\,]$
u_*		Surface friction velocity		$[\,ms^{-1}\,]$
v		Meridional wind speed		$[\,ms^{-1}\,]$
w		Vertical wind speed		$[\,ms^{-1}\,]$
W		Wavelet function		
$\overline{X}$		Grid box averaged value of variable X		
$\langle X \rangle$		Time-averaged value of variable X		
X_e		Environmental value of variable X		
X_f		Full level value of variable X		
X_h		Half level value of variable X		
X_u		Updraft value of variable X		

ψ_0	Mother wavelet function	
ω_0	Non-dimensional wavelet frequency parameter	
z	Height	$[\,m\,]$
z_i	Inversion height	$[\,m\,]$
z_r	Parcel release height	$[\,m\,]$
z_{LCL}	Height of LCL	$[\,m\,]$
z_{LFC}	Height of LFC	$[\,m\,]$
z_{LNB}	Height of LNB	$[\,m\,]$
z_{LZB}	Height of LZB	$[\,m\,]$

List of Abbreviations

1D	one-dimensional
2D	two-dimensional
3D	three-dimensional
ABL	Atmospheric Boundary Layer
AWS	Automatic Weather Stations
BALTEX	Baltic Sea Experiment
BBC	Baltex Bridge Campaign
BBC1	1st Baltex Bridge Campaign
BBC2	2nd Baltex Bridge Campaign
CAPE	Convective Available Potential Energy
Cu	Cumulus
CESAR	Cabauw Experimental Site for Atmospheric Research
CNRM	Centre National de Recherches Meteorologiques
CRM	Cloud Resolving Model
CTBL	Cumulus-topped Boundary Layer
DIRAM	Directional Radiance Distribution Measurement
DOG	Derivative Of a Gaussian
ECMWF	European Centre for Medium-Range Weather Forecasts
GCM	General Circulation Model
GEWEX	Global Energy and Water Cycle Experiment
HATPRO	Humidity And Temperature Profiler
HIRLAM	High Resolution Limited Area Model
IfT	Institute for Tropospheric Research
IMAU	Institute for Marine and Atmospheric research Utrecht
IPT	Integrated Profiling Technique
ISCCP	International Satellite Cloud Climatology Project
ITCZ	Intertropical Convergence Zone
KNMI	Royal Dutch Meteorological Institute
LCL	Lifting Condensation Level
LES	Large Eddy Simulation
LFC	Level of Free Convection
LHF	Latent Heat Flux
lidar	Light Detection And Ranging
LNB	Level of Neutral Buoyancy
LS	large scale
LZB	Level of Zero Buoyancy
l.h.s.	left hand side
MICCY	Microwave Radiometer for Cloud Cartography
MIRACLE	Microwave Radar for Cloud Layer Exploration
MSc	Master of Science

NERC	National Environment Research Council
NWP	Numerical Weather Prediction
PBL	Planetary Boundary Layer
RACMO	Regional Atmospheric Climate Model
radar	Radio Detection And Ranging
RASS	Radio Acoustic Sounding System
REF	Reference Run
RIVM	National Institute for Public Health and the Environment
r.h.s.	right hand side
SCM	Single Column Model
Sc	Stratocumulus
ShCu	Shallow Cumulus
SHF	Sensible Heat Flux
SIAM	Sensor Intelligent Adaptation Module
SPAM	Single Parcel Ascent Model
TKE	Turbulent Kinetic Energy
UMF	Updraft Mass-flux
UND	Undiluted Run
USA-NSF	USA-National Science Foundation
UTC	Coordinated Universal Time
WCRP	World Climate Research Programme

List of Figures

Bibliography

Betts, A.K., 1973: Non-precipitating cumulus convection and its parameterization. *Quart. J. Roy. Meteor. Soc.*, **99**, 178-196.

Betts, A.K., 1986: New convective adjustment scheme, Pt. 1, Observational and theoretical basis. *Quart. J. Roy. Meteor. Soc.*, **112**, 677-691.

Bougeault, P., 1981: Modeling the trade-wind cumulus boundary layer. Part 1: Testing ensemble cloud relations against numerical data. *J. Atmos. Sci.*, **38**, 2414-2428.

Bretherton, C.S., J.R. McCaa, and H. Grenier, 2004: A New Parameterization for Shallow Cumulus Convection and Its Application to Marine Subtropical Cloud-Topped Boundary Layers. Part I: Description and 1D Results. *Mon. Wea. Rev.*, **132**, 864-882.

Brown, A.R., 1999: Large-Eddy Simulation and Parameterization of the Effects of Shear on Shallow Cumulus Convection. *Boundary-Layer Meteorol.*, **91**, 65-80.

Cheinet, S., 2003: A Multiple Mass-Flux Parameterization for the Surface-Generated Convection. Part I: Dry Plumes. *J. Atmos. Sci.*, **60**, 2313-2327.

Cheinet, S., 2004: A Multiple Mass-Flux Parameterization for the Surface-Generated Convection. Part II: Cloudy Cores. *J. Atmos. Sci.*, **61**, 1093-1113.

Chen, H., and F. Hu, 2003: Coherent Structures Detected in Atmospheric Boundary-layer Turbulence using Wavelet transforms at Huaihe River Basin, China. *Boundary-Layer Meteorol.*, **107**, 429-444.

Chen, H., J. Chen, F. Hu, and Q. Zeng, 2003: The Coherent Structure of Water Vapor Transfer in the Unstable Atmospheric Surface Layer. *Boundary-Layer Meteorol.*, **111**, 543-552.

Collineau, S. And Y. Brunet, 1993: Detection of Turbulent Coherent Motion in a Forest Canopy, Part I: Wavelet Analysis. *Boundary-Layer Meteorol.*, **65**, 357-379.

Cuijpers, J.W.M., 1994: Large-Eddy Simulation of Cumulus Convection. PhD Thesis, Technische Universiteit Delft, Delft.

De Roode, S.R., P.G Duynkerke and A.P. Siebesma, 2000: Analogies between mass-flux and Reynolds-averaged equations. *J. Atmos. Sci.*, **57**, 1585-1598.

Dop, Van H., 2001: Turbulentieleer. IMAU college reader, Universiteit Utrecht, Utrecht.

Dop, Van H., 2002: Grenslaagmeteorologie. IMAU college reader, Universiteit Utrecht, Utrecht.

Farge, M., 1992: Wavelet transforms and their applications to turbulence. *Annu. Rev. Fluid Mech.*, **24**, 395-457.

Gamage, N., and W. Blumen, 1993: Comparative analysis of low-level cold fronts: Wavelet, Fourier and empirical orthogonal function decompositions. *Mon. Wea. Rev.*, **121**, 2867-2878.

Gao, W., R.H. Shaw, and K.W. Paw U, 1989: Observation of Organized Structure in Turbulent Flow within and above a Forest Canopy. *Boundary-Layer Meteorol.*, **59**, 35-57.

Gu, D., and S.G.H. Philander, 1995: Secular changes of annual and interannual variability in the Tropics during the past century. *J. Climate*, **8**, 864-876.

Holtslag, A.A.M., and B.A. Boville, 1992: Local Versus Nonlocal Boundary-Layer Diffusion in a Global Climate Model. *J. Climate*, **6**, 1825-1842.

Iribarne, J.V., and W.L. Godson, 1973: Atmospheric Thermodynamics. Kluwer Academic Publishers, Dordrecht, 259 p.

Jakob, C., and A.P. Siebesma, 2003: A new subcloud model for mass-flux convection schemes; Influence on triggering, updraught properties, and model climate. *Mon. Wea. Rev.*, **131**, 2765-2778.

Krusche, N., and A.P. de Oliveira, 2004: Characterization of Coherent Structures in the Atmospheric Surface Layer. *Boundary-Layer Meteorol.*, **110**, 191-211.

Lenschow, D.H., and P.L. Stephens, 1980: The Role of Thermals in the Convective Boundary Layer. *Boundary-Layer Meteorol.*, **19**, 509-532.

Löhnert, U., S. Crewell, and C. Simmer, 2004: An integrated approach toward retrieving physically consistent profiles of temperature, humidity and cloud liquid water. *J. App. Meteor.*, accepted.

Lu, C.-H., and D.R. Fitzjarrald, 1994: Seasonal and Diurnal Variations of Coherent Structures over a Deciduous Forest. *Boundary-Layer Meteorol.*, **69**, 43-69.

Meyers, S.D., B.G. Kelly, and J.J. O'Brien, 1993: An introduction to wavelet analysis in oceanography and meteorology: With application to Yanai waves. *Mon. Wea. Rev.*, **121**, 2858-2866.

Murray, F.W., 1967: On the computation of saturation vapour pressure. *J. Appl. Meteor.*, **6**, 203-204.

Neggers, R.A.J., 2002: Shallow Cumulus Convection. PhD Thesis, Wageningen Universiteit, Wageningen.

Pickett, M.C., S.A. Young, R. Boers, and C.M.R. Platt, 1995: Lidar observations of boundary layer clouds during the Southern Ocean Cloud Experiment. *Baseline Atmospheric Program Australia 1994-95,* 10-21.

Rodts, S.M.A., 2001: Shallow cumulus dynamics and its parameterization. MSc Thesis, Technische Universiteit Delft, Delft.

Schotanus, P., F.T.M. Nieuwstadt and H.A.R. de Bruin, 1983: Temperature measurement with a sonic anemometer and its application to heat and moisture fluxes. *Boundary-Layer Meteorol.*, **26**, 81-93.

Schrieber, K., R. Stull, and Q. Zang, 1995: Distributions of Surface-Layer Buoyancy Versus Lifting Condensation Level over a Heterogeneous Land Surface. *J. Atmos. Sci.*, **53**, 1086-1107.

Siebesma, A.P., and A.A.M. Holtslag, 1996: Model Impacts of Entrainment and Detrainment Rates in Shallow Cumulus Convection. *J. Atmos. Sci.*, **53**, 2354-2364.

Siebesma, A.P., 1998: Shallow Cumulus Convection. In Plate, E.J., E.E. Fedorovich, X.V. Viegas, and J.C. Wyngaard, editors, Buoyant Convection in Geophysical Flows, Vol. 513, 441-486. Kluwer Academic Publishers.

Siebesma, A.P., P.M.M. Soares, and J. Teixeira, 2004: An advection-diffusion approach for parameterizing turbulent transport in the convective boundary layer. Submitted to *J. Atmos. Sci.*.

Simmer, C., V. Venema, M. Diederich, S. Crewell, A. Feijt, and J. Brenguier, 2004: The Baltex Bridge Campaigns – A Quest For Continental Cloud Structures. *Proceedings of the 14th International Conference on Clouds and Precipitation, Bologna, Italy*, 1742-1745.

Soares, P.M.M., P.M.A. Miranda, A.P. Siebesma, and J. Teixeira, 2004: An Eddy-Diffusivity/Mass-flux parameterization for dry and shallow cumulus convection. Eurocs special issue of *Quart. J. Roy. Meteor. Soc.*

Stull, R.B., 1988: An Introduction to Boundary Layer Meteorology. Kluwer Academic Publishers, Dordrecht, 666 p.

Tiedtke, M., 1987: The parameterization of moist processes. Part 2: The parameterization of cumulus convection. *ECMWF Lecture Series*, 56 p.

Tiedtke, M., 1989: A comprehensive mass-flux scheme for cumulus parameterization in large-scale models. *Mon. Wea. Rev.*, **117**, 1779-1800.

Torrence, C., and G.P. Compo, 1998: A Practical Guide to Wavelet Analysis. *Bull. Amer. Meteorol. Soc.*, Vol. 79, No. 1, January 1998, 61-78.

Troen, I. And L. Mahrt, 1986: A simple model of the atmospheric boundary layer: sensitivity to surface evaporation. *Boundary-Layer Meteorol.*, **37**, 129-148.

Vilà-Guerau de Arellano, J., B. Gioli, F. Miglietta, H.J.J. Jonker, H. Klein Baltink, R.W.A. Hutjes, and A.A.M Holtslag, 2004: The entrainment process of carbon dioxide in the atmospheric boundary layer. Submitted to *J. Geophys. Res.-Atm.*

Wang, B., and Y. Wang, 1996: Temporal structure of the Southern Oscillation as revealed by waveform and wavelet analysis. *J. Climate*, **9**, 1586-1598.

Weijers, E.P., A. van Delden, H.F. Vugts and A.G.C.A. Meesters, 1995: Characteristics of convective turbulence in the surface layer investigated by principle component analysis. *J. App. Meteor.*, **34**, 528-541.

Relevant websites

isccp.giss.nasa.gov	ISCCP cloud data and products
paos.colorado.edu/research/wavelets/	A practical guide to wavelet analysis; examples and software, by C. Torrence and G.P. Compo
www.cesar-observatory.nl	Cabauw Experimental Site of Atmospheric Research
www.knmi.nl/~bosveld/	Homepage of Fred Bosveld, KNMI
www.knmi.nl/samenw/bbc2/	BBC2 Cloud Campaign
www.knmi.nl/voorl/weer/	KNMI Climatological Service
www.met.rdg.ac.uk/radar/cloudnet/	Cloudnet project website